Institut für Kernphysik
Universität zu Köln

Master Thesis

Optimization of the Pulse Shape Analysis for the Position-Sensitive γ-Ray Spectrometer AGATA

Erstgutachter: Prof. Dr. Peter Reiter
Zweitgutachter: Prof. Dr. Jan Jolie

Vorgelegt von Lars Lewandowski
Matrikelnummer 4872509

Köln im Juli 2014

1 Abstract

The position sensitive detection of γ-rays via the Pulse Shape Analysis (PSA) method in highly segmented High Purity Germanium (HPGe) AGATA detectors is investigated. The novel Gamma Ray Tracking technique (GRT) allows to track the path of a γ-ray through the array and to determine the complete deposited γ-ray-energy in the detectors. In this way AGATA delivers spectra compareable to Compton suppressed spectrometers. The tracking also provides a superb Doppler correction by identifying the first interaction point within the array and thereby defining the direction of the incoming γ-ray. The tracking is based on the position information of each individual interaction position. These position information is provided by the PSA which employes the pulse shape of all segments and the central electrode. These pulse shapes are mainly caused by the charge collection process in the crystal. The PSA extracts the position information using the shape of the signal of the hit segment as well as the transient signals of neighboring segments which are induced image charges. For each possible interaction point in the detector a set of signals is calculated forming a database which is used to compare the measured signals with the calculated ones. The position in the detector at which the matching between measured and calculated signals is best is allocated as interaction point by the PSA. Therefore a very good understanding of the detector characteristics is requested. The detector properties are crucial for the analysis and they determine where the PSA allocates the interaction position. However also other detector properties influence the PSA like: crosstalk, electron and hole mobility, crystal axis orientation, space charge distribution due to impurities of the crystal and signal shaping of the preamplifiers and the digitizers. These parameters have to be determined very carefully. Unfortunately not all are available for a direct measurement and they have to be included on an empiric basis. Moreover the impact of the search algorithm and the comparison of measured and calculated signals needs to be scrutinized. The proof of principle of the PSA and the tracking method was already shown successfully, however some systematic deviations from the expected results were observed. This can be seen by deviations of the allocated hit distributions of source runs. Here a homogeneous distribution with statistical fluctuation is expected for interaction points with

the same distance to the source. The final results show systematic deviations from such a distribution. The structure of the segments is visible in these hit distributions though the interaction probability is expected to be the same at every point in the crystal. There exist also points, mostly at the edge of the detector, where the PSA allocates by far too many interaction points. These effects motivated a careful investigation including the detector characteristics as well as the mode of operation of the search algorithm.

Zusammenfassung

In dieser Arbeit wird die positionsempfindliche Detektion von γ-Strahlung mittels der Pulse-Shape-Analysis-Methode (PSA) in hochsegmentierten, hochreinen Germanium AGATA-Detektoren untersucht. Die Gamma-Ray-Tracking-Technik (GRT) erlaubt es den Pfad des γ-Quants durch das Spektrometer zu verfolgen und festzustellen, ob die gesamte γ-Energie deponiert wurde, was am Ende die Qualität von Compton-unterdrückten Spektren liefert. Das GRT stellt auch eine hervorragende Doppler-Korrektur zur Verfügung, indem es den ersten Wechselwirkungsort im Array findet und damit die Richtung des ankommenden γ-Quants festlegt. Das Tracking benötigt die Positionsinformation jeder einzelnen Wechselwirkung. Diese Positionsinformationen werden von der PSA bereitgestellt, welche dafür die gemessene Impulsformen aller Segmente und der zentralen Elektrode verwendet. Die Impulsform wird durch den Prozess der Ladungssammlung bestimmt. Die PSA extrahiert die Positionsinformation, indem sie sowohl die Form des Signals des getroffenen Segments als auch die transienten Signale von benachbarten Segmenten, welche durch Spiegelladungen induziert werden, nutzt. Unabhängig davon werden für jeden möglichen Wechselwirkungsort die Detektorsignale berechnet, wodurch eine Datenbank geschaffen wird, die zum Vergleich zwischen gemessenen und berechneten Signalen eingesetzt wird. Der Punkt im Detektor, an dem die beste Übereinstimmung gefunden wird, wird von der PSA einem Wechselwirkungsort zugewiesen. Für diese Methode ist ein sehr gutes Verständnis der Detektoreigenschaften notwendig. Diese Eigenschaften gehen in die Analyse ein und bestimmen somit die Ergebnisse der PSA mit den Wechselwirkungsorten. Eigenschaften, die die Impulsform beeinflussen, sind unter anderem Crosstalk, Mobilität von Elektronen und Löchern, die Kristallachsenorientierung, Raumladungsverteilungen, die durch Unreinheiten im Kristall verursacht werden und Veränderungen des Signals durch Vorverstärker und Digitalisierer. Deshalb müssen diese Parameter sehr sorgfältig bestimmt werden. Allerdings sind nicht alle Größen einer direkten Messung zugänglich und wurden deshalb empirisch bestimmt. Die Funktionsweise des Algorithmus, der den Vergleich zwischen gemessenen und simulierten Signalen durchführt muss ebenfalls optimiert werden. Die Machbarkeit von PSA und Tracking wurde bereits mit großem Erfolg demonstriert, jedoch gibt es noch systematische Abweichungen von den erwarteten Ergebnissen. Dies kann beobachtet werden, wenn die Trefferverteilungen von Quellenmessungen, die von der PSA zugewiesen wurden, betrachtet werden. Man erwartet für Punkte mit gleichem Abstand zur Quelle eine homogene Verteilung mit zufälligen Fluktuationen. Tatsächlich werden systematische Abweichungen von dieser Erwartung beobachtet. Die Struktur der Segmente

ist in diesen Trefferverteilungen sichtbar, obwohl die Wechselwirkungswahrscheinlichkeit im gesamten Kristall gleich ist und nicht davon beeinflusst sein sollte. Es gibt auch Orte in den HPGe-Kristallen, vor allem am Rand der Detektoren, denen von der PSA deutlich zu viele Wechselwirkungen zugewiesen werden. Die Eigenschaften dieser Effekte wurden im Rahmen dieser Arbeit bestimmt. Dazu wurden sowohl die Detektoreigenschaften als auch die Funktionsweise des Suchalgorithmus eingehend untersucht.

Contents

2 Introduction

2.1 The AGATA Spectrometer

AGATA (Advanced GAmma Tracking Array) was built to investigate nuclear structure and the underlying interactions of the nuclear many body system by measuring the corresponding γ-rays emitted from excited nuclei. It consists of highly electrically segmented high purity germanium (HPGe) detectors which will, in the final configuration, form a full 4π shell. In opposite to existing 4π germanium arrays AGATA does not rely on escape suppression and therefore reaches unmatched efficiency. This is possible due to the high segmentation and the position sensitivity inside the segments which allow to track the γ-ray through the array. This Gamma Ray Tracking (GRT) technique needs energy, timing and position information from of the individual interaction points and is explained in section 2.3 in more detail. The position information, given by the segmentation, is better than in conventional spectrometers. However for γ-ray tracking the interaction point inside the

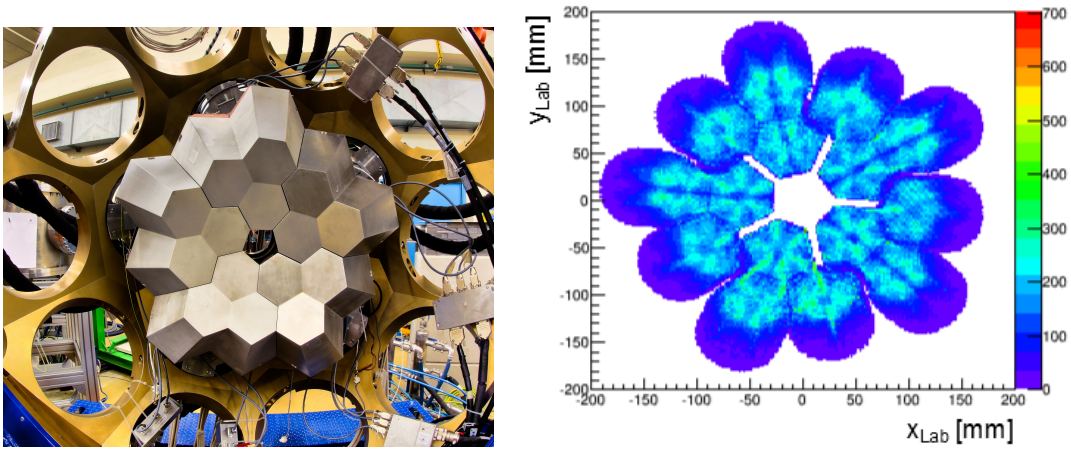

Figure 2.1: The AGATA demonstrator as it was used for experiments at the LNL. It was composed of 5 triple clusters summing up to 15 crystals in total (left). The right plot shows the interaction points of γ-rays within the array assigned by the PSA.

segment is needed. This can be obtained by pulse shape analysis (PSA) methods which will also be explained in more detail in section 2.2. The position sensitivity also allows for a very good Doppler correction. This is especially important as future experiments want to access very neutron or proton rich nuclei via radioactive ion beams which will become available in facilities like FAIR, HIE-ISOLDE or SPIRAL2. The conditions at this radioactive or high intensity ion beams are very challenging considering the requirements for sensitivity, counting rate capabilities or the necessity to cope with Doppler effects due to the high velocities. Conventional spectrometers cannot reach these specifications in performance which motivated new spectrometers like AGATA, or GRETA in the USA. [16, 17]

The full AGATA array will consist of 180 hexagonal detectors forming a full 4π shell with a solid angle coverage of 82%. There are limited possibilities how the individual detectors can be arranged to form a full shell without gaps. A small number of detector shapes is needed due to high development and production cost of the system. Additionally the radius of the full shell has to be large enough to provide enough space for the ancillary detectors at different experimental sites which will host AGATA. The inner radius will be 22.5 cm. The chosen solution with 180 hexagonal detectors was based on Monte Carlo simulations that predict 43% (28%) full energy efficiency and 59% (43%) peak to total ratio at photon multiplicites of 1 and 30 respectively. [17]

2.1.1 Detector Characteristics

The segmentation of the detectors is mainly determined by the detector shape given by the solution for the full shell coverage. Hexagonal detectors are used and a six fold symmetry is the natural solution. Each segment is centered around a corner of the crystal. The segmentation in the longitudinal direction is derived by considering the electric field inside the crystal. It is non trivial due to the central contact that does not go through the whole crystal. A limited number of segments is needed which have a suitable size in order to keep cost and effort for the corresponding electronics reasonably low. At the end 6 segments in the longitudinal direction were considered optimal. The crystals themselves are encapsulated and consist of n-type high purity germanium. The central contact (core) is equipped with a preamplifier that has a reset technique which allows very high counting rates up to 50 kHz. As always the germanium crystals have to be cooled with liquid nitrogen to work properly due to their small band gap of 0.67 eV. Some parts of the preamplifier

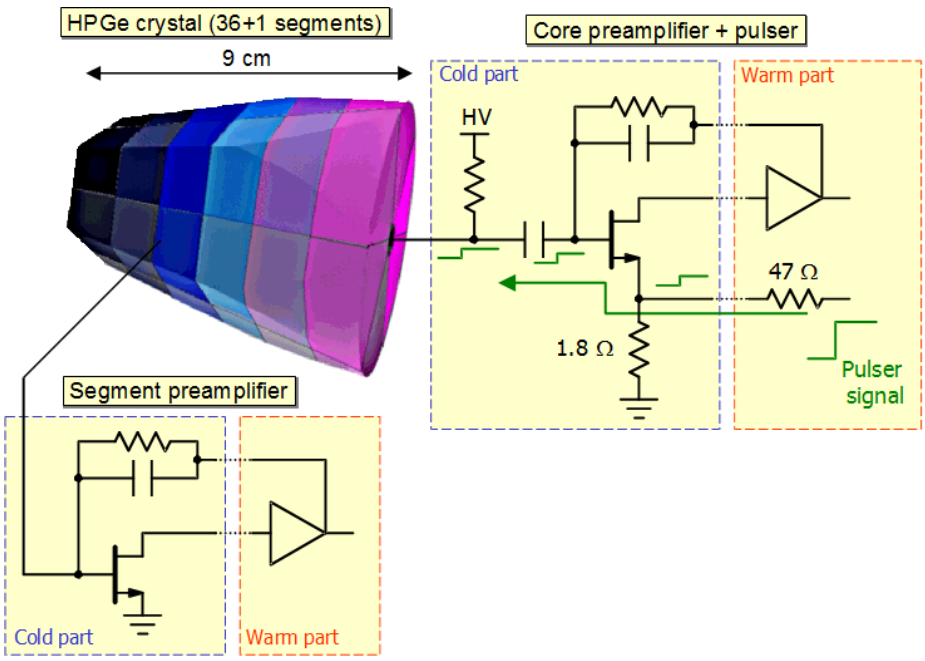

Figure 2.2: A 36 times segmented HPGe detector with the preamplifiers for the segments and the core respectively is shown which have both a cold and a warm part. The core preampifier has to cope with very high counting rates as it has to record all signals of the crystal. [24]

electronics are cooled too, to reduce noise contributions. The electronics are discussed in section 2.1.2.

2.1.2 Electronics

The electronics of the detector have to fulfill the following criterias. The signal of every segment has to be amplified, digitized and written on disk. The system has to be able to cope with very high counting rates of up to 50 kHz per crystal. The preamplifiers need good energy and timing properties and a transfer function that influences the signal as little as possible because the signal itself is needed for the pulse shape analysis. The preamplifiers have a cold and a warm part which consist of a low noise silicon FET in the cold part and a low noise transimpedance preamplifier in the warm part, see fig. 2.2.

A fast reset mechanism is implemented to reduce dead time of saturated preamplifiers and increase the accessible energy range up to 180 MeV via a time over threshold (TOT) method [17]. The fast reset mechanism detects if a preamplifier is saturated and connects a drain current. The time over threshold relates to the deposited energy and behaves

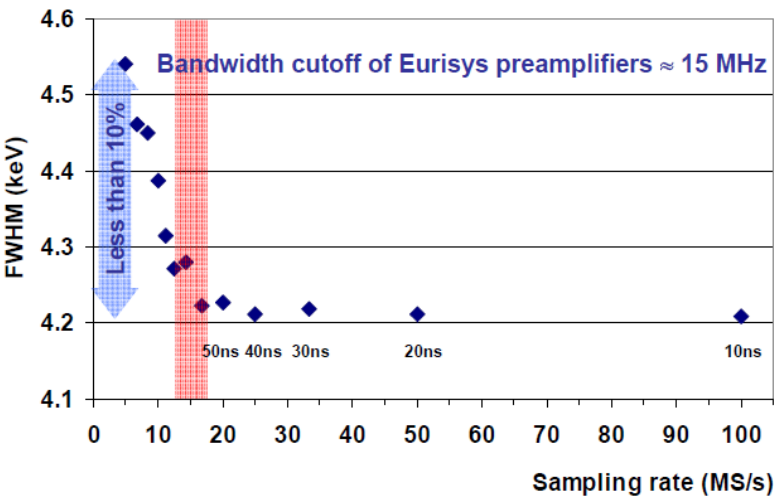

Figure 2.3: The dependence of the Doppler corrected FWHM on the sampling rate of the digitizers is shown. Higher sampling rates allow better comparisons of calculated and measured signals and therefore bettter PSA result which lead to better tracking and improved Doppler corrections. But the effect is relatively small and is not more than 10%. The used digitizers have sampling rates of 100 MHz and are therefore more than sufficient. [26]

nearly linear with small quadratic corrections. The preamplifier signal is transferred to the digitizers which receive all 37 signals from one crystal, determine the energy with a trapezoidal filter and digitize them at a rate of 100 MHz at 14 bit. This means that the pulse is measured in time steps of 10 ns. The core signal is used to create a logic signal with a constant fraction discriminator (CFD) [17]. The maximum frequency that can be processed is 50 MHz as described by the Nyquist theorem. The Nyquist sampling rate is always the half of the actual sampling rate. This means the sampling rate must be twice as high as the frequency of a measured signal if data loss is to be avoided completely. Else aliasing comes into effect. In practice this frequency is only about 20 Mhz. The impact of the sampling rate of the digitizers on tracking performance is shown in Fig. 2.3. [2]

Both preamplifiers and digitizers alter the signal due to their intrinsic properties. A preamplifier integrates the charge with a RC circuit and therefore alters an input signal that is a step function into an exponential saturation described by $\tau = \mathrm{RC}$. This behavior is described by the so called transfer or response function. The read out signal $F(t)$ is the convolution of the real signal $f(t)$ and the transfer function $T(t)$

$$F(t) = \int_{-\infty}^{\infty} f(t-\theta)T(\theta)d\theta \tag{2.1}$$

As the data consists of single data points and is not continuous the discrete form is used. For the deconvolution of the signal the discrete Fourier transform (or the Laplace transform) is used. If $\mathcal{F}$ denotes the Fourier transform of a function then the Fourier transform of the convolution is the product of the Fourier transform of the two functions:

$$\mathcal{F}(f(t) * T(t)) = \mathcal{F}f(t) \cdot \mathcal{F}T(t) \tag{2.2}$$

The transfer function T has either to be measured or estimated by an analytic function. The real signal can be obtained using the back transformation. For discrete signals instead the z-transform is used which is the discrete form of the Laplace transform. It is given by:

$$\mathcal{Z}f(t) = \sum_{n=-\infty}^{\infty} f(t)z^{-n} \tag{2.3}$$

With z being a complex number and f a discrete function of t. It can be easily shown that the transform of the convolution is the product of the tranforms of the individual functions. Typically an exponential decay is assumed for the transfer function with a decay constant τ that has to be determined. [10]

The transfer function was evaluated in this work, assuming an exponential behavior and finding the correct value for τ.

Transient Signals

The induced currents in neighboring segments can be understood by considering a simplified example of a charge above a grounded metal plate. This charge induces a surface charge depending on the distance to the surface z_0. The created field is:

$$E(x, y) = \frac{qz_0}{2\pi\epsilon_0(x^2 + y^2 + z_0^2)^{\frac{3}{2}}} \tag{2.4}$$

If the plate is divided in individual steps (see Fig. 2.4) and the charge above the plate moves along a path $r(t)$ a current is induced $I_i(t) = \frac{\mathrm{d}Q_i}{\mathrm{d}t}$ where i is the respective segment on the surface. The induced charge $Q_i(\vec{r}(t))$ can be described by a weighting potential Φ_i:

$$Q_i(\vec{r}(t)) = -q\Phi_i(\vec{r}(t)) \tag{2.5}$$

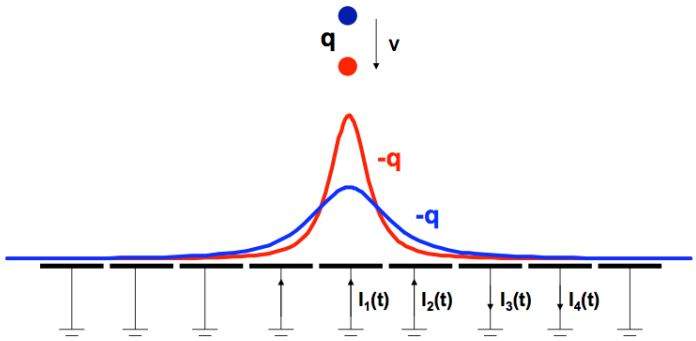

Figure 2.4: Simple model to describe the induced currents on a surface generated by a charge q that moves along a path $r(t)$. The surface can be dividied into individual segments which allows to introduce a weighting potential that describes the induced charge on this segment for a given time t. [11]

This allows to write for the induced current:

$$I_i(t) = -q\frac{\mathrm{d}\Phi_i}{\mathrm{d}t} = \left(\frac{\mathrm{d}\Phi_i}{\mathrm{d}x}\frac{\mathrm{d}x}{\mathrm{d}t} + \frac{\mathrm{d}\Phi_i}{\mathrm{d}y}\frac{\mathrm{d}y}{\mathrm{d}t} + \frac{\mathrm{d}\Phi_i}{\mathrm{d}z}\frac{\mathrm{d}z}{\mathrm{d}t}\right) = q\vec{E}_{\Phi,i} \cdot \vec{v}_{drift} \tag{2.6}$$

$\vec{E}_{\Phi,i}$ is weighting field that is generated by the weighting potential. [11]

Crosstalk

The segmentation of the crystals causes crosstalk due to the capacitive coupling between the crystal and its preamplifier front end electronics which is in the order of 0,1%. To retain the very good energy resolution a crosstalk correction has to be performed. It can be assessed by comparing the energy of the core with the energy sum of the segments. In an ideal scenario the same value is measured however deviations that come from crosstalk properties of the segmented crystal are observed. This behavior is strongly dependent on the segment multiplicity, which is the number of segments that registered an energy above the threshold. The main part of the crosstalk, that influences the measured energy spectra, is an effect dominant at low frequencies. It reduces primarily the energy resolution and does not change the pulse shape. There is also a high frequency crosstalk effect, referred to

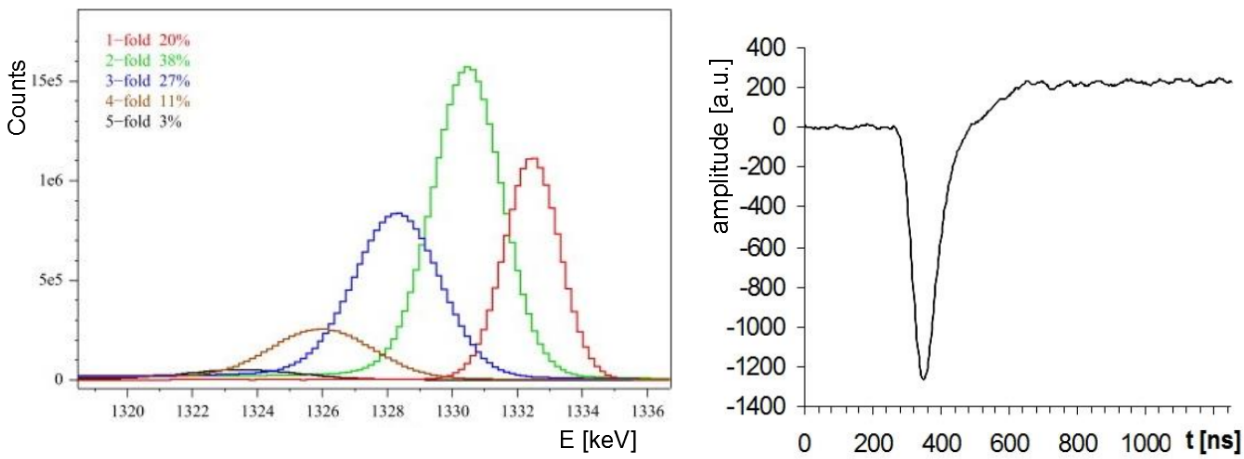

Figure 2.5: The energy spectra of the ^{60}Co peak for different segment multiplicities is shown without crosstalk correction. The energy resolution worsens for higher folds and a shift of the centroid is observed. The right plot shows a typical signal influenced by crosstalk. The shifting of the trace as well as a high frequency effect called differential crosstalk can be seen. The differential crosstalk does not affect the measured energy but is important for the PSA. The impact of crosstalk effects is non negligible and makes a correction imperative. [15]

as differential crosstalk, which influences the pulse shape and affects the PSA. Therefore, also the γ-ray tracking is affected. In a first approach the crosstalk can be measured by comparing the energy shifts in the γ-ray spectrum of events with a segment multiplicity of m = 1 with 2-fold events with m = 2. The dependence of the energy shift and the energy resolution on segment multiplicity due to crosstalk is shown in fig. 2.5.

A linear electronic model that describes the observed effects was derived by [15]. It regards the Alternating Current (AC) coupling, also called capacitive coupling, of the core preamplifier to the crystal, as well as the Direct Current (DC) coupling from the segment preamplifier to the crystal. A schematic with a 2-segment detector (for simplicity reasons) is shown in Fig. 2.6. There is a large resistance R_{fb} in parallel to the feedback capacitance C_{fb} described by an impedance Z_{fb}. The schematic drawing can be converted into in AC equivalent scheme. In this scheme the depleted detector can be described as a network of capacitances $C_{i,j}$. There is the coupling of the segments to the core by the corresponding capacitances which are $C_{0,1}$, $C_{0,2}$ in the schematic and the coupling of the segments is given by $C_{1,2}$. The coupling of the core to the segments is the more dominant one and can be measured directly. In contrast to that the coupling between the segments is not available for direct measurement. It can be assumed that $C_{i,j} \ll C_{0,j}$ for $i \neq 0$. The

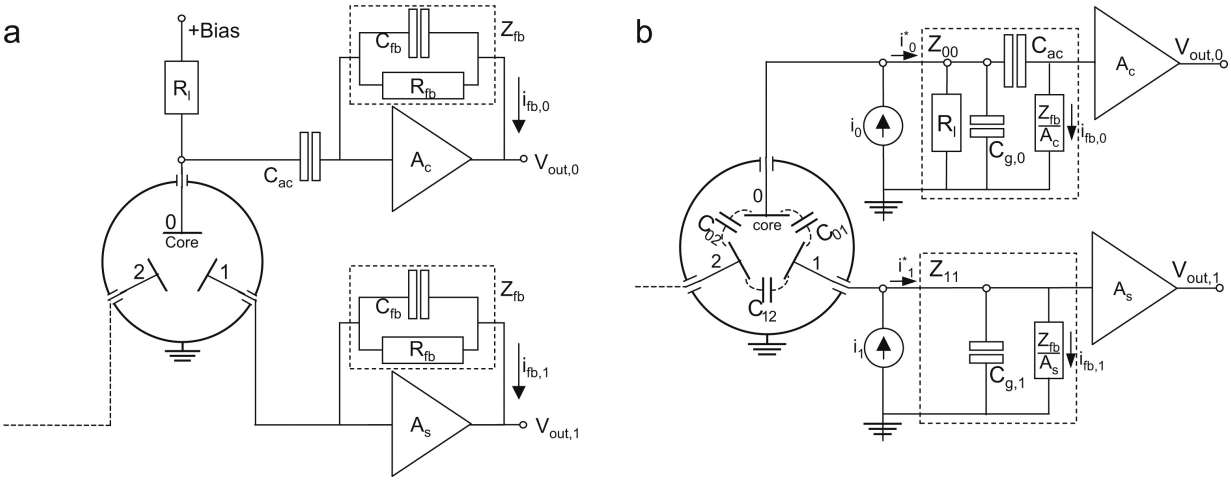

Figure 2.6: Schematic drawing of a 2-fold detector that shows the AC coupling of the core preamplifier and the DC coupling of the segments. The scheme on the right side is AC equivalent and shows that the system can be described by an electronic network of capacitances that couple the core to the segments as well as the segments themselves. [15]

segment to segment coupling is of importance for directly neighboring segments as the corresponding capacitance depends on the areas of the involved segments, their distance and their orientation to each other. There is also a coupling between the segment and the ground, as encapsulated detectors are used. There is a current induced between the electrode and the ground by the moving charged particles in the detector. This is described by the Shockley-Ramo theorem. [19]

The overall current that is generated in the charge collection process can be described by the feedback currents and a 37 x 37 matrix that is the inverse of the transfer function. (Details of this model are described in [15]):

$$\vec{i} = T^{-1}\,\vec{i}_{fb} \tag{2.7}$$

The matrix includes information about the impedances $Z_{i,j}$ caused by the corresponding capacitance and its parallel resistance as well as the impedance between the node and the ground. The crosstalk can then be estimated in the model by evaluating the off diagonal matrix elements of the transfer function matrix. Not the whole current, which is generated at the electrode, is seen by the preamplifier. A part is picked up by the other segments, whereby the amount can be estimated to be $\frac{Z_g}{Z_g+Z_{i,j}}$. Z_g is the impedance between the node and the ground and as $Z_g \ll Z_{i,j}$ it can be written $\frac{Z_g}{Z_g+Z_{i,j}} \approx \frac{Z_g}{Z_{i,j}}$. Inserting typical

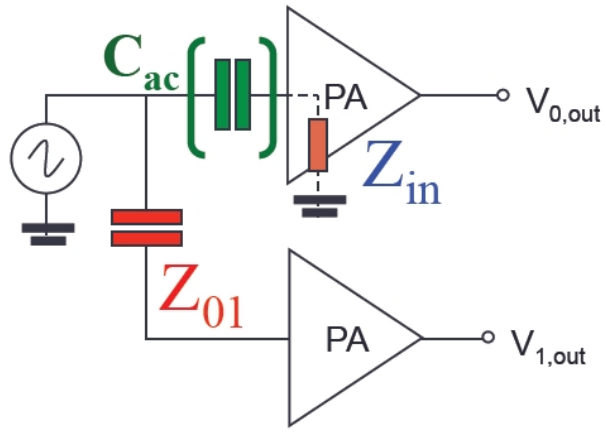

Figure 2.7: A simple scheme of the preamplifier of one segment and the core with the corresponding impedances is displayed. The core is AC coupled due to the capacitance C_{AC}. The input impedance is frequency dependent with an Ohmic offset. [10]

values for the impedances reduced segment energies of around 0,1% are obtained whereas the core energy is not affected in very good approximation. [14]

As mentioned earlier there is also a high frequency crosstalk effect illustrated in Fig. 2.5 called differential crosstalk. The differential crosstalk affects the signal during its risetime and it does not affect the measured energy but is important for the PSA. The simulated signals can only match the measured ones if all effects that alter the measured signal are considered and corrected for. A simple scheme with a core and a segment preamplifier is shown in Fig. 2.7. As stated above the crosstalk is given by $\frac{Z_g}{Z_{i,j}}$ in good estimation. Considering the proportional part the impedance between node and ground is given by the Miller effect and therefore $Z_g \propto \frac{1}{sAC_{fb}}$ with s being a complex frequency from the Laplace transform. The Laplace transform $F(s)$ of the function $f(t)$ is given by:

$$F(s) = \int_0^\infty f(t)\mathrm{e}^{-st}dt \tag{2.8}$$

The transformation allows to transform differential equations into simple algebraic equations as it is done here for $I(t) = C\frac{\mathrm{d}U}{\mathrm{d}t}$ which transforms to $i(s) = Csu(s)$. The rewritten form for the impedance is then:

$$z(s) = \frac{u(s)}{i(s)} = \frac{1}{sC} \tag{2.9}$$

To include the differential crosstalk the frequency dependence of the impedance has to be

considered. The dependency of Z_g is given by the frequency dependence of the feedback capacitance and has an offset which is an Ohmic resistance R. Including the AC coupling $Z_g = \frac{1}{sAC_{fb}} + \frac{1}{sC_{ac}} + R$ is obtained. The overall crosstalk is given by [10]:

$$\text{Crosstalk} \approx \frac{Z_{in}}{Z_{0,1}} \propto \underbrace{\frac{C_{0,1}}{AC_{fb}} + \frac{C_{0,1}}{C_{ac}}}_{\text{proportional}} + \underbrace{RC_{0,1}}_{\text{differential}} \tag{2.10}$$

The first two terms describe the proportional crosstalk and the last term contains the contribution from the differential crosstalk. As they both depend on the core to segment capacity $C_{0,1}$ proportional and differential crosstalk are related. To find the segment to core capacity $C_{0,1}$ the baseline shift (or the energy shift of the peak) of the segments has to be measured depending on which segment was hit. A constant shift independent of which segment was hit can always be observed. This is caused by the segment to core capacity which always contributes to the signal. Only if neighboring segments are hit a deviation from that can be seen which consists of the segment to segment contribution (additional to the always present segment to core contribution). The core to segment capacity can then be estimated by averaging over all shifts, neglecting the segment to segment coupling. The Ohmic resistance cannot be measured directly and has to be chosen empirically so that the crosstalk corrections best describes the detector response. [8, 9] The input parameters of the differential crosstalk correction were optimized in this work.

2.2 Pulse Shape Analysis

To determine the interaction position of a γ-ray within the Ge-crystal the pulse shape of the charge collection is analyzed. Several algorithms were developed within the AGATA community to perform this analysis for different scenarios. All of these algorithms have to be very fast as the analysis will be performed online during future experiments. The amount of data will be too high to write everything (without triggering) on disk and to analyze it later. It is possible to replay the data and alter the analysis that is performed. The data that is used for the replay is considerably compressed.

Several algorithms were developed such as genetic algorithms, adaptive grid and particle swarm search as well as wavelet decomposition and matrix methods [17]. The adaptive grid search algorithm that divides the crystal into grid points and compares measured and

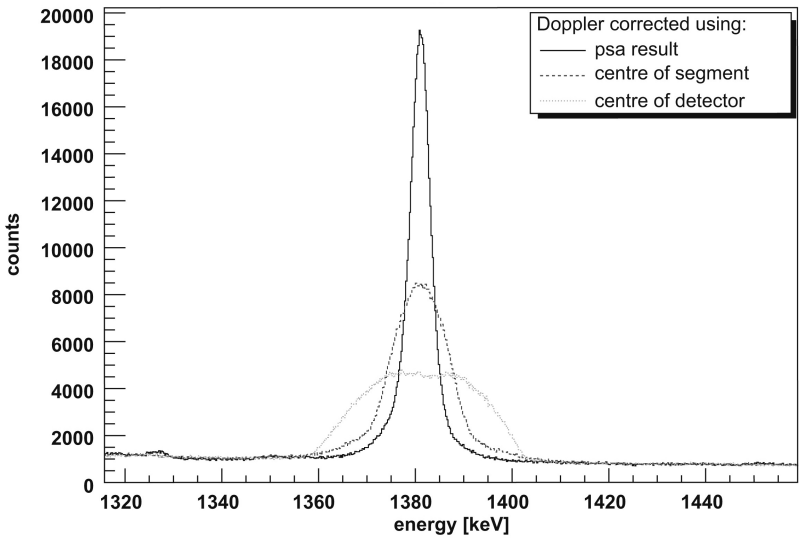

Figure 2.8: Energy spectra with and without Doppler correction. The Doppler correction assumes either the detector center (like in conventional spectrometers), the segment center or the PSA result as interaction position which shows the power of the PSA to perform excellent Doppler corrections. The 1382 keV peak of ^{49}Ti has a FWHM of 4,8 keV, 14 keV and 35 keV for the PSA, segment center and detector center models. [22]

simulating traces for every grid point going from a coarse to a fine grid is the most commonly used one. It is also used in this work including transient and net charge signals. It is explained in detail in section 2.2.2. Some of the algorithms such as the particle swarm search are much faster and were developed in order to cope with a high number of interactions within the crystal. Multiple interactions within one segment are a challenge too, as those events have to be recognized and dealt with. The standard version of the adaptive grid search does not include multiple interactions within one segment though there are some early versions that try to deal with this problem. Monte Carlo simulations and first measurements show that the resolution with this grid search algorithm is approximately 5 mm and therefore within the specifications to perform γ-ray tracking. [23]

2.2.1 The AGATA Data Library

The grid search algorithm needs to know the detector response for an interaction of each grid point. Measuring this response, namely the net and the transient signals is extremely time consuming and up to now only simulated traces can be used. The AGATA Data Library ADL contains this information. To create this library the Poisson equation is

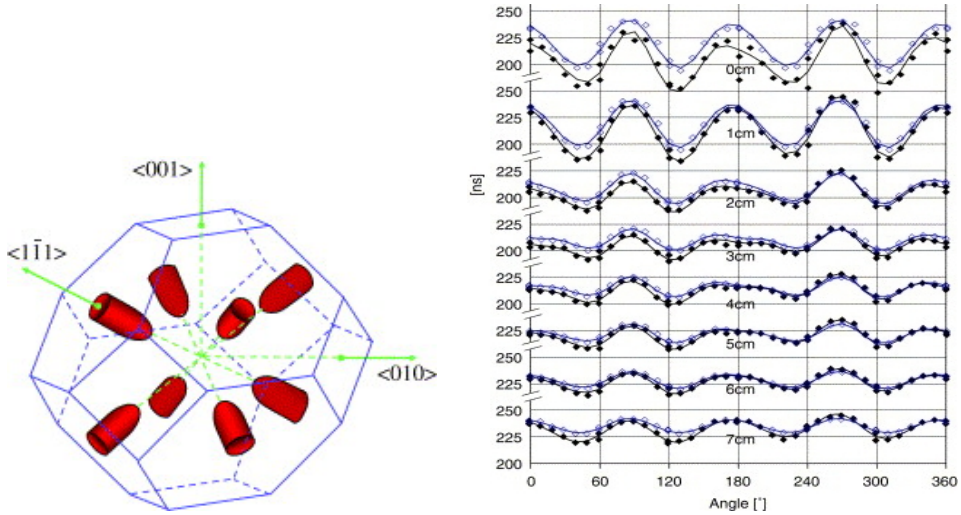

Figure 2.9: The first Brillion zone for germanium is shown in the left picture. The minima in the band structure in the conduction band are displayed in red. Their shape is ellipsoidal and their surface is defined by a constant energy. The right plot shows measured (black) and simulated (white) risetimes of electrons in dependence of radius and angle of the interaction. The risetime decreases for higher radii. The lattice orientation and its impact on the risetime can be observed by the angular dependence. [12, 13]

solved for every interaction point. The cloud of charges that is created of an interaction point can be assumed point like in good approximation. The shape of the electrical field and the corresponding potentials have to be known very well. In the front part of the detector the central contact is not present. The fields are inhomogeneous even in case the contact is bulletized, meaning that the edges are smoothed.

A good knowledge of the different mobility of electrons and holes is needed. This mobility depends on the orientation of the crystal axis due to the band structure of germanium. Germanium has a cubic lattice and crystallizes in the diamond structure. If the crystal is cooled to liquid nitrogen temperature the charges do not move exactly in the direction of the field lines of the external electrical field that is applied. The internal electrical field created by the lattice cannot be neglected. A theoretic description of charge carrier mobilities is given in [12]. In combination with crosstalk properties, response functions and space charge distributions the detector is fully described and the traces can be calculated. The impurity of the crystal has an impact on the potential and the capacitance between the inner and outer electrode. It causes a space charge distribution which affects the created signals during charge collection as shown in Fig. 2.10. The impurity of the HPGe material

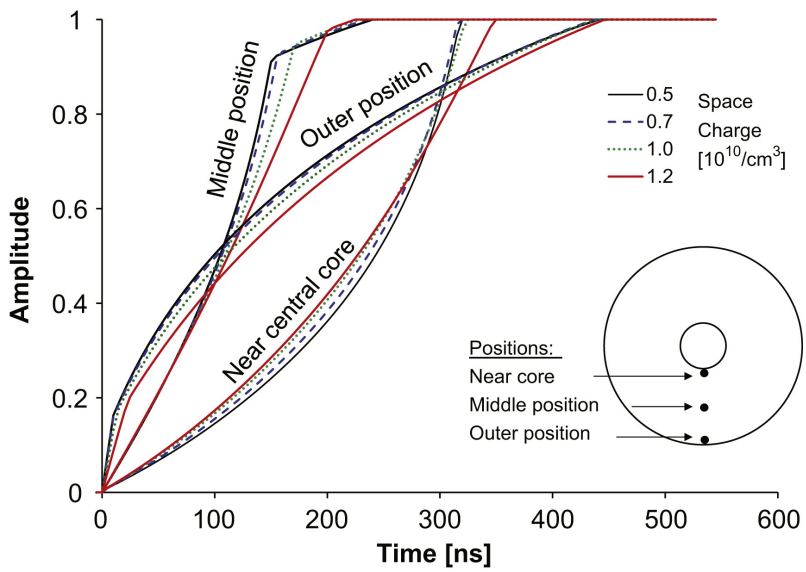

Figure 2.10: The simulated impact of the space charge distribution on the signals is shown for different typical interaction positions and different space charge densities. The figure demonstrates that the knowledge of the impurity concentration of the crystal and the corresponding space charge is a necessary ingredient for the PSA. [7]

is only known to a certain extent and is hard to access experimentally because the crystal is encapsulated by the manufacturer. An average value for the top and the bottom of the crystal are provided by the company from a Van der Pauw measurement. [7]

The space charge can be estimated by capacitance voltage (CV) measurements. For this the capacitance of the detector in dependence of the bias voltage is measured [3]. The remaining net space charge N(d) in dependence on the depletion depth d is given by:

$$N(d) = |N_D - N_A| = \frac{-C^3}{\epsilon e A^2}\left(\frac{dC}{dV}\right)^{-1} \quad [3] \tag{2.11}$$

N_D and N_A are the donor and acceptor concentrations, A is the crystal surface and C the capacitance of the detector. The model given in eq. 2.11 assumes a planar setup but the high segmentation of the crystal can be used to measure the core to segment capacities for every segment to get a three dimensional reconstruction of the space charge distribution. The space charge distribution completes the set of needed parameters and allows to solve the equations, that describe charge transportation within a semiconductor. They are taken from [7].

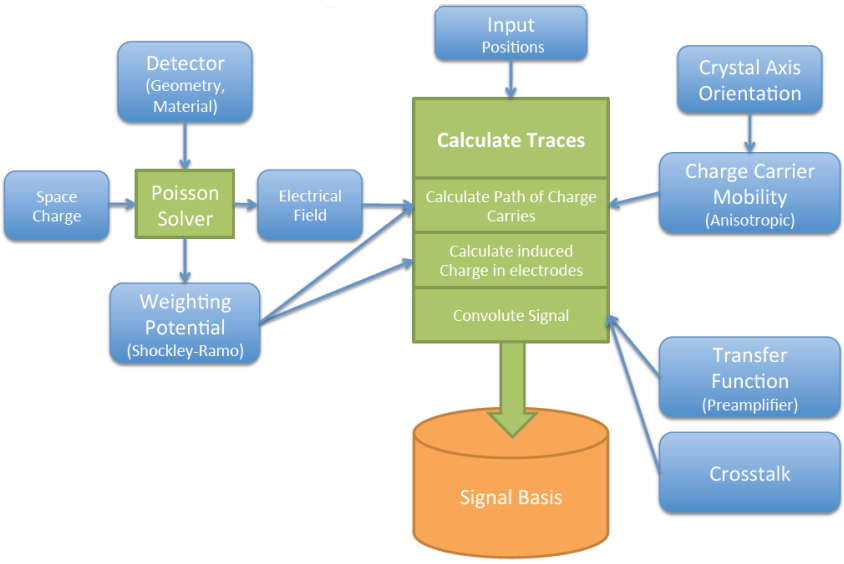

Figure 2.11: The ingredients of the ADL are illustrated in blue, the algorithms that solve the corresponding equations in green and the final basis in orange. Only a good knowledge of the input paramters can ensure a well working PSA. The whole ADL can be generated by solving the corresponding equations that describe the detector. These are the Poisson equation, the continuity equation and the description of the current densities (Ohm's law). [4]

$$\Delta\Phi = -\frac{e}{\epsilon}[N - n + p] \tag{2.12}$$

$$\vec{j_n} = -e\mu_n n \text{ grad}\,\Phi + eD_n \text{ grad}\, n \tag{2.13}$$

$$\vec{j_p} = -e\mu_p p \text{ grad}\,\Phi - eD_p \text{ grad}\, p \tag{2.14}$$

$$\frac{dn}{dt} = \frac{1}{e}\text{div}\,\vec{j_n} - R \tag{2.15}$$

$$\frac{dp}{dt} = -\frac{1}{e}\text{div}\,\vec{j_p} - R \tag{2.16}$$

All functions depend on space and time. In the Poisson equation in eq. 2.12, Φ is the potential, N the space charge, n the electron and p the hole density. The currents of the electrons n and holes p $\vec{j_n}$ and $\vec{j_p}$ are described by the respective electron and hole mobility μ_n and μ_p and their diffusion coefficients D_n and D_p. The equation of continuity (charge conservation) for the two densities is described by a recombination rate R. The change of the densities in time is set to zero as a steady state condition of the detector is assumed for simplicity. As the AGATA detector is n-type p is set to zero and the the leakage current $\vec{j_n}$ is neglected as well as the diffusion coefficients.

These assumptions allow to solve the equations numerically. The results are given for a 2 mm grid and for time steps of 5 ns as ingredients of the AGATA Data Library which is used by different PSA algorithms. The currently used digitizers have a sampling rate of 100 MHz and the calculated time steps are sufficient to compare the measured and the calculated signals with timesteps of 10 ns. The ADL depends on the following input parameters: crosstalk, response function, impurity concentration and space charge distribution, electron and hole mobility, electrical fields and the crystal orientation. These parameters have to be determined very carefully and may differ for each individual crystal. A set of detector signals created by the ADL is shown in Fig. 2.12.

2.2.2 The Adaptive Grid Search Algorithm

The adaptive grid search algorithm uses the ADL to compare the measured and calculated signals. Therefore, for each interaction the hit segment signal and the neighboring transient signals are compared with the calculation. This comparison has to be done for every grid point in the hit segment. A different set of traces belongs to every grid point. The comparison is done by minimizing a figure of merit that is defined as:

$$\text{Figure of Merit} = \sum_{i,j} |A^m_{i,j} - A^s_{i,j}|^p \tag{2.17}$$

Where the sum goes over the relevant timescale $i = T_0,\ T_0 + 1, ...,\ T_f$ It is done for all the involved segments j that are the hit and their neighboring segments. A^m and A^s are the corresponding value of the measured and simulated signal. The exponent p is a positive and real number. The selection of this parameter is discussed in detail in section 3.3.1. The PSA is the most time consuming part of the analysis. To reduce computing time the comparison is done for two different grids. First a coarse 6 mm grid is used and then the PSA is performed around the found interaction point in a finer 2 mm grid. If the energy of the interaction is below a certain threshold only the coarse search is performed to save computing time. For low energy interactions the position resolution is worse than the scale of the 2 mm grid. The combination of the coarse/fine grid allows to find the interaction point with good precision using a minimum number of iterations.

Both the measured amplitude $A^m_{i,j}$ and the simulated one $A^s_{i,j}$ depend strongly on time. Therefor, the determination of the starting time T_0 has to be performed precisely which is done via a digital CFD algorithm. Due to different cable length etc. the starting time of

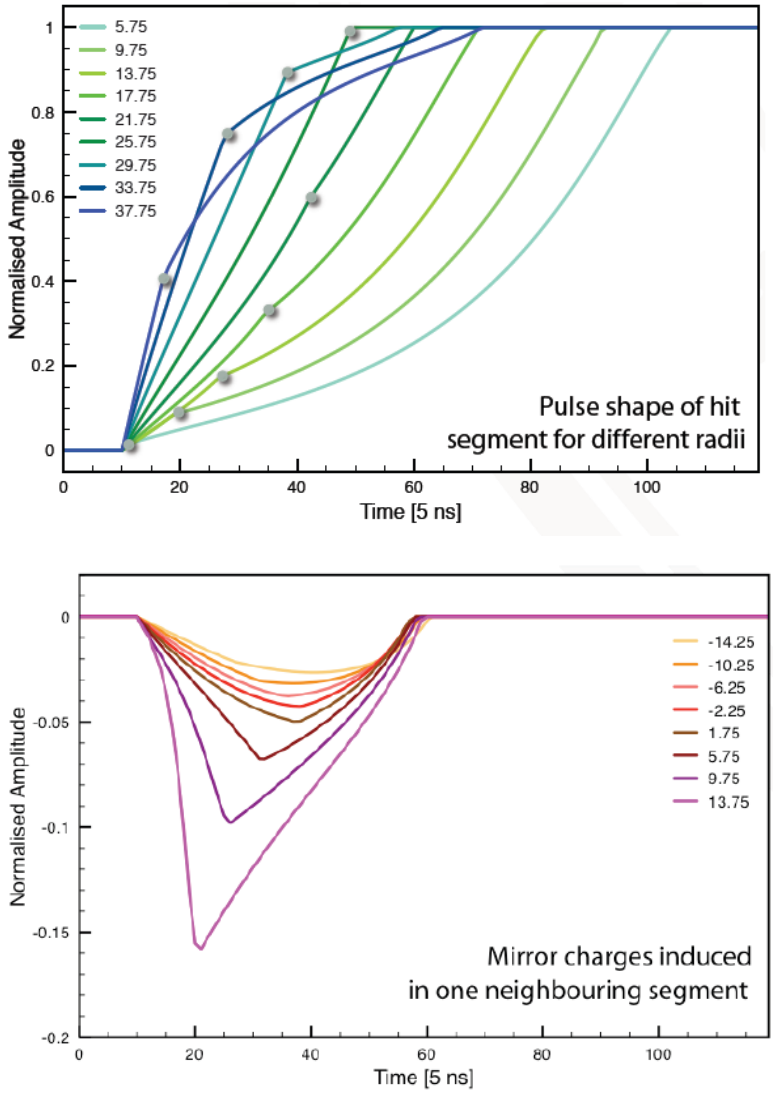

Figure 2.12: Simulated signals generated by the AGATA Data Library. The net signal (left) and the transient signal of one neighboring segment (right) is shown for different radii of the interaction position. Depending on the radius of the interaction the traveling time for electrons and holes changes. The grey dots in the left plot indicate at which time the collection of the electrons is finished. Especially for larger radii a strong change in the slope of the signal due to the smaller mobility of the holes can be observed.[11]

the neighboring segments may differ from that and all traces have to be time aligned very carefully. This is done by performing the minimization of the figure of merit not only by varying the interaction point but also by implementing a time adjustment in the following way:

$$\text{Figure of Merit} = \sum_{i,j} |A^m_{i+\Delta i,j} - A^s_{i,j}|^p \tag{2.18}$$

An improved time alignment should cause a better agreement between calculated and measured traces. After performing the PSA for the first time the adaptive grid search algorithm performs the time adjustment. In case the time adjustment delivers a figure of merit value below the previous one the new interaction point is taken as result of the PSA. This procedure is repeated until no significant change in Δi (1,5 ns is used) is achieved or the predefined maximum number of loops is reached. The maximum number of loops is set to 10 in the standard setup because the whole analysis may not take too long, especially when performed online. In the offline analysis, the replay of the data, this value may be increased if it delivers improved results. There is also a minimum number of loops, that is four in the standard setup, as well as a maximum time shift of 5 ns to avoid unreasonable shifting. To reduce the needed computing time only a small part of the signal before the trigger and a certain part of the risetime is used for the time adjustment. The standard setup uses 40 ns of the pre trigger signal and 250 ns of the risetime. It is important to use the signal before the trigger if the time shift is negative. All these parameters were chosen to find an optimum between computing time and performance of the time alignment. The time alignment improves by increasing the maximum number of loops or by using a lower value for the minimal time shift. The algorithm should converge so that additional iterations yield only very small changes in Δi.

Multiple interactions in one segment have to be considered. These events are far more complex to handle and the unknown parameters increase the number of degrees of freedom for the algorithm. First of all there are obviously two interaction points; However the sharing of the deposited energy in each interaction point is not known. Only the sum of the energy is measured leaving the energy fraction E_1/E_2 as parameter. But these energies are crucial for the PSA and this parameter has to be varied. That leads to a rise in the needed time per event.

It is impossible to decide whether an event has multiple interactions in one segment beforehand. It is done after the PSA for a single interaction was already performed and the matching between the measured and the best fitting signal is bad. A threshold for the

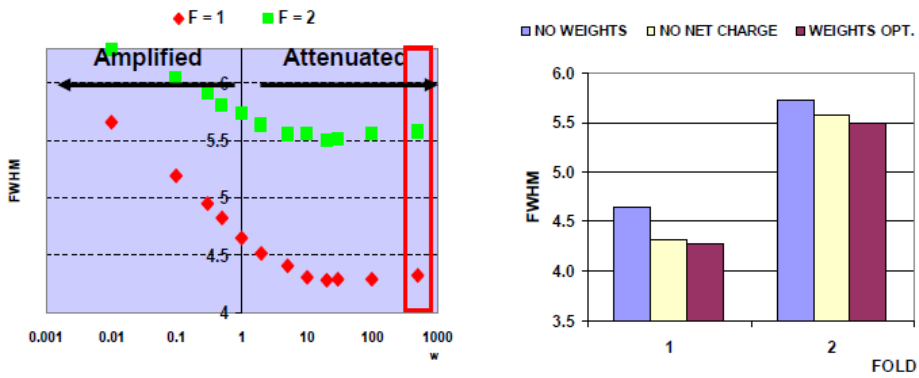

Figure 2.13: The effect of the implementation of a weighting factor on the net signal is shown. This factor describes how strongly the net signal impacts the PSA result compared to the transient signals. It is absolutely possible to even neglect the net signal completely as shown on the right. The optimal behavior is reached for an attenuating weighting factor that disfavors the net signal. [26]

figure of merit value has to be defined and the two hit search has to be performed if it is above that threshold. There are additional problems that arise when trying to cope with multiple interactions in one segment with the adaptive grid search. If the energy fraction is very small or very close to one, only the interaction point of the interaction with the high energy deposition can be extracted with good accuracy. If it is close to 0.5 it is likely that both interactions will be interchanged which poses a problem for the tracking because the energies do not fit to the interaction point and the event might be rejected. The probability for multiple interactions in a segment is, depending on average crystal multiplicity, reasonably low which is also discussed later in section 3.4. This all leads to the fact that most commonly those multiple interactions in one segment are neglected when using the adaptive grid search. If only single interactions are taken into account the events with multiple interactions will have the center of the two interaction points, weighted by their respective energies, as result of the PSA. The found point $\vec{r}_{PSA}$ will be:

$$\vec{r}_{PSA} = \frac{\vec{r}_1 E_1 + \vec{r}_2 E_2}{E_1 + E_2} \tag{2.19}$$

The impact of the transient signal on the PSA result has also to be considered. Ideally both information are used. But as the difference of measured and simulated amplitudes goes into the algorithm and since the amplitude of the net signal is much higher than the transient one it has to be ensured that this information is not neglected by the algorithm. A variation of a weighting factor that is attached to the net signal implies that the net

signal can either be completely ignored or should be less strongly weighted. How net and transient signals influence the PSA result is also described by the exponent p in eq. 2.17. A larger exponent will favor the net signal since the difference of the amplitudes for a given time will always be proportional to the entire deviation from the baseline. This will also be discussed later in section 3.3.1.

2.2.3 Measured Bases and Scanning Tables

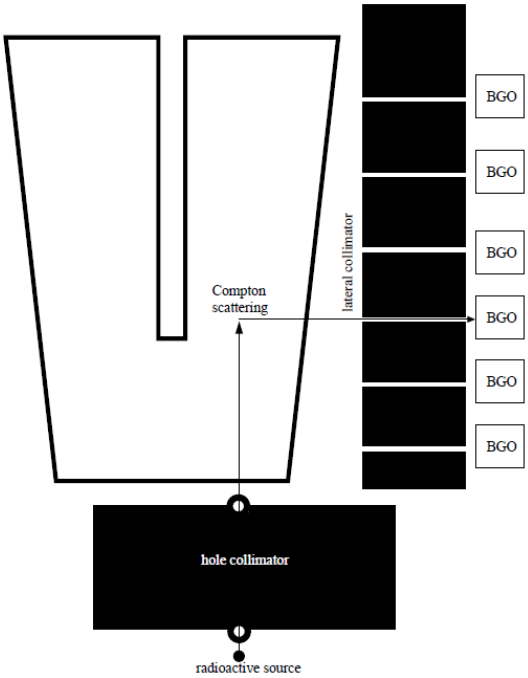

Figure 2.14: The Liverpool scanning table setup is shown. There is an incident photon, beam defined by a collimator, interacting within the crystal. The interaction point is restricted by gating on Compton scattering of 90 degrees and demanding a coincidence with a BGO detector that is placed around the crystal. To assure that the outgoing photon after the Compton scattering is actually in a plane perpendicular to the incident beam a lateral collimator is placed before the BGO detector. [25]

In contrast to the simulation approach it is possible to create a database of signals for each interaction point in the detector by measuring these signals directly. This has the advantage that all the aspects of the detector properties that go into the final signal shape, like crosstalk etc., are automatically included. On the other hand it is quite challenging to actually measure these signals with a precision that is above that of the simulation. It has to be ensured that the interaction actually took place at the position for which

the signal base is to be evaluated. A collimated beam of γ-rays is used that reduces the number of degrees of freedom of the interaction position to one. The finite width of the beam that extends for larger distances from the source has to be considered. To extract the actual position information a BGO detector is placed at an angle of 90 degrees with respect to the investigated grid point. A gate on an energy deposition that corresponds to a Compton scattering of 90 degrees and a coincidence with the BGO detector is required. This way the interaction position is restricted to a single point. The resolution of this point depends on the quality of the collimation and the solid angle that the BGO detector covers. The solid angle can be reduced by using a lead shielding allowing a small slit. In this way the error of the angle of the Compton scattering is minimized. The setup is shown in Fig. 2.14 though the BGO is covering 360 degrees which is not shown for simplicity reasons. The setup implies very long measurement times since the rate of accepted events is very low due to the two collimations and the restriction to a small energy range. The signal shape is averaged over all events. This possibly causes a loss of information as small deviations of the signal vanish. These measurements have to be done for every grid point individually as well as for every individual detector. The lengthy measurements make it unlikely that the measured bases will replace the simulation in the near future. Though it is a very important method for cross checking the simulated ADL results and to improve the understanding of the detector by adjusting the ADL parameters to match the measured signals.

There are other possible setups that reduce the time needed to create the full database, for example by increasing the possible interaction points that can be measured simultaneously or by removing the first collimator. The position information given by the first collimator could also be acquired by using a position sensitive detector that is placed behind a β^+ source like ^{22}Na. Since the two 511 keV photons are emitted in an angle of 180 degrees the direction of the beam is known. Though these methods are promising the time to measure a full base is still very long.

2.3 γ-ray Tracking

To ensure good Doppler correction and Compton suppression the path of the γ-rays through the array has to be reconstructed. With the interaction positions and energies provided by the PSA the γ-ray tracking algorithm is able to to disentangle the individual hits. The

complexity of the problem scales with the number of individual γ-rays that hit the array and their energies. Depending on the energies of the incident γ-rays the potential interaction mechanism change as well as the probabilities for the individual interaction. These probabilities are given by the corresponding cross sections for the photoelectric effect, Compton scattering and pair creation. Compton scattering is the most dominant process in the typical energy ranges investigated. To reconstruct the track of one or multiple γ-rays the algorithm varies the number of incident γ-rays, to which γ-ray the individual interactions belong and the order in which the interactions happened. In this space of possible combinations all permutations have to be evaluated. Depending on the deposited energy in an individual interaction the scattering angle between different positions due to the Compton effect is well determined. This rules out most or ideally all but one combination. If no combination can reproduce the tracks of the γ-rays through the array then it is assumed that not the entire energy was deposited in the detector and the event is rejected. There are several approaches to perform this, mainly the back- and forward-tracking algorithms. However it has been shown [21] that the forward tracking and clustering technique is nearly always superior. Back tracking algorithms start from the last interaction point which should be a photo effect (for a non escaping γ-ray). This approach has the advantage that it is mainly independent from the incident energy of the γ-ray because the probability for the photo effect becomes dominant for relatively low energies of 100 to 250 keV.

The forward tracking divides the interactions into clusters defined by two angles (ϕ, θ). If they are within a close angular range they are packed together. The idea relies on the fact that forward scattering is dominant for Compton scattering. This is illustrated by the Klein-Nishina differential cross section for Compton scattering shown in Fig. 2.15. For every cluster of hits a figure of merit is defined describing how well the assumed scattering angle matches the one calculated from the deposited energy.

$$\mathrm{FOM} = \exp\left(-2\frac{(E_{\mathrm{Rest}} - E_{\mathrm{Compton}})^2}{\sigma_e^2}\right) \quad [21] \tag{2.20}$$

Where E_{Rest} is the energy left after the considered interaction, E_{Compton} the energy after scattering that is calculated using the angle θ and the Compton formula and σ_e the assumed uncertainty of E_{Compton} due to the uncertainty of the interaction positions and the scattering angle θ. E_{Compton} is calculated by:

$$E_{\mathrm{Compton}} = \frac{E}{1 + \frac{E}{m_e c^2}(1 - \cos\theta)} \tag{2.21}$$

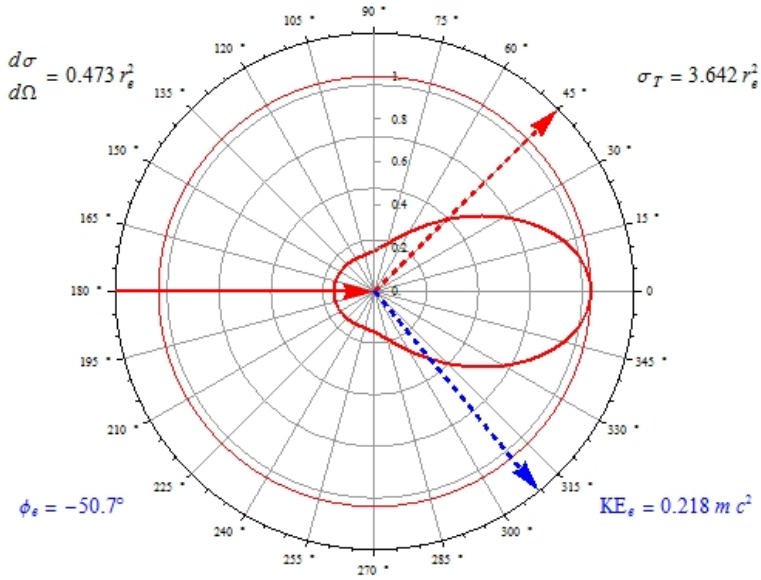

Figure 2.15: The tracking algorithm is based on the energy dependent Compton scattering. The plot shows the differential Klein-Nishina cross section for Compton scattering for an incident γ-ray energy of 500 keV. It can be clearly seen that forward scattering is dominant which allows to sort the interaction positions into clusters of hits within an angular cone. [5]

If the interactions are aligned in the right order and belong to the same γ-ray both E_{Rest} and E_{Compton} should be nearly the same. For every combination of interactions within one cluster the sum of all figure of merits is calculated. The combination with the maximum FOM is assumed to be the true track. The FOM is above a certain threshold, else the event is rejected because most likely not the entire γ-ray energy was deposited. Dividing the interactions in clusters allows to minimize the number of permutations that have to be evaluated.

2.4 AGATA Data Processing

The whole AGATA data structure is designed to collect the data from the different parts of the setup, merge them and perform an online analysis. Therefore, after a trigger was generated the raw data of all 36 segments and the core is collected and digitized. The triggering and the selection of the data that is given to the PSA is called preprocessing. The PSA is performed with the passed data using the energy, pulse shape and timing

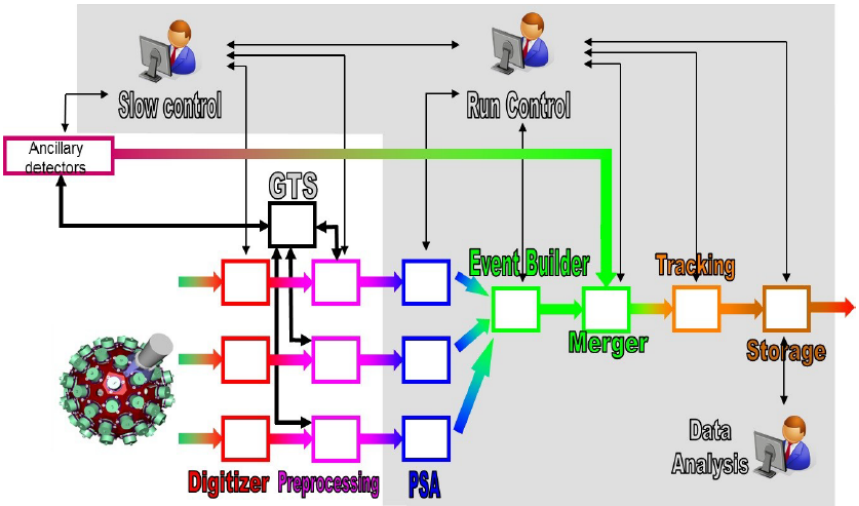

Figure 2.16: The data flow is depicted in a simple scheme. The digitized raw data from the individual crystals is given to the preprocessing. If the raw data contains a signal above a set threshold a logic signal is given to the Global Triggering System GTS. Depending on the desired information a global trigger is send out (for example if also ancillary data is present) and data from all triggering detectors is collected. After the PSA the event building for the whole array is performed and the events are then merged with the corresponding ancillary data. The complete set of merged data is then used for tracking and Doppler correction.

information. Then this individual PSA data is merged with the data from the other crystals by performing an event building including all detectors of AGATA. The events are then merged with any ancillary data, if present. After that the tracking is performed. The whole online analysis, including the PSA, the event building, event merging and the tracking is performed using the NARVAL [18] environment. This environment allows other programs, like the Watchers, to extract online information at any point in the data flow. NARVAL creates data in the AGATA Data Format ADF which contains every information necessary to perform PSA, event building, merging and tracking. This allows to perform an offline analysis and to optimize the input like calibration, crosstalk coefficients etc. or to change the parameters of the ancillary detectors. [17]

2.4.1 Replay of Data

The offline analysis is also called the replay of the data. It is done with a NARVAL emulator that treats the incoming ADF data like incoming data from a running experiment. The most commonly used NARVAL emulator is called femul [1] which is a C/C++ software

package. It allows to mimic the preprocessing, the PSA, the event building, the merging and the tracking as well as any desired topology of involved AGATA or ancillary detectors.

In the preprocessing the energy calibrations are performed, a first time alignment, given by individual offsets for every channel, decay times of the preamplifiers and rise times of the trapezoidal filter can be chosen. It is possible to select different options for triggering, to set energy gates or to require a certain segment fold. The preproccessed data contains the energies, timestamps and pulse shapes which is given to the PSA filter. The crosstalk coefficients are read in here and the signal base is corrected accordingly. Also the chosen distance metric is read in (see section 2.2.2), as well as the decay constants for the response function, the information for trapping corrections or the type of search algorithm. These parameters all affect the PSA result. After the event building of all AGATA data and the merging with ancillary data the tracking is performed. This allows to trigger on the ancillary detectors and only perform the tracking if ancillary data is present. The tracking has relatively low computing requirements compared to the PSA which uses up most of the CPU time. In this part of the analysis the forwarded data from the PSA containing energy timing and position information, as well as the corresponding ancillary data and the tracked data is written into a root [6] tree. The transformation of the position information of the individual crystal into the lab system is also performed for proper Doppler correction.

3 Analysis

The hit distributions allocated by the PSA show some unexpected behavior. An unphysical clustering of hits can be observed. There are also interaction points at the edge of detector which have too much hits allocated by the PSA taking statistical fluctuations into account. Exemplary hit distributions of a source run that show these effects are depicted in Fig. 3.1 and 3.2. The observed behavior of clustering or the wrongly allocated hits at the edge of the detectors can be observed in all 15 crystals. The presented depictions show that the distribution of hits is very similar for all detectors. The wrongly allocated hits at the edge of the detector appear at the same detector depth z for all detectors. This leads to the conclusion that the underlying problem of the PSA affects all detectors in the same way.

These effects motivated the development of observables (or criteria) which are able to assess this behavior quantitatively and are introduced in section 3.1. These criteria use

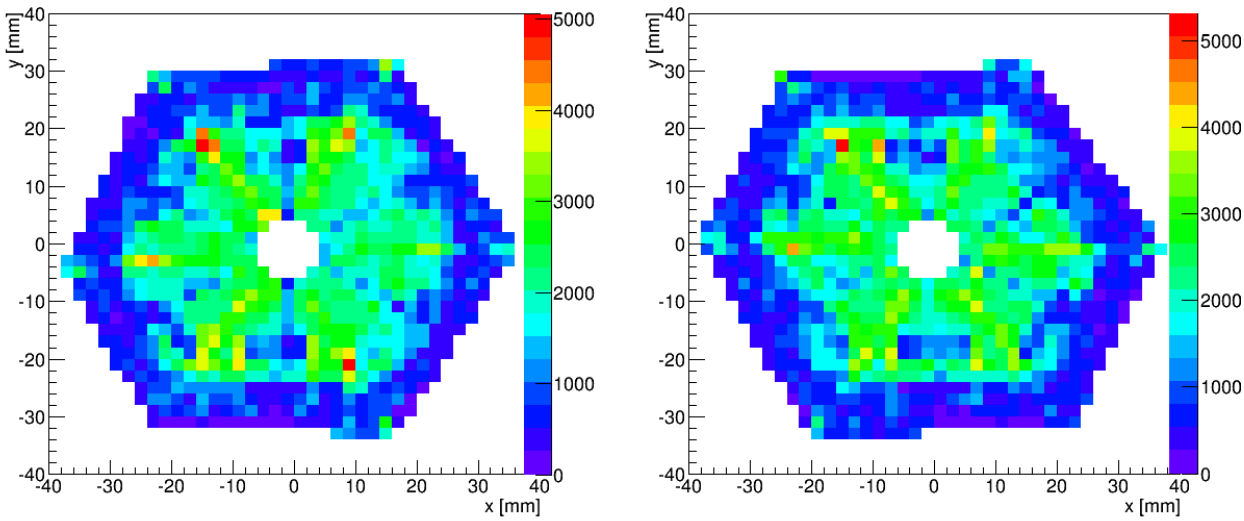

Figure 3.1: The distribution of hits in the xy-plane for two different detectors and a detector depth z = 20 mm is shown. A clustering of hits in the middle of the segments can be observed. No distinct deviations between the two detectors can be seen.

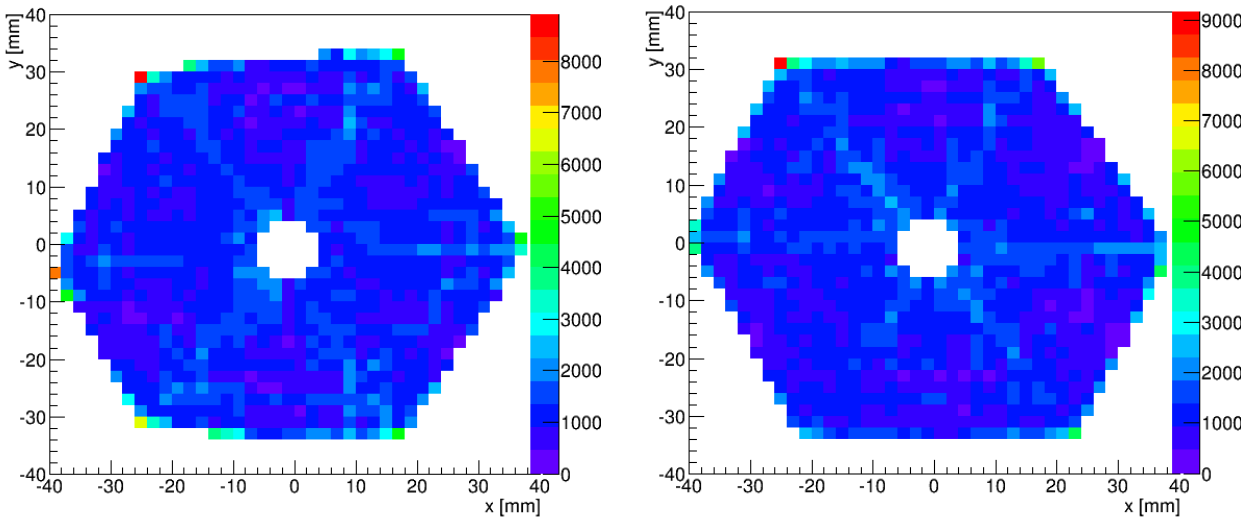

Figure 3.2: The distribution of hits for two different detectors and a detector depth of z = 30 mm is shown. At this detector depth the wrong allocation of hits to one interaction point at the edge of the detector is the dominating effect. This effect occurs at the same depth z for both detectors.

the fact that for a source run a homogeneous distribution of hits for interaction points with the same distance to the source is expected. Experimental data from measurements at the Legnaro National Laboratories LNL with the AGATA demonstrator, consisting of five triple clusters, was used. This data includes long time source runs and in beam γ-ray spectroscopy. The latter was an experiment in which a 1 GeV ^{136}Xe beam impinged on an ^{238}U target. Beam like particles were identified with the mass spectrometer PRISMA [28] and the tracking performance was investigated [4]. The quality of the Doppler correction, which is determined by the tracking performance, was examined in this work. A Doppler corrected spectrum is shown in fig. 3.4. For the long time source measurement an ^{152}Eu source was used. The measurement consists of $2.7 \cdot 10^8$ individual interactions within the array. The corresponding energy spectrum of hits and the tracked spectrum are shown in Fig. 3.3. These energy spectra show the power of the tracking. The tracked spectrum has a superior peak to total ratio. The source was placed in the center of AGATA.

To create the plots shown in Fig. 3.1 and 3.2 a C/C++ code was written. The experimental data was replayed with the Narval emulator femul. The code loops over all events of the investigated source run and extracts all information like energy, x-,y-,z-coordinates or the hit segment. This way distribution of hits were created that can be gated on any of these

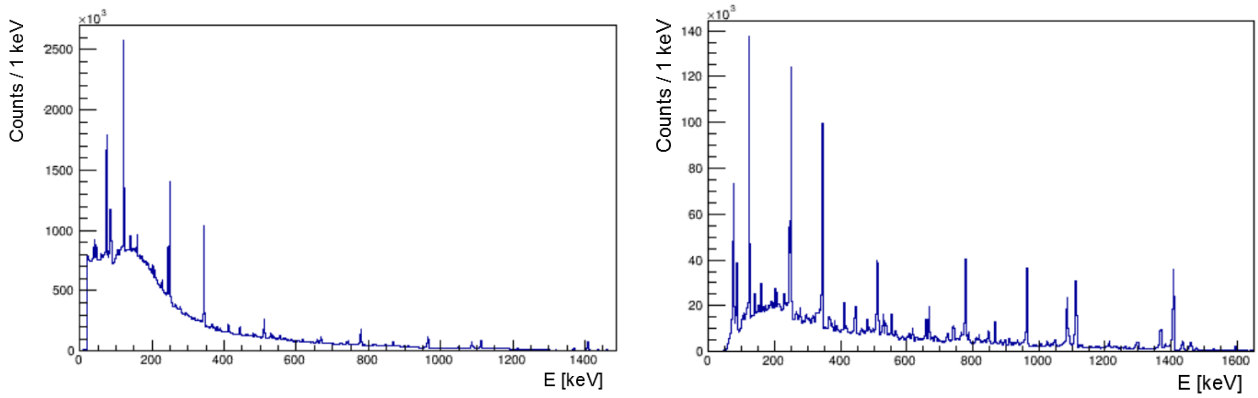

Figure 3.3: The energy spectrum of the individual hits and the tracked γ-ray spectrum of the used ^{152}Eu source run is shown. The tracked spectrum has a superior peak to total ratio. A reduction of the number of entries in the peaks in the tracked spectrum can also be observed.

information. With such gates the energy and position dependence of the PSA performance was examined.

The source measurement allows to observe the distribution of hits and compare it with the expectation. The developed observables can be used to improve the PSA by varying its input parameters. If changing an input parameter of the PSA causes a reduced clustering this new parameter value is used instead. The ingredients for the PSA were discussed in section 2.2. First the developed observables will be introduced and then the obtained results regarding energy and position dependence will be discussed. The created observables and criteria were used to improve and optimize the PSA performance which will be discussed in section 3.3.

3.1 Methods and Observables

To judge PSA performance quantitatively observables are needed to make statements about how well the PSA is working. With these observables the change in position resolution when choosing different values for certain parameters in the PSA can be described. The methods and observables that were developed and used in this work to make these statements are presented in the following sections.

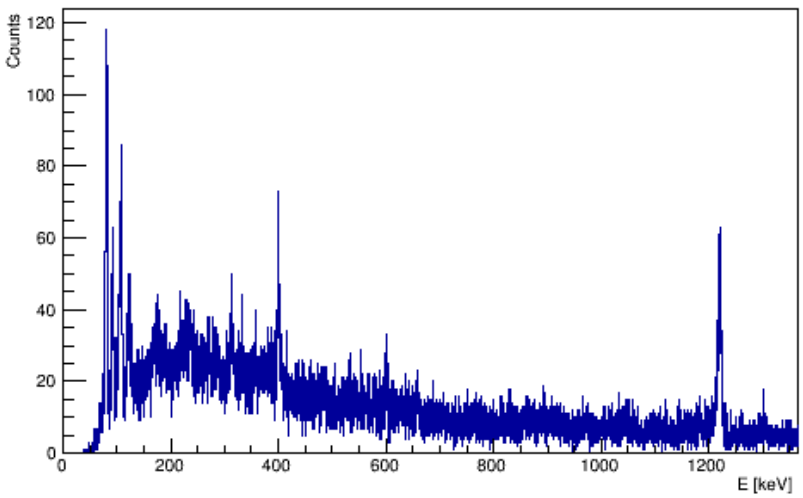

Figure 3.4: The tracked and Doppler corrected spectrum for atomic charge Z = 54 (Xenon) and mass A = 137 is shown. The data is taken from the LNL 11.22 experiment in which an ^{136}Xe beam impinged on an ^{238}U target. The Doppler correction was performed by [4]. Even after the Doppler correction the resolution cannot reach the performance of a source run. The peak at 400 keV has a FWHM of 3,26 keV.

3.1.1 Quality of Doppler Correction

The first criteria that is usually considered when judging the position resolution of the PSA is the quality of the Doppler correction. The correction needs as input the angle between velocity vector $\vec{v}$ of the excited nucleus and the direction of the emitted γ-ray described by the wave vector $\vec{k}$. The wave vector $\vec{k}$ has to be determined by the first interaction point of the γ-ray within the detector array. The velocity vector of the nucleus has to be determined from the kinematics of the reaction. In this way the quality of the Doppler correction is a direct measure of the tracking performance. It is also a measure for position resolution because the tracking relies on the PSA. The relativistic Doppler correction is given by:

$$E_\gamma = E_{\gamma,0} \frac{\sqrt{1-\beta^2}}{1-\beta\cos\theta} \tag{3.1}$$

Where $E_{\gamma,0}$ is the energy of the emitted γ-ray, E_γ the measured energy and θ the angle between velocity vector of the emitting nucleus and direction of emission of the γ-ray.

It has already been shown [4] that the overall quality of the Doppler correction provided by AGATA is well within the specifications and delivers clean γ-ray spectra with sharp peaks.

A tracked and Doppler corrected spectrum is depicted in Fig. 3.4. A good estimate for the quality of the Doppler correction is the Full Width Half Maximum (FWHM) of the full energy peaks. The quality of the Doppler correction, depending on the PSA performance, was investigated. Results are shown and discussed in section 3.3.1.

3.1.2 Homogeneity of the Hit Distribution

Another way to describe the PSA performance is the homogeneity of the distribution of hits in the detector. Therefore, a calibration run was used where the source was placed in the center of AGATA. Then in good approximation the expected number of interactions within the crystal for a constant detector depth z is the same within the corresponding xy-plane of the detector, like the ones shown in Fig. 3.1 or 3.2. In such a plane a homogeneous distribution of hits is expected since the interaction probability is the same. It can be assumed that all interaction points in such a xy-plane have the same distance to the source. This assumption is a good approximation because the distance to the source is much larger than the typical radius of the detector and the considered xy-planes can be estimated to be on the surface of a sphere. It can be observed that the distribution is in fact not completely homogeneous which means that for some events the interaction positions determined by the PSA are not the true physical interaction points. This means a more homogeneous distribution of hits corresponds to a better PSA performance. The inhomogeneity of the distribution can be seen in two ways (i) the structure of the segments is visible and (ii) certain grid points mostly located at the outer edge of the detector show more hits allocated by the PSA than would be expected within statistical fluctuations. This qualitative statement has to be converted into a quantitative measure and further tools are needed. These tools or criteria describe how well the PSA reflects the expected homogeneous distribution of interactions.

Deviation from the mean

As a first criterion the deviation from the mean is introduced. Therefore, the bin content BC of grid points for one detector depth z is considered. For same distances to the source the bin content is expected to be the same on average. All these grid points of one detector with the same distance to the source are compared and analyzed. As stated above xy-planes of the detector are used for this. First of all the mean bin content μ is derived by summing

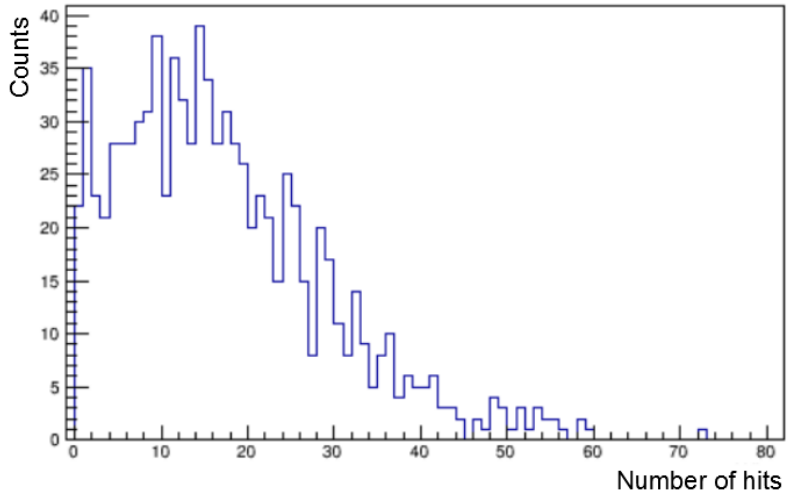

Figure 3.5: The distribution of the number of hits within the individual grid points of one exemplary xy plane is shown. The mean μ and the deviation from the mean ΔBC can be extracted from this distribution. The error of 11.98 is significantly above the Poisson error $\sqrt{\mu}$=4.12.

over all grid points in the considered xy-plane. The grid points are described by their x and y coordinates, so $BC_{x,y}$ is the bin content of the respective coordinates.

$$\mu = \frac{1}{N} \sum_{x,y \in D} BC_{x,y} \tag{3.2}$$

N is the number of grid points in the considered plane and D is the set of grid points belonging to the detector for the considered detector depth z.

The shape of the detector leads to different forms of D for each z. That means a method has to be developed to find the set of grid points belonging to the detector D for each z and to keep track of N. It has to be checked for every single grid point if it belongs to the detector. This is done using the fact that hits can only be allocated by the PSA to interaction points within the detector. If the number of hits within a grid point is above zero it is assumed to be an element of D. This method was further improved to include grid points that have no hits allocated by the PSA but belong to the detector. Therefore, an algorithm was implemented that checks the neighboring grid points of the considered point for their respective bin contents. If a set number of those are empty the grid point is considered to be outside of the detector and is discarded. At the edge of the detector 3 to 4 or in exceptional cases 5 of the neighboring grid points will be empty by default which has to be regarded. This method has the advantage that grid points within the

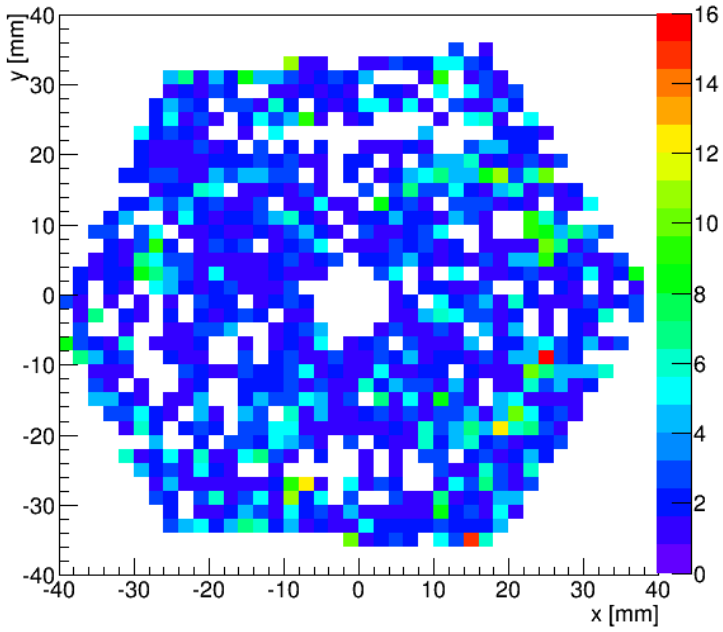

Figure 3.6: The hit distribution for a detector depth of 40 mm of one detector is shown here with a cut on the energy to 510±10 keV. The used method will not work in a low statistic scenario like shown here. Grid points within the detector will be rejected by the algorithm since the bin content of their neighbours is zero as well.

detector that are empty are not rejected. Empty grid points within the detector have to count towards the mean and the deviation from the mean which will be introduced in the next paragraph. This method will not work if a great part of the grid points are empty due to low statistics as an example shows in Fig. 3.6. To avoid this low statistic cases a long time source run with the highest possible number of hits was analyzed.

With the derived mean μ the deviation from the mean ΔBC can be assessed by:

$$\Delta BC = \sqrt{\frac{1}{N-1} \sum_{x,y \in D} (BC_{x,y} - \mu)^2} \tag{3.3}$$

It has to be noted that this representation of the standard deviation assumes that the single measurements of $BC_{x,y}$ are independent which is not true. There is a correlation between grid points that are close together and show clusters of counts. So the defined value is just an approximation for the standard deviation which is defined as:

$$\sigma = \sqrt{\mathrm{Var}(BC_{x,y})} = \sqrt{E(BC_{x,y}^2) - (E(BC_{x,y}))^2} \tag{3.4}$$

With $E(BC_{x,y}) = \mu$ being the expectancy value for the bin content in the corresponding (x,y) tuple. The distribution of the number of hits in each individual grid point is shown in Fig. 3.5. The mean μ and the deviation from the mean ΔBC can be extracted from such a distribution. It can be seen that it does not behave like a Poisson distribution. The derived error is about a factor of three higher than the Poisson error.

The such calculated value ΔBC carries information on the homogeneity of the distribution for one detector depth z in one detector. But for optimization purposes an assessment parameter for the whole array is needed. To achieve this the value ΔBC is calculated for every z and every detector. Those values are not comparable since they depend on the mean μ in the corresponding xy-planes. Therefore, a normalization is needed. To find the correct normalization parameter for every xy plane the formula for ΔBC has to be considered. Taking $BC_{x,y} \propto \mu$ into account it can be written:

$$\sqrt{\sum_{x,y \in D} (BC_{x,y} - \mu)^2} \propto \mu \tag{3.5}$$

That means every value for the deviation from the mean of each xy-plane has to be normalized by the corresponding mean μ:

$$\Delta BC_{\text{norm}} = \frac{\Delta BC}{\mu} \tag{3.6}$$

The normalized values can then be compared and be used to judge the performance of the whole array. It is convenient to combine the normalized values into one final parameter as a measure for PSA performance. ΔBC carries only information for a certain z from one detector.

$$\Delta BC = \Delta BC(z, i) \tag{3.7}$$

Where i labels the detector number. The final parameter P judging the PSA performance is then:

$$P = \frac{1}{n} \sum_{z,Det.i} \frac{\Delta BC(z, i)}{\mu(z, i)} \tag{3.8}$$

Where n is the number of considered xy planes. In the used data there were 15 detectors and the granularity of the grid is 2 mm which gives $15 \cdot 45 = 675$ xy planes. This number may increase if additional conditions e.g. on the energy of an interaction are applied. The derived value P describes the deviation from the mean μ and is therefore a measure for the homogeneity of the distribution. When performing a variation and optimization of PSA

input parameters this value has to be minimized.

Correlation coefficient

The deviation from the mean is independent of the position of the grid points within the considered xy plane. It is a good way to describe the inhomogeneity of the distribution of hits but it cannot describe the tendency of the PSA to allocate hits in clusters located in the middle of the segments. To include this position dependent effect into the analysis a new quantity was developed. A correlation coefficient was defined to describe the clustering of hits in the detector. This value describes the correlation between neighboring grid points. Two grid points are correlated if their bin content behaves similar. If the first grid point has an above average number of hits as well as the second grid point they are correlated. The same is true for two grid points with below average number of entries. To reduce the effect of random fluctuations the correlation has to be calculated for many neighboring grid points. The covariance cov describing the correlation is defined as:

$$\mathrm{cov} = E[(BC_{x,y} - E(BC_{x,y}))(BC_{x,y+2} - E(BC_{x,y+2}))] \tag{3.9}$$

Here E is the expectancy value for the corresponding random variable with $E(BC_{x,y}) = E(BC_{x,y+2}) = \mu$ since the expected bin content is the same for all points of one xy-plane. The neighboring grid point of (x,y) has the coordinates (x,y+2) because the grid has a granularity of 2 mm. For simplification only the correlation in y direction is discussed here.

For the calculation of the covariance cov the expectancy value of the product in the brackets is derived by going over all tuples (x,y) in the considered xy-plane. Since the covariance for different xy-planes needs to be comparable like in the case of ΔBC a normalization is necessary. Each term $BC_{x,y} - E(BC_{x,y})$ is proportional to the deviation from the mean which was already calculated:

$$BC_{x,y} - E(BC_{x,y}) \propto \Delta BC \tag{3.10}$$

So the normalized covariance which is called the correlation coefficient η is given by:

$$\eta = \frac{\mathrm{cov}}{\Delta BC^2} \tag{3.11}$$

The correlation coefficient η describes the normalized covariance for one xy-plane. A final

parameter for the correlation over the whole array P_{corr} is then given by:

$$P_{\text{corr}} = \frac{1}{n} \sum_{z,i} \eta(z,i) \tag{3.12}$$

The correlation coefficient depends on the value of the deviation from the mean ΔBC. To get two independent observables the normalization can be performed with μ^2 instead, since $\Delta BC \propto \mu$.

3.2 Quantitative description of systematic PSA errors

The final parameters in eq. 3.8 and in eq. 3.12 are used to describe the PSA performance of the complete array in the following analysis and will be referred to as deviation from the mean and correlation coefficient for simplification purposes. In an ideal case for the correlation coefficient a value of zero is expected. However it is observed that it is always significantly above zero which means that there is indeed a correlation of neighboring grid points. The normalized deviation from the mean is typically in the order of one which means that it is in the order of the mean μ.

3.2.1 Visibility of the Segments

The PSA behavior has to be described qualitatively and quantitatively. Inspecting the distribution of hits it can be seen that not all hits are allocated to their correct interaction points by the PSA. This is visible best by investigating source measurements with the source in the center of AGATA. Examining a set of grid points with the same distance to the source the structure of the segments can be seen as shown in Fig. 3.7. Such behavior is not expected because the interaction probability in this plane is the same.

This implies that the PSA algorithm shifts hits from the segment border to the middle of the segment. The dependence on the energy and the detector depth z will also be discussed later in section 3.2.2. The segment borders in z direction can be estimated to be at 8,21,36,54,72 and 90 mm in first order. The effect of clustering and the visibility of the segments can be quantified when calculating an averaged mean for different angles. The angle α is defined as the one perpendicular to the z axis and is therefore given by the x

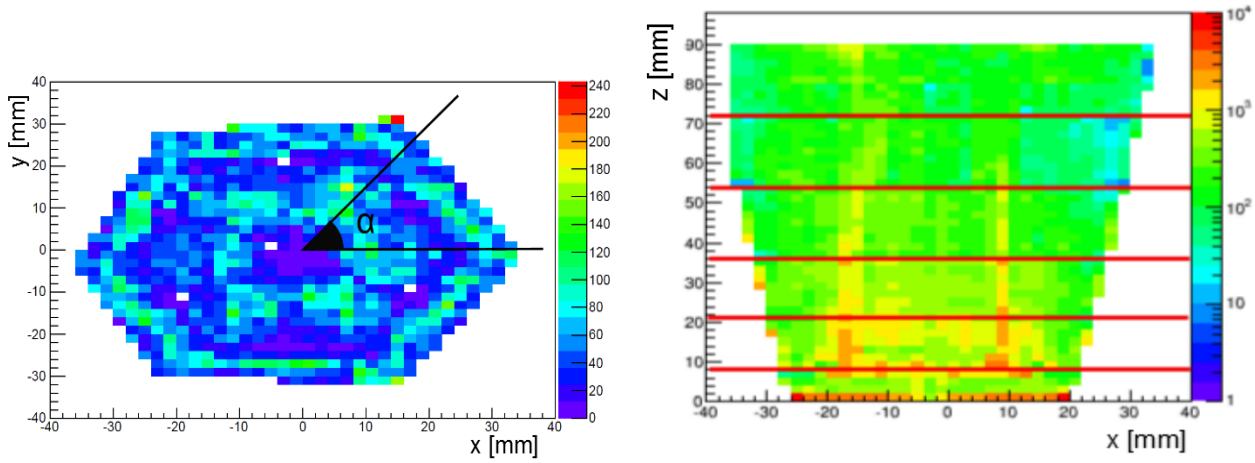

Figure 3.7: Hit distribution in xy and xz depiction of the detector. The structure of the segments is clearly visible though it is not so pronounced in the xz plot. The left plot indicates the defined angle α that is used to investigate the angular dependence. The segment borders are indicated with red lines in the xz plot.

and y coordinates in the following way (as indicated in the simple sketch in Fig. 3.7):

$$\alpha = \arccos\left(\frac{x}{r}\right) \tag{3.13}$$

With $r = \sqrt{x^2 + y^2}$. This only holds true for y ≥ 0 because the arccos can only give values up to π because the cosine is not injective. That means there is more than one possible argument value for one function value. For y < 0 the angle is given by:

$$\alpha = 2\pi - \arccos\left(\frac{x}{r}\right) \tag{3.14}$$

For each grid point in the array the corresponding angle was calculated and the bin content was read out. Grid points belonging to a certain angular range, 20 degrees in this case, were combined and an average mean was calculated. The angular dependence of this average mean is shown in Fig. 3.8. The six-fold structure of the segments can be seen.

3.2.2 Energy and Position Dependence

To further quantify the behavior of the PSA the position dependence of the PSA was investigated to make statements about where the PSA is working better or is having problems. If considering the deviation from the mean and the correlation coefficient in

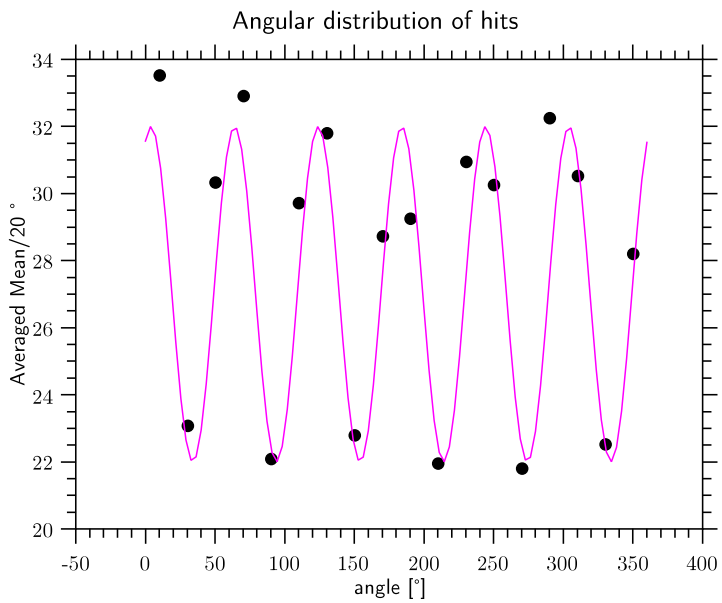

Figure 3.8: The structure of the segments can be seen in the xy-depiction described by the angle α which was fitted by a simple sine function to illustrate the six-fold symmetry.

dependence of the detector depth z an increase at the borders of the segments can be seen. The z dependence for one detector is shown in Fig. 3.9. This behavior suggests that the measured traces do not show the expected behavior at segment borders and that the assumptions made when simulating the AGATA Data Library ADL might be too simplifying. The actual dimension of the segments has also to be considered. The segment borders are not shaped like straight lines. If an interaction took place in a spot that is not considered to belong to the hit segment by the adaptive grid search, then a false PSA result is inevitable. The increases at the segment borders can be seen in every detector. The energy and the depth z of an interaction are not independent. The energy dependence of the PSA has to be taken into account as an improved PSA performance is expected for higher energies.

To complete the analysis of the position dependence the dependence on the radius r has to be treated. Sets of grid points with the same distance to the source were investigated separately. Dividing those sets even more by allocating them to certain radii lowers the amount of grid points that are available for the calculation of the deviation from the mean or the correlation coefficient. This means that they are less significant. For the higher radii at the outer part of the detector there are only grid points for higher z values due to the shape of the detector. The detector has a growing radius r for higher z. This means that

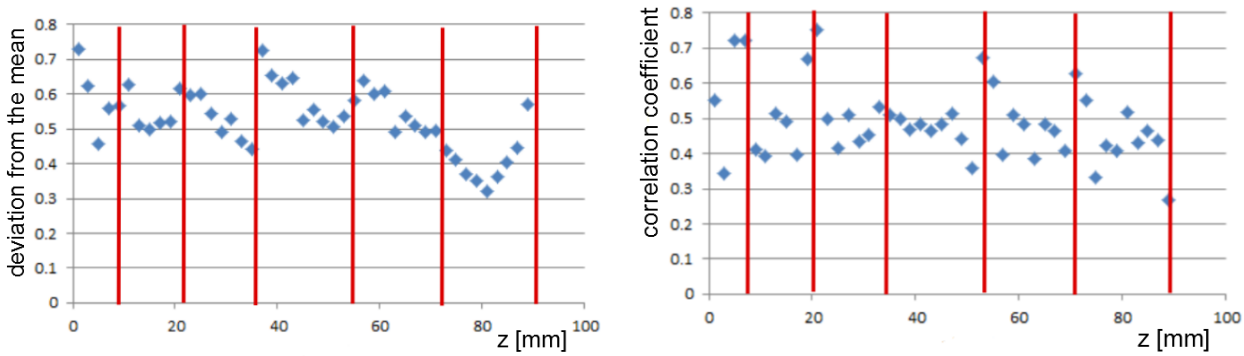

Figure 3.9: An increase in the normalized deviation from the mean and the correlation coefficient, which are described by eq. **??** and 3.11, at the segment borders at 8,21,36,54,72 and 90 mm can be seen. Thus means that the PSA algorithm is not working as well here as in the rest of the detector. The segment borders are indicated with red lines for clarification.

the results for higher r are biased because they are only composed of the behavior of the PSA in the back of the detector. This also means that the corresponding energy is biased.

The radial dependence was investigated but there seems to be no distinct behavior regarding the homogeneity or the clustering. The deviation from the mean increases slightly whereas the correlation coefficient is constant as is shown in Fig. 3.10. The granularity of the radius cannot be increased further because else too few grid points would belong to each analyzed set of grid points for the statistical values to be meaningful.

The energy dependence was investigated. A calibration measurement with ^{152}Eu, containing $2{,}7 \cdot 10^8$ hits, was used. A C++ code was written that fills 2D histograms with hits depending on detector number, depth z and the energy. Gates were set on the peaks of the first most prominent peaks at energies of 75, 84.5, 122, 158.5, 202.5, 244.5, 249.5, 344.5, 510.5 keV with a gate-width of 10 keV. Smaller peaks, especially at higher energies, could not be used due to the low statistics. To secure proper working of the algorithms that calculate the deviation from the mean and the correlation a condition had to be applied that only allowed xy-planes with a mean above a set value to contribute to the net result. This implies that histograms with energy gates at less prominent peaks will more often be rejected, especially for higher z.

The respective gated 2D histograms were analyzed with the introduced algorithms. The obtained results are shown in Fig. 3.11. It can be seen that the two observables seem to get worse for increasing energy opposing to the expectation. There also seems to be some kind

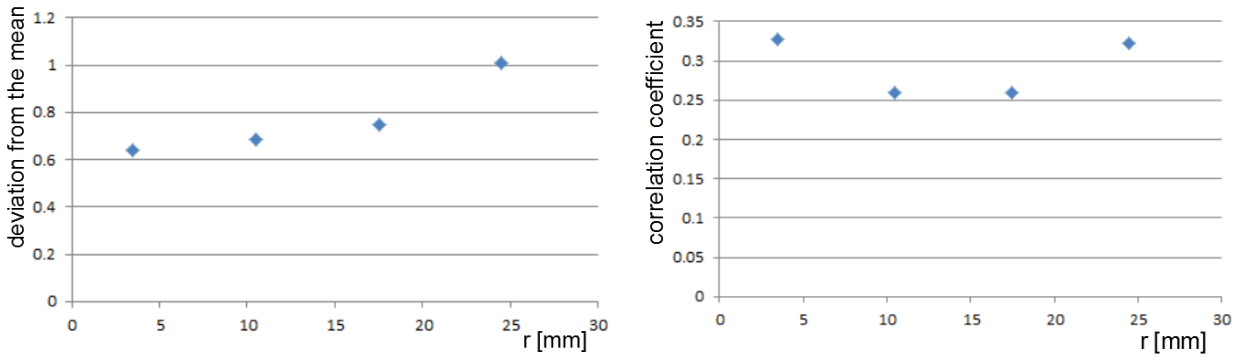

Figure 3.10: The radial dependence of the correlation is essentially constant. The deviation from the mean increases slightly for higher r. The significance of the here shown values is limited by the low amount of grid points for each contributing parameter and due to the z bias at higher r values attributable to the detector shape.

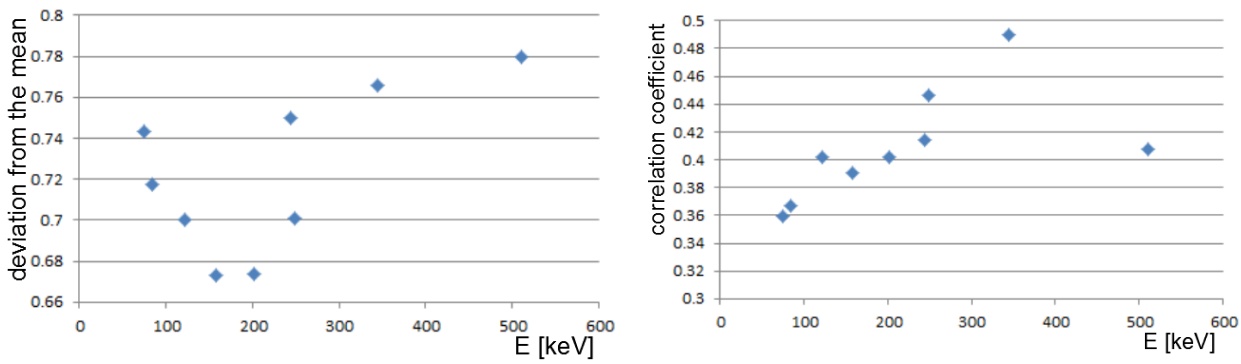

Figure 3.11: Energy dependence of deviation from the mean and correlation coefficient. They both increase for higher energies and there is a minimum around 150 keV.

of minimum around 150 keV. The homogeneity of the distribution of hits is only an indirect measurement for PSA performance. If for example an extreme scenario is assumed where the PSA algorithm failes completely and only allocates hits randomly the homogeneity would suggest optimal PSA performance.

To judge if the homogeneity is a good measure for PSA performance the composition of the introduced observables has to be investigated. The parameter measuring the homogeneity can be split up into two parts. One part $\Delta BC_{\text{intrinsic}}$ is directly depending on PSA performance and gets better when the PSA allocates hits more closely to the physical interaction point. The other part $\Delta BC_{\text{systematic}}$ changes when the PSA shifts hits from one wrong assumed interaction point to another wrong interaction point and thereby making

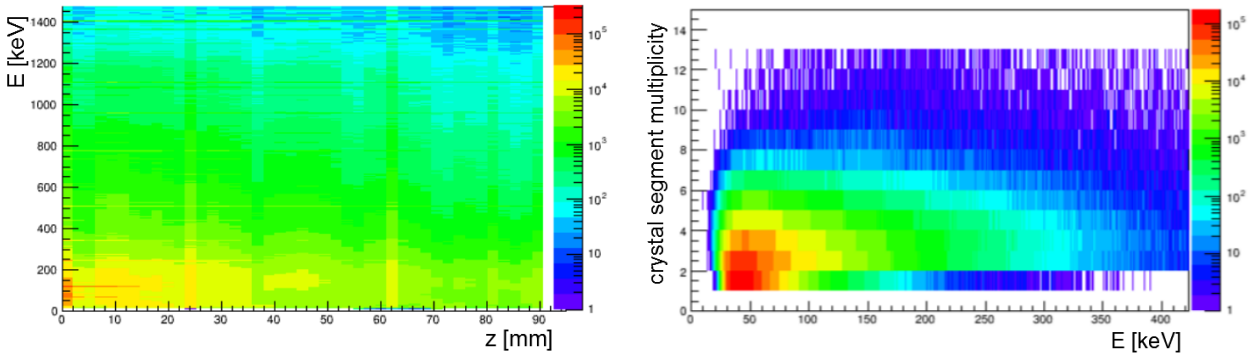

Figure 3.12: Correlation of energy and detector depth z. Certain slices contain too many entries, like at z=24 mm or z=62 mm. The plot on the left shows the correlation between energy and segment multiplicity (restricted to one crystal).

the distribution more or less homogeneous.

$$\Delta BC = \Delta BC_{\text{intrinsic}} + \Delta BC_{\text{systematic}} \tag{3.15}$$

If this second part is random for each individual hit it should be zero in the sum over all interactions. But if there is a systematic part in the behavior in how the PSA shifts events when changing input parameters then it is non-zero. For the case that $\Delta BC_{\text{intrinsic}} \gg \Delta BC_{\text{systematic}}$ the homogeneity of the distribution is a good measure for PSA performance. To get an idea what the ratio of the intrinsic and systematic values are the correlation coefficient is considered. As described in section 3.1.2 the correlation coefficient can be derived by using either a method that is independent of the deviation from the mean or by using ΔBC^2 as normalization parameter. The correlation coefficient consists of an intrinsic and systematic part as well.

$$\eta = \eta_{\text{intrinsic}} + \eta_{\text{systematic}} \tag{3.16}$$

With

$$\eta = \frac{\text{cov}}{\Delta BC^2} = \frac{\text{cov}_{\text{intrinsic}} + \text{cov}_{\text{systematic}}}{(\Delta BC_{\text{intrinsic}} + \Delta BC_{\text{systematic}})^2} \tag{3.17}$$

This means if the deviation from the mean is governed by $\Delta BC_{\text{systematic}}$ the correlation coefficient η is also governed by it. So if both parameters show the opposite behavior, i.e. if one goes up and the other falls off over a certain parameter range, then it is reasonable to assume that the systematic part is non negligible and that both parameters are not a good measure for PSA performance. If they have a minimum at the same position then

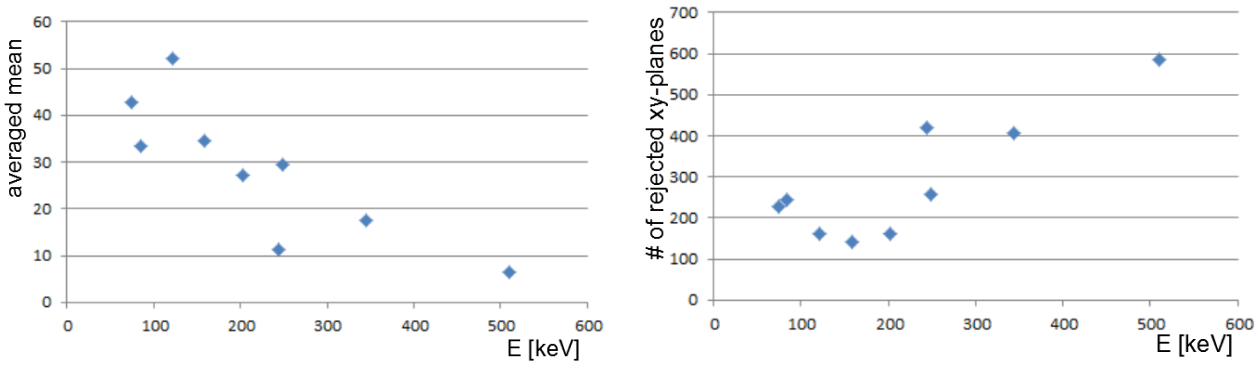

Figure 3.13: On the left the average mean over all xy planes is shown in dependence of the energy. On the right the number of rejected xy planes that could not contribute to the analysis due to low statistics is shown. The overall number of xy planes is 675.

it is relatively safe to assume that this comes from the intrinsic change. This means that a cross check for consistency is always necessary. The minimum around 150 keV can also be seen in the correlation coefficient but it is not as significant. There is no correlation between energy and multiplicity as shown in Fig. 3.12, so this is no explanation for the increase at higher energies.

The average mean in dependence of the energy is shown in Fig. 3.13. The right plot shows the number of rejected xy-planes. More xy-planes are rejected at higher energies due to too low statistics. A xy-plane was rejected if the corresponding mean was below 10. The number of xy-planes is 45 for each detector which gives 675 xy planes overall. For the 510 keV energy gate almost all xy planes were rejected which leads to a strong correlation to the detector depth z. There is a small dip in the number of rejected xy planes around 150 keV which has no corresponding counterpart in the average mean. This could explain the behavior of the homogeneity of the distribution around 150 keV.

The investigation of the energy dependence poses some difficulties when done with the presented methods. The energy dependence cannot be treated independent of the detector depth z. For higher energies the statistics are too low so that xy-planes at the back of the detector cannot be included. The distribution of hits in z dependence is shown in Fig. 3.14. As energy and z are not uncorrelated this might explain the observed behavior of the homogeneity. The homogeneity of the distribution of hits is not a good tool to extract the energy dependence of the PSA performance as systematic effects dominate. Therefore, it was investigated with another method which is shown in section 3.2.3.

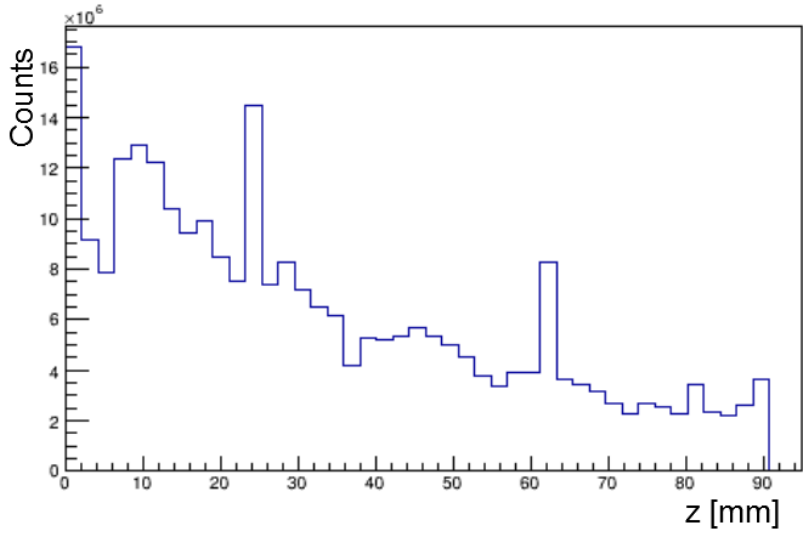

Figure 3.14: Histogram for the allocated z position. An increase at z=24 mm and z=62 mm can be seen. The PSA falsely allocates interactions there. This effect can be observed for all energies and all detectors.

3.2.3 χ^2 distribution

While searching the interaction point the PSA algorithm minimizes a figure of merit that is defined as

$$\text{Figure of Merit} = \sum_{i,j} |A^s_{i,j} - A^m_{i,j}|^p \tag{3.18}$$

$A_{i,j}$ is the amplitude or signal height at the time i of segment j for the measured m or simulated s signals respectively. If the phrase amplitude is used in the following sections then this time dependent amplitude, that describes the value of the signal at time index i, is meant. The loop over the segments involves the hit segment, its direct neighbours and the core. Segments that are not direct neighbours of the hit segment see barely no transient signals and can be neglected by the PSA. The figure of merit is calculated for every grid point in the hit segment with a set of simulated signals belonging to every grid point. The fit of the simulated traces is best where it is is minimal. The parameter p is set to 0.6 in all plots presented in this section. Its absolute value still contains information about the quality of the best fit. In the standard setup the figure of merit is not passed from the PSA producer to the tracking filter. In the online analysis the amount of data that is passed should be minimized to ensure a fast algorithm. For offline analysis it is possible to use that additional information. Therefore, the Narval emulator femul that replays the data offline was modified and this value was added to the data block which is

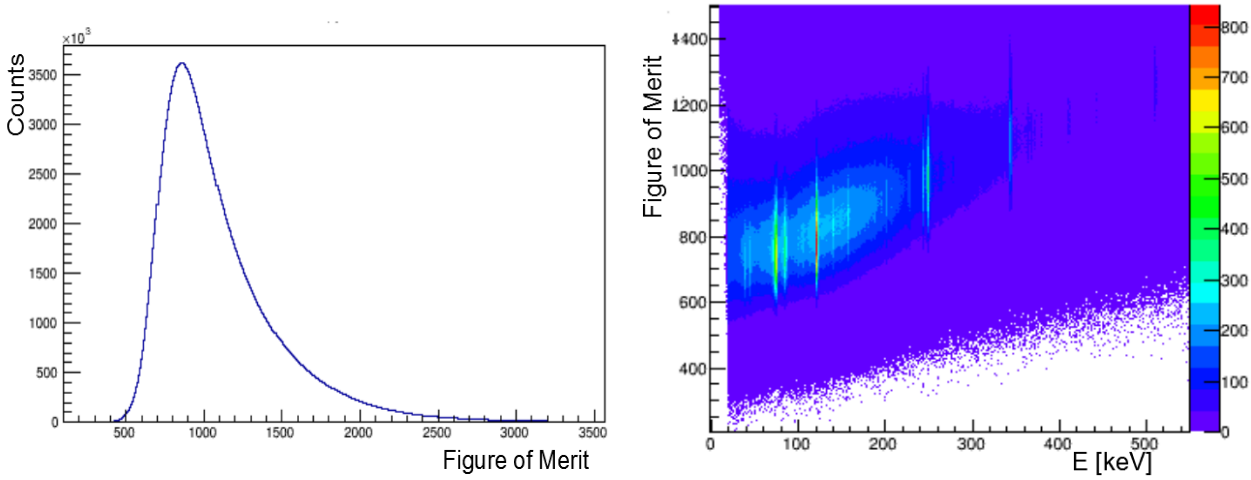

Figure 3.15: The distribution of the figure of merit and its energy dependence is shown on the left and on the right respectively. The figure of merit has a systematic energy dependence and a normalization is necessary

passed from the PSA producer to the tracking. The tracking filter was modified so that the figure of merit is added as a branch to the final root tree. This allows to investigate each hit by examining the corresponding value of the figure of merit. Its distribution is shown in Fig. 3.15.

The absolute value of the figure of merit for the best fit contains information about how well the calculated traces match the measured ones. If the value is very high it can be assumed that the physical interaction did not actually take place at the allocated position. To use the figure of merit as a tool to divide hits into good or bad agreement a systematic energy dependence has to be removed, see Fig. 3.15 on the right. A reasonable assumption is that the difference of the amplitudes is proportional to the deposited energy:

$$|A^s_{i,j} - A^m_{i,j}| \propto E \Rightarrow \text{Figure of Merit} \propto E^p \tag{3.19}$$

The 2D histogram displaying the energy dependence of the figure of merit after a normalization by E^p is shown in Fig. 3.16. The normalization by E^p does not lead to a constant value for the figure of merit. This suggests that there is a remaining intrinsic energy dependence. As stated in previous sections the PSA should work better at higher energies causing smaller figure of merit values. Fig. 3.16 shows the intrinsic energy dependence of the PSA performance. The normalized distribution of the figure of merit has a similar shape as the original one.

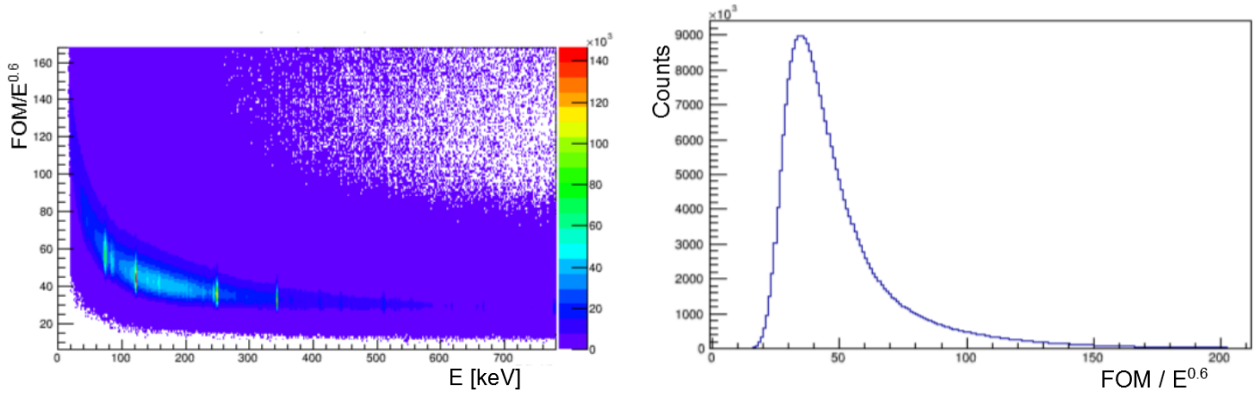

Figure 3.16: By eliminating the systematic part of the energy dependence of the figure of merit the intrinsic dependence can be observed. The right plot shows the normalized distribution of the figure of merit.

The normalized distribution holds the relevant information about how well simulated and measured traces match and allows to gate on events with good or bad matching of simulation and measurement. The energy spectrum or the hit distribution can then be investigated for those events. Fig. 3.17 shows the energy spectra for the conditions Figure of Merit/$(E)^p < 35$ and Figure of Merit/$(E)^p > 70$ for $p = 0.6$. The former has more entries at higher energies than the ungated spectrum. The latter only has entries for small energies. It is unexpected that the second spectrum does not show the structure of the ungated energy spectrum. There are nearly no peaks visible. The measurement without a gate on the figure of merit in Fig. 3.3 shows several peaks in the energy range up to 350 keV. It should have no impact on PSA performance whether the interaction was a photoeffect or Compton scattering. The second spectrum of Fig. 3.17 consists almost only of background and the very dominant peaks at 84, 159 and 244 keV miss completely. This behavior is not expected and unexplained because a bad matching of measurement and simulation should have no impact on the actually deposited energy in the interaction.

The gating on the normalized figure of merit is used for the investigation of the hit distributions. In Fig. 3.18 the hit distributions for z = 8 to 10 mm and the same figure of merit gates as above (smaller than 35 and greater than 70) are displayed. To compare both distributions the different numbers of entries have to be considered. The left one with the gating on good matching of simulated and measured traces has a total of $1.65 \cdot 10^5$ hits whereas the total number of hits in the right one is $1.25 \cdot 10^5$. If the normalized figure of merit value has no influence on where hits are allocated by the PSA then it is expected to

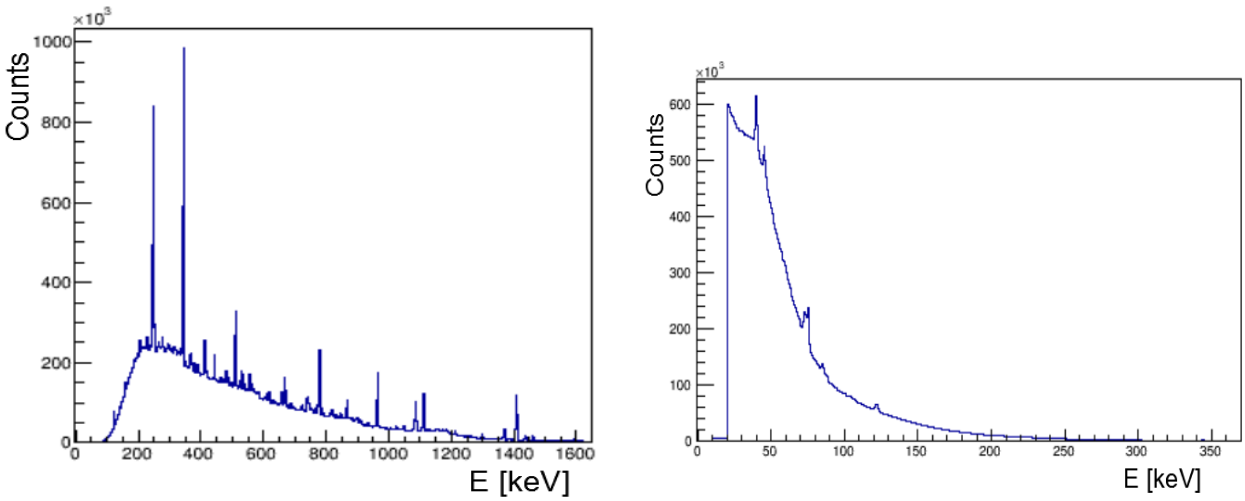

Figure 3.17: Energy spectra of ^{152}Eu with gating on good (left) and poor matching of traces (right). The latter only has entries at smaller energies and no clear peaks are visible.

	deviation from the mean	correlation coefficient
$\frac{FOM}{E^{0.6}} < 35$	0.91	0.45
$\frac{FOM}{E^{0.6}} > 70$	1.14	0.41

Table 3.1: Deviation from the mean and correlation coefficient for gating on different figure of merit values.

find a drop in statistics uniformly over the shown xy plane. It can be seen in Fig. 3.18 that the single grid points with too high statistics at the edge of the detector miss completely on the plot with the gating on good agreement of simulation and measurement.

The color scale in those hit distributions is defined by the grid point with the highest number of entries. If the ratio of the statistics of that one grid point and the average is very high less clustering is visible. A distribution seems to have less clustering if there is one grid point with especially high statistics (though it is still present). Both distributions were analyzed with the algorithm for the deviation from the mean and the correlation coefficient. The results are shown in the following table.

The deviation from the mean improves when gating on the good events whereas the correlations more or less stays constant. The normalization on the mean μ^2 was used for the correlation coefficient. The change of the deviation from the mean mainly comes from the existence of the single high statistic grid points. The existence of a single high statistic

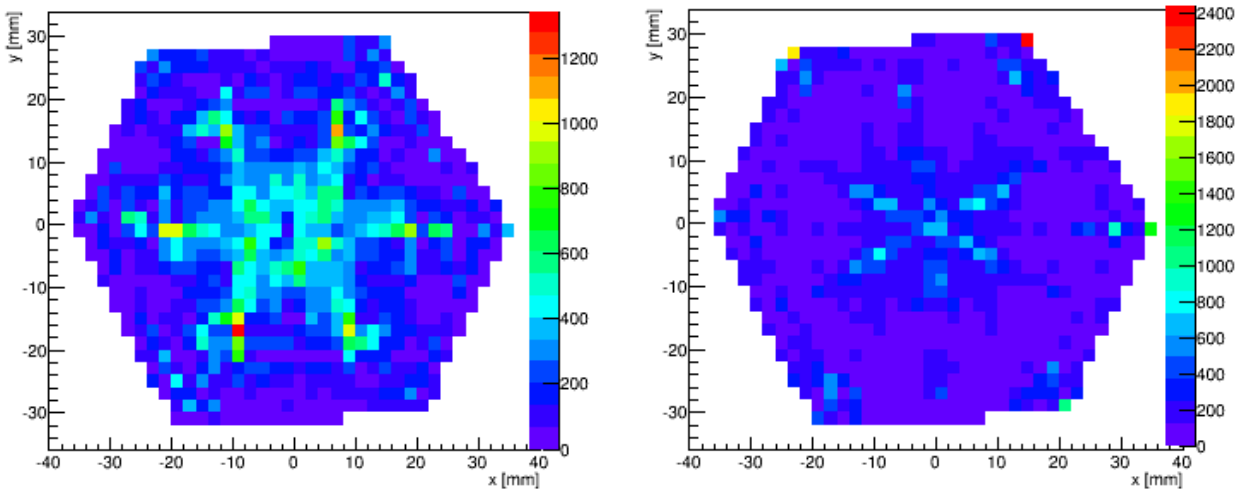

Figure 3.18: Hit distributions for good (left) and poor (right) matching of simulated and measured traces. The xy plane for z= 8 to 10 mm for one detector is shown exemplary. The single grid points with extreme high statistics at the edge of the detector only exist in the right plot.

grid point also has an impact on the correlation coefficient because the deviation from the neighboring grid point is very high. This does not describe the clustering in the middle of the detector.

The figure of merit cut can be used to get rid of the single high statistic grid points at the edge of the detector. Events that are allocated here by the PSA have a poor agreement with the simulation. These events should not be rejected but their interaction position could be set to the center of the segment. The average deviation to the physical interaction point is smaller this way. The clustering seems to be merely independent of the figure of merit. A possible interpretation is that events in the single high statistic grid points show high deviations of the measured traces compared to the simulated ones. The clustering however is caused by events that have relatively good matching. For the clustered events it is reasonable to assume that the physical interaction point is only some milimeters away from the allocated one. There is some systematic shift of events to the center of the segments, possibly due to an incomplete description of detector characteristics.

For a further analysis a map of the distribution of the figure of merit was created and compared with the hit distributions. By this an assignment of a value for the figure of merit for every grid point in the detector is meant. Every grid point has a multiple number of hits; only a mean value can be assigned. An algorithm was written that reads out the

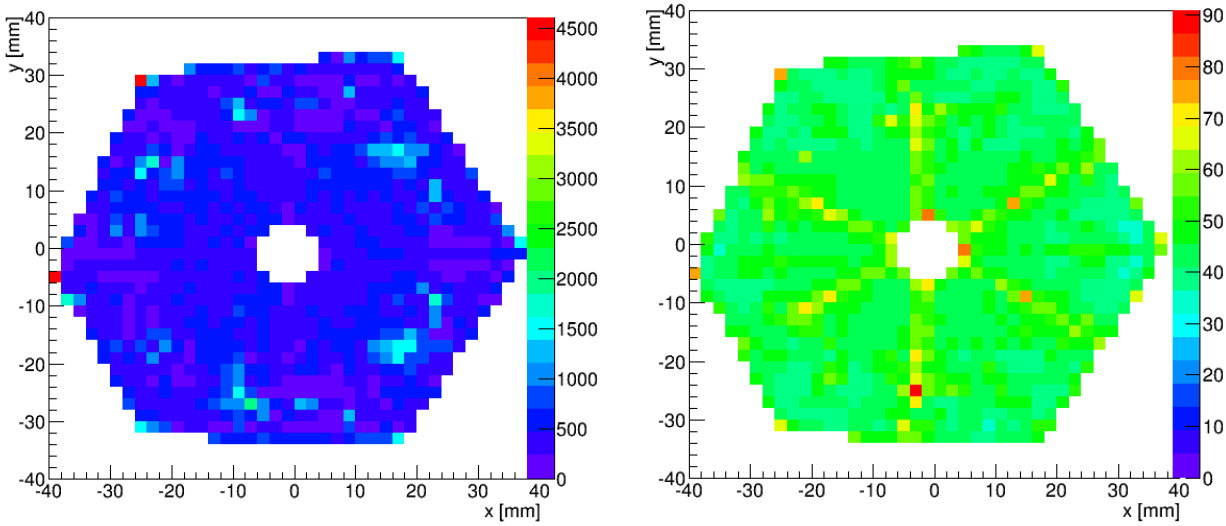

Figure 3.19: The comparison of the hit distribution (left) with the corresponding average value for the figure of merit (right) is shown for a detector depth of z = 30 mm. The ^{152}Eu measurement was used. No further cuts on energy were used. An increase in the figure of merit at the same spot where the hit distribution has single high statistic grid points can be seen. The six fold structure of the segments with an increase at the segment borders can also be observed.

figure of merit for every hit, calculates a mean value and fills histograms for every grid point in every detector. This allows the calculation of a position dependent average value for the figure of merit. This averaged figure of merit value is filled into 2D histograms which allows a direct comparison with the hit distributions.

The mapping of the figure of merit value allows several observations. There is an increase in the figure of merit at the same spot where the hit distribution has a single high statistic grid point which can be seen in Fig. 3.19. A second observation is that the 6 fold structure of the segments is always visible in the distribution of the averaged figure of merit. There is an increase at the segment borders which also fits to the previously made observation that the PSA has problems to describe the traces correctly at the segment borders. The PSA tends to allocate hits more to the middle of the segment. Regarding the clustering effect an anticorrelation of bin content and average figure of merit can be observed. Areas of the detector which show a clustering of hits typically have a low figure of merit value and vice versa. In the middle of a segment measured and simulated traces match better. The bad matching at segment borders either leads to the observed high figure of merit

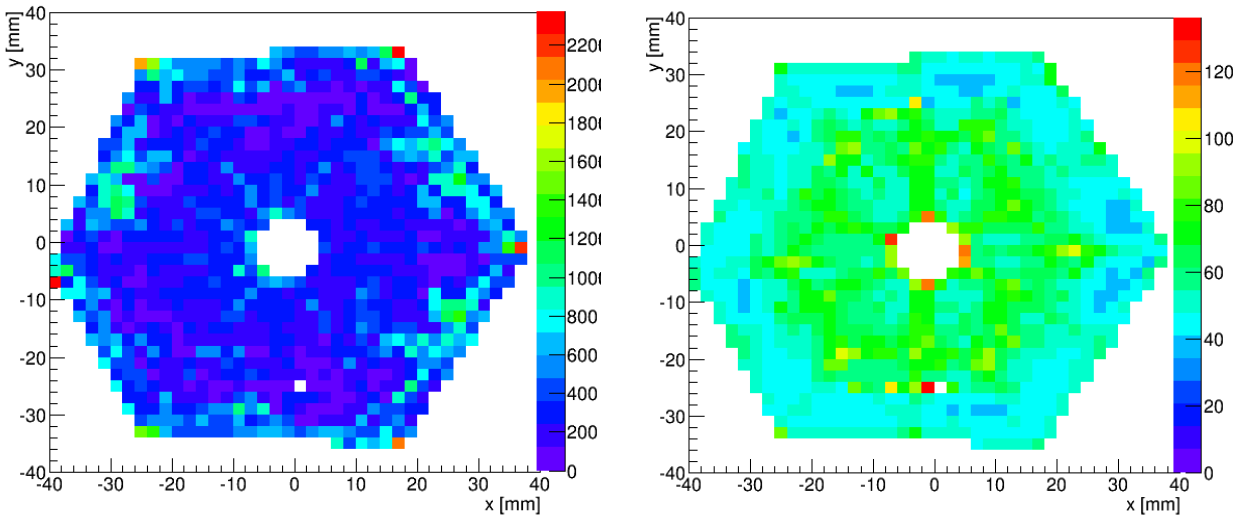

Figure 3.20: Same comparison of the hit distribution (left) with the figure of merit (right) for a detector depth of z = 36 mm is shown. At points with clustering of hits the corresponding figure of merit value is low.

values or the falsely allocation at grid points with similar traces.

3.2.4 Multiplicity

The impact of the segment multiplicity on the homogeneity of the distribution and the PSA performance was investigated using the ^{152}Eu source run. Multiple interactions in one crystal lead to the superposition of the transient signals. This is relevant if the considered segments for the influenced charges are direct neighbors. If both hit segments are direct neighbors then the real signal is slightly altered by the influenced mirror charges. The superposition of the both charge collection processes can be described by the PSA, but a higher complexity of the problem increases the probability that the algorithm cannot resolve the pulses properly. The impact of overall segment multiplicity on the homogeneity of the hit distribution and the correlation is shown in Fig. 3.21. This multiplicity describes the number of hits for one event considering the whole AGATA demonstrator array. The superimposed hit distributions of all detectors were investigated. This first approach is questionable since each detector should be investigated on its own. Else information could be lost due to the superposition of the hit distributions of all detectors. The obtained results are not significant which can be seen by comparing the behavior of the deviation

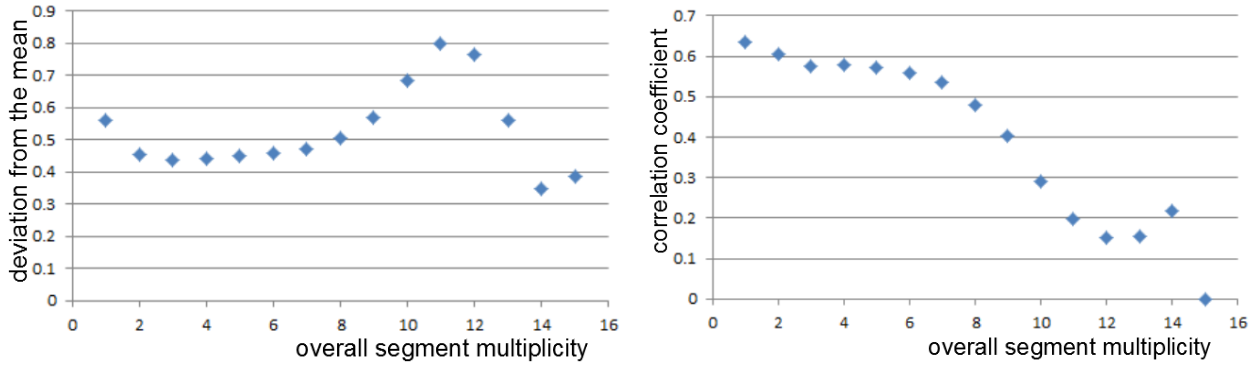

Figure 3.21: The deviation from the mean (left) and the correlation coefficient (right) in dependence of overall segment multiplicity are shown. The behavior is not consistent which arises from the array wide multiplicity definition that was used. The hit distributions of all detectors had to be superimposed.

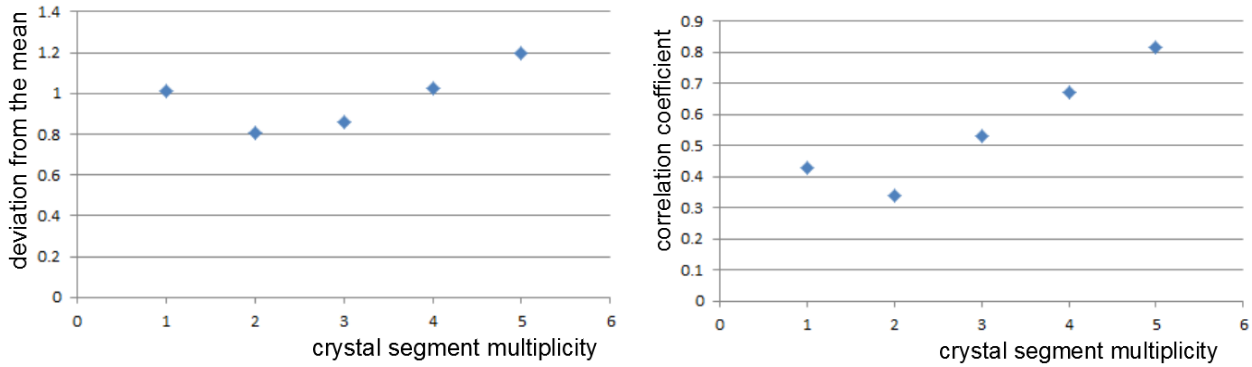

Figure 3.22: The PSA performance in dependence of the crystal segment multiplicity is shown. Only values up to a crystal segment multiplicity of 5 are shown because the statistics are not sufficient for higher values to perform the statistical analysis. The expected increase for higher multiplicities can be observed for the correlation coefficient on the right but there is also an enhancement for single interactions with m=1.

from the mean with the correlation coefficient, see Fig. 3.21. A reverse behavior of both values can be observed. This means that the systematic change has a higher impact than the one caused by changes in PSA performance as described previously in chapter 3.2.2.

To find a better approach a C++ program was written looping over the complete data and adding up the hits of every event to get a multiplicity value for each individual crystal for every event. This allows to fill 2D histograms for every detector and every xy plane gated on the corresponding crystal multiplicity. These histograms can then be analyzed.

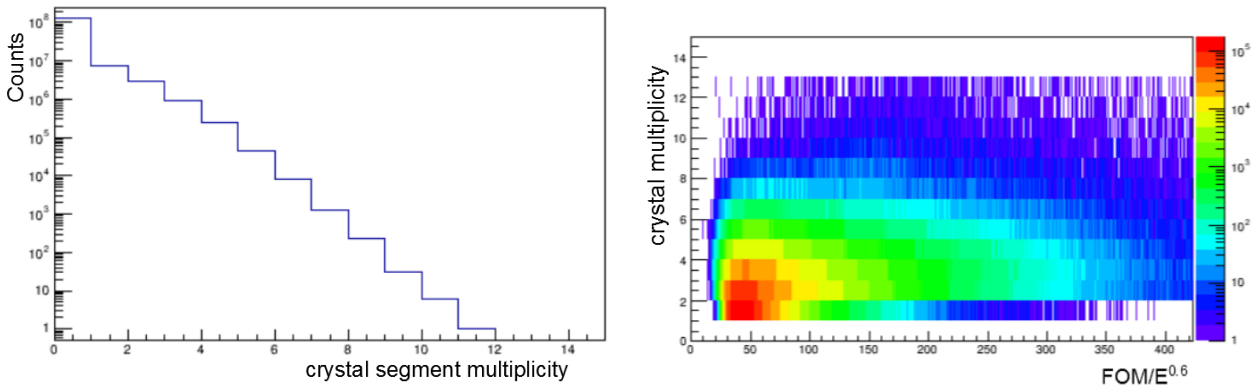

Figure 3.23: The distribution of the crystal multiplicity is shown on the left. The right plot shows a 2d spectrum with the normalized figure of merit on the x-axis and the corresponding crystal segment multiplicity on the y-axis.

The results are shown in Fig. 3.22. The expected increase for higher multiplicities can be observed but there is also an enhancement for single interactions with multiplicities of m=1. This can be observed in both the deviation as well as in the correlation in a self consistent way. For two interactions in a crystal most of the time the hit segments are not direct neighbors and do not interact too much with each other. However the core signal is the sum of the charge collection of both hit segments. For the core signal the noise to signal ratio is better if both signals are superimposed. This could explain the improvement in PSA performance. For comparison the dependence of the normalized figure of merit on the crystal multiplicity is shown in Fig. 3.23.

3.3 Variation of Producer Parameters

To try and optimize the PSA performance a better understanding of detector characteristics relevant for the PSA has to be reached. The expected signals after charge collection are the starting point. Corrections for a more realistic pulse have to be included. For example the electronics of preamplifiers and digitizers alter the measured signal. On the other hand there are ways to improve the algorithm itself which are not directly correlated with detector properties. These are improvements of the comparison of the measured and simulated signals, e.g. a variation of the starting time of each signal of an event.

3.3.1 Distance Metric

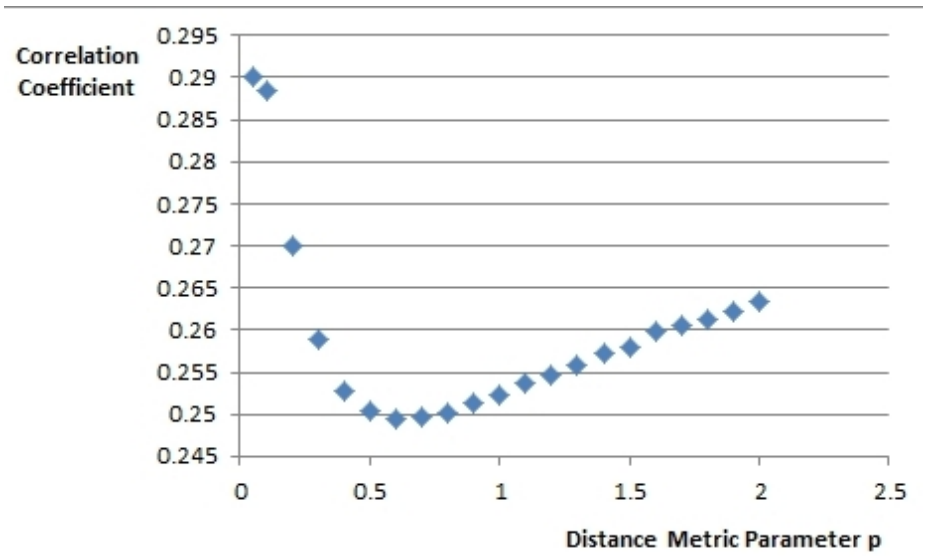

Figure 3.24: Correlation coefficient against chosen distance metric defined by the exponent $p > 0 \in \mathcal{R}$. A pronounced minimum around 0.6 can be observed. The optimal distance metric depends on the distribution of the difference of the measured and simulated amplitudes $A_{i,j}^{m,s}$ and the optimal weighting of the transient signals compared to the net signal.

When comparing measured and simulated signals the already introduced figure of merit is used as minimization variable, see eq. **??** At which grid point the minimum is found depends on the choice of the exponent p, which is a real number greater zero. The correct choice of p depends on the distribution of the difference of the amplitudes $A_{i,j}^{m} - A_{i,j}^{s}$. In general a Gaussian distribution around zero is expected as the simulated signal sometimes over- or underestimates the real signal, mainly due to noise. The measured amplitude $A_{i,j}^{m}$ varies around its expectancy value due to the statistical nature of the charge collection. If the distribution is not Gaussian then this implies systematic deviations of the measured and simulated signals.

The value that is chosen for the exponent p decides the metric that the figure of merit follows. A metric is a distance function that assigns a non negative real number to two elements of a space. A value of $p = 2$ corresponds to an Euclidian metric and the space is called an Euclidian space. Since the absolute value of the difference is used for the figure of merit it is a metric for every positive real value of p. Different values of p affect how the algorithm performs the comparison of measurement and simulation. A very high value

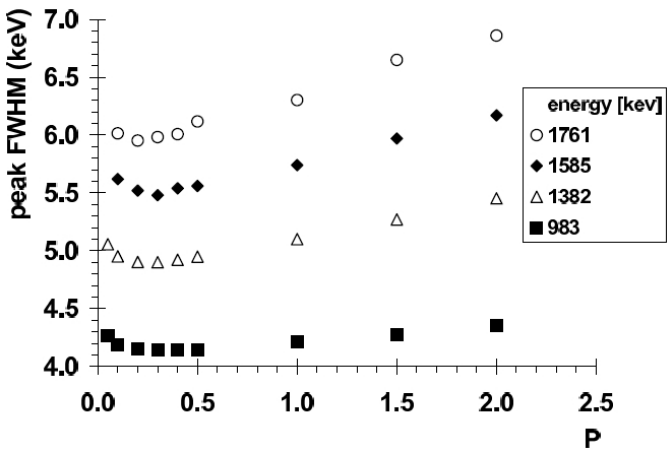

Figure 3.25: FWHM values of Doppler corrected peaks in dependence of the used distance metric from a work of Francesco Recchia. In that work a value of p = 0.3 was chosen though the position of the minimum is not resolved very well especially for the smaller energies. [23]

of p corresponds to a strong weighting of large deviations of the measured and calculated signals. These large discrepancies, that may appear only within a short time interval, dominate the composition of the figure of merit for large p. These large deviations mostly occur in the comparison of the signals of the hit segment and the core. Smaller values of p do not disfavor single large deviations from the measurement as much. Smaller values of p require that the overall matching, considering also the transient signals, has to be good. The small transient signals have a higher impact on the PSA result if a smaller value for p is chosen. A Gaussian like distribution of the difference of the amplitudes $A^m_{i,j} - A^s_{i,j}$ implies optimal PSA results for an Euclidian Metric. However if there are deviations higher than expected for a Gaussian distribution optimal results will be obtained for values of p smaller than 2.

It is difficult to derive the optimal value for the exponent by analyzing the distribution of the difference of the amplitudes. Instead an empirical approach was used. The parameter p was varied in steps of 0.1. The ^{152}Eu source run was replayed with the Narval emulator femul for every individual value of p. The replayed data was analyzed with the Watchers to create a root tree containing information about energy and the interaction position within the crystal. The Watchers have the advantage that the position information for each interaction is given in the basis of the crystal and not in the lab system like in the root tree created by femul. This simplifies the data analysis with the introduced algorithm for the determination of the correlation of neighboring grid points. For every implemented

distance metric a final value is derived that describes the PSA performance of the whole array as shown in section 3.1.2. All other PSA parameters are kept constant. The results are displayed in Fig. 3.24 and suggest $p = 0.6$ as an optimal value. The value that was used before was chosen to p = 0.3 by Francesco Recchia [23] after analyzing the width of Doppler corrected peaks shown in Fig. 3.25. In Recchia's work the minimum was not pronounced.

It is difficult to disentangle the two quantities that determine the optimal value for the distance metric. These are, as discussed, the distribution of the difference of the measured and simulated amplitudes and the weighting of the transient signals compared to the net signal. This weighting was discussed in section 2.2.2. To check the obtained results for consistency the variation of p was performed using the quality of the Doppler correction as criteria. The obtained results are presented in section 3.3.1.

Optimization via Doppler Correction

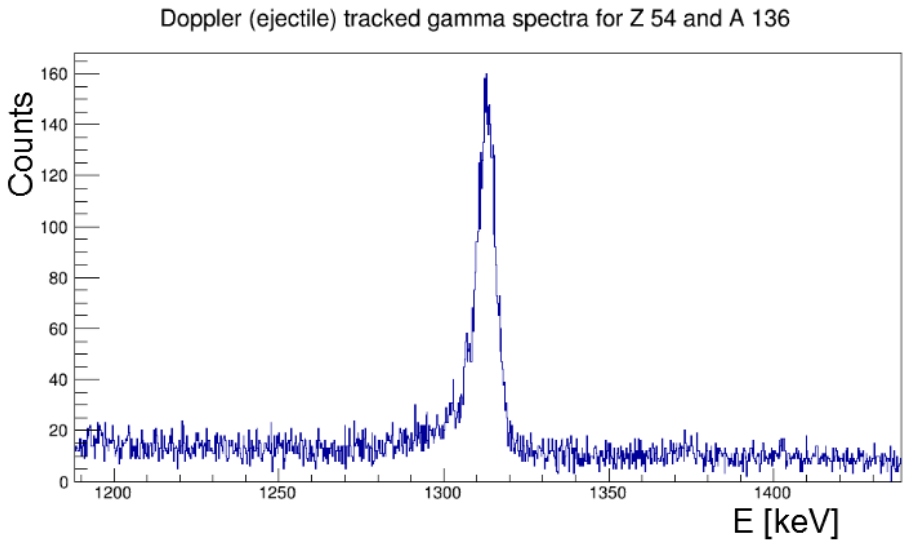

Figure 3.26: Doppler corrected and tracked ejectile spectrum for ^{136}Xe with a zoom on the prominent 2^+ transition at 1313 keV. The peak was fitted with a Gaussian that allowed left tailing to derive the corresponding FWHM value of about 6.5 keV.

The in beam experiment at the Legnaro National Laboratories (LNL) 11.22 was investigated for this purpose. A 1 GeV ^{136}Xe beam was shot on an ^{238}U target to induce multi nucleon transfer reactions. For examination of the PSA performance the Doppler corrected γ-spectra were analyzed. The identification of the reaction products via Z,q and A

identification with the PRISMA mass spectrometer was taken from Andreas Vogt [27, 28]. Benedikt Birkenbach contributed the implementation of the Doppler correction in the data analysis [4]. The quality of the Doppler correction depends directly on the position resolution of the first interaction in the array. This first interaction point is derived from the tracking which relies on the PSA. The quality of the Doppler correction is therefore a measure for PSA performance.

	E [keV]	Volume V	FWHM [keV]	Δ FWHM [keV]
^{136}Xe	1313	1080	6.53	0.21
^{137}Xe	1219	324	7.46	0.28
^{135}Xe	1131	247	6.47	0.57
^{138}Xe	589	150	4.4	0.24
^{138}Xe	483	275	4.03	0.18
^{134}Xe	847	232	4.42	0.37

Table 3.2: Fit results for the different transitions for a fixed value of $p = 0.6$. The relatively small volumes of the peaks cause higher errors. For the further analysis only the $2^+ \rightarrow 0^+$ transition from ^{136}Xe is considered.

For a precise and reliable determination of the peak width only those with a reasonable amount of hits were considered. Therefore, only the beam like particles were investigated. The channels with not more than ± 2 neutrons were analyzed. The best spectrum was the one from the beam itself, where the 2^+ state at 1313 keV was populated most prominently. It consists of about $2.49 \cdot 10^5$ entries. The peak width was analyzed in dependence on the chosen distance metric. The low number of hits contributing to the peak is problematic. It causes a relatively high error of the fit that is in the order of 0.1 to 0.2 keV. This is comparable to the peak width changes due to the different metrics. The peak to total ratio given by the volume of the peak relative to the integral of the complete spectrum is also a measure for the performance of the tracking. The results regarding the width and volumes of the peaks corresponding to the different transitions of the considered nuclei are shown in table 3.2. It shows the small volumes of the peaks and the errors of the fits. Only the 2^+ transition of ^{136}Xe at 1313 keV has enough statistics.

The results for the peak widths and the peak to total ratios regarding the optimization of the distance metric is shown in Fig. 3.27. There is no change observable because the variation is in the order of or smaller than the respective errors. The errors for the fit of the peak are in the order of 0.2 keV and the FWHM value changes only in the range of up to

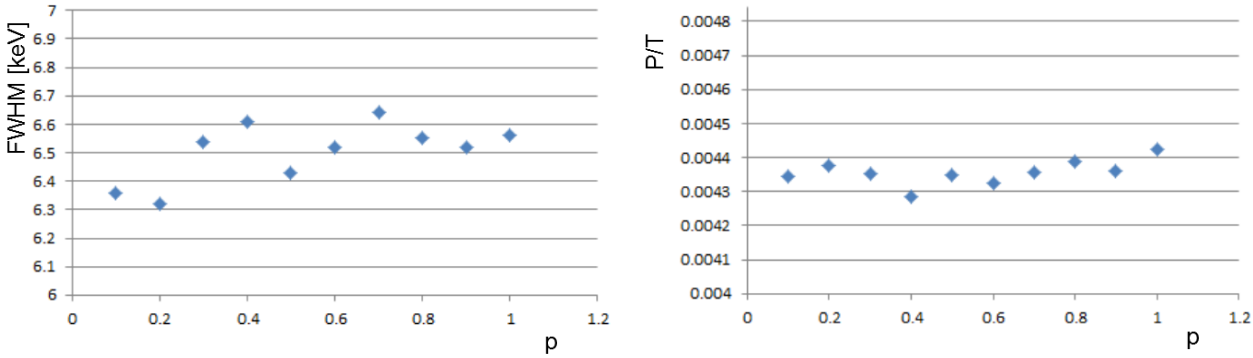

Figure 3.27: The Doppler corrected FWHM values (left) and the peak to total ratio (right) of the 2^+ transition of ^{136}Xe after tracking in dependence on the used metric is shown. Both values stay constant within the observable resolution. They change in the order of their errors which are 0.2 keV for the FWHM values and 33 for the volume of the peak.

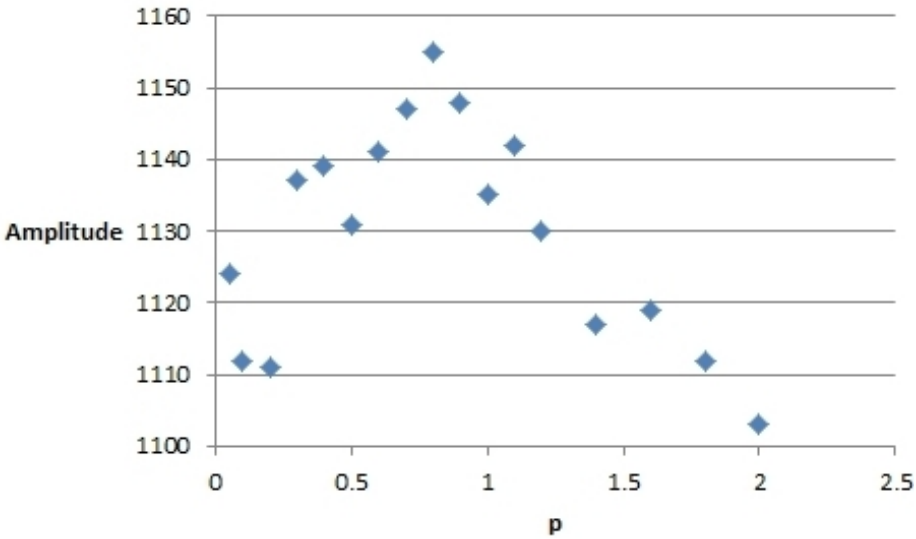

Figure 3.28: Amplitude of the 2^+ transition of ^{136}Xe in a spectrum with reduced binning of 4 keV per bin. The amplitude is a measure for peak width. The determination does not depend on starting parameters like for the Gaussian fit. A more distinct behavior with a pronounced maximum can be observed which implies an optimum value around $p = 0.8$

0.4 keV. This makes it very hard to see an underlying dependence. The same problem exists for the peak to total ratio. The average peak volume is about 1090 entries with an average error of 33. Variations of the volume when changing the distance metric are all in the order of or smaller than this error. Small variations of the PSA parameters do not affect how an

event is treated by the tracking most of the time. To extract more useful information the peak width was replaced with the amplitude of the peak as criteria. Higher amplitudes correspond to smaller peak widths and therefore a better Doppler correction. Using the amplitude as criteria has the advantage that the derived value does not depend on initial conditions of the Gaussian fit. These initial conditions are the background estimation, peak position and the energy range that is considered by the fit algorithm. Like in all converging algorithms choosing the starting values may have an impact on the final result. It could be observed that already slight variations of starting parameters changed the final fit results. Using the amplitude of the peak as optimization value requires the binning of the spectrum to be reduced to avoid random stacking of events in single bins. The width of one bin was set to 4 keV. As the tracking does not depend strongly on the PSA the background could be assumed to be constant for all values of p in good approximation. The results are shown in Fig. 3.28. They suggest an optimal value of $p = 0.8$ which is slightly above the results using the correlation method. There might be some deviations due to the different experimental conditions of the two measurements that were used. The correlation method uses a calibration run which has different conditions regarding counting rate and multiplicity. This may impact how the difference of the amplitudes $A^m_{i,j} - A^s_{i,j}$ behaves, e.g. due to a more unstable baseline. This would in turn make the distribution more Gaussian like and favor a higher values for p.

3.3.2 Comparison of Traces

To extract further information on the distribution of the difference of the amplitudes $A^m_{i,j} - A^s_{i,j}$ the measured and calculated traces were analyzed. The traces were extracted while performing the replay of the data. For every event the measured and calculated signals were written to file for every segment and the core. The PSA only uses the first 56 samples, corresponding to 560 ns, after the trigger at T_0. The trace for a segment or the core contains 4 empty samples at the end. This corresponds to $37 \cdot 60 = 2220$ data points for the measured signal of one event. Out of those $37 \cdot 4 = 148$ are zero by default. For every measured signal the best fitting calculated signal is read out. The event energy, time shift, hit segment and position information is given at the end of the data block that contains the measured and calculated signals. The written traces correspond to a long list of numbers and the relevant information were acquired with an adequate algorithm.

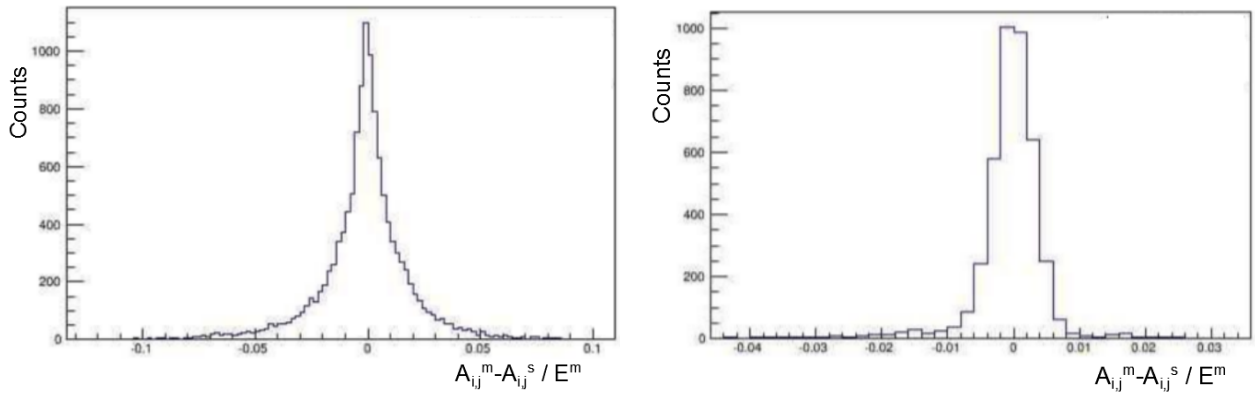

Figure 3.29: The normalized distribution of the difference of the measured and calculated amplitudes $\frac{A^m_{i,j}-A^s_{i,j}}{E^m}$ is shown for two positions in the detector. The first position corresponds to the distribution on the left where the normalized figure of merit value is considerably above average whereas on the right it is below average. The distribution on the left shows strong tailing and is non Gaussian. The distribution that corresponds to a low figure of merit is much narrower and more Gaussian like.

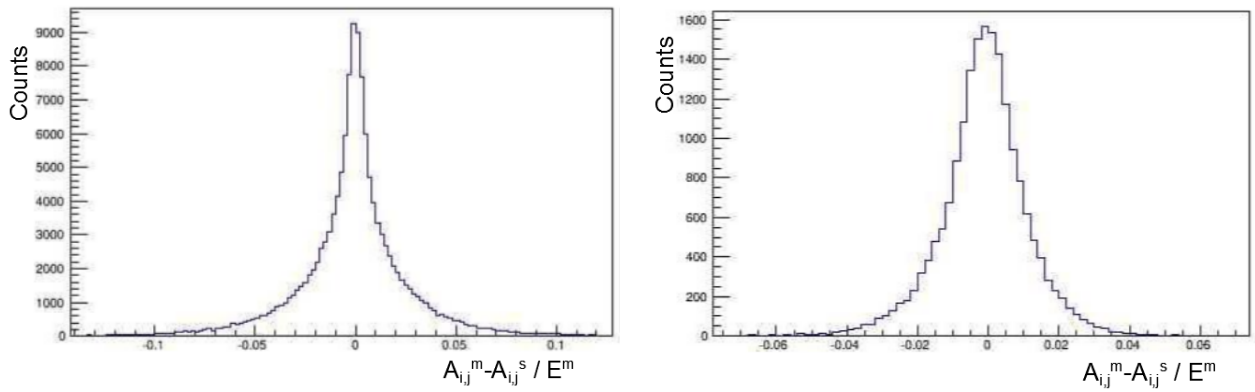

Figure 3.30: The normalized distribution of the difference of the measured and calculated amplitudes for two different positions in the detector. In contrast to Fig. 3.29 they are selected by their number of entries relative to other points in the detector with the same distance to the source. The left plot shows the distribution for all events that were allocated to one single high statistic grid point. This point has too many entries to be explained by random statistical fluctuation. The right one is a typical point in the detector that does not show a distinct statistical in- or decrease or clustering.

The traces for certain grid points of the detector were compared. Those are points where the matching of measured and calculated signals is good or poor (see figure of merit distributions in section 3.2.3), or points where the PSA is assumingly not working well, like for the single grid points with too high statistic. A typical grid point with an average number of hits was also investigated for comparison. This was done for grid points with high and low values of the figure of merit respectively. The difference of the amplitudes was calculated for every sampling point of the signals from the segments and the core. The difference of the amplitudes is proportional to the energy that was deposited. Therefore, a normalization was performed so that the value contributing for every sampling point is:

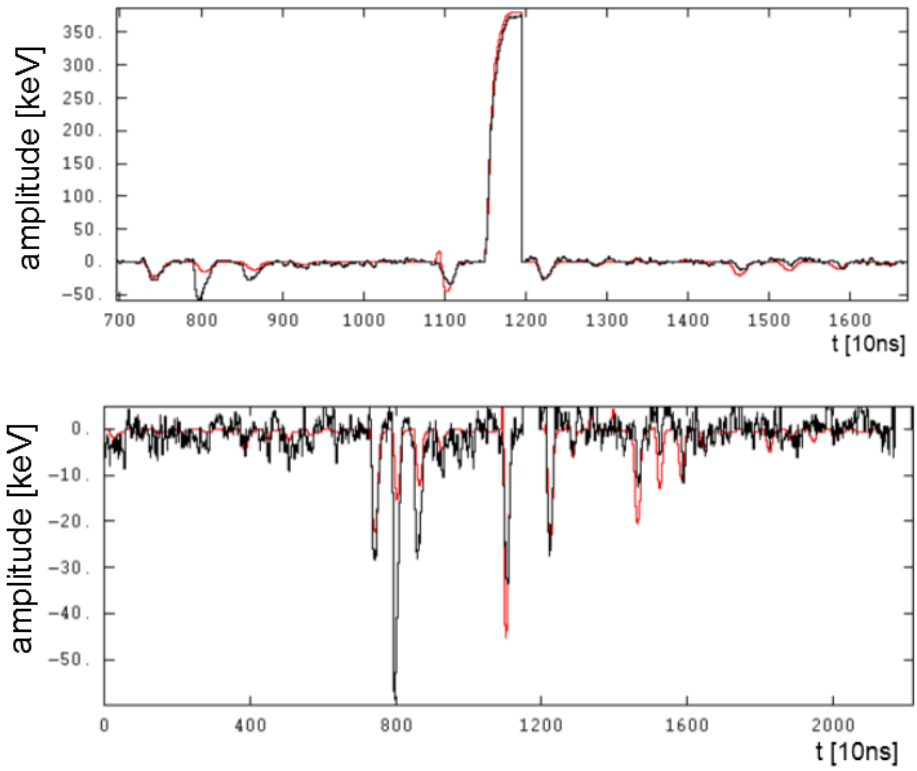

Figure 3.31: The traces for every segment are shown on the left for one event that contributed to the left plot in Fig. 3.29. A zoom on the transient signals which shows the reproduction by the calculated signal is given on the right.

$$\text{Normalized Difference} = \frac{A^m_{i,j} - A^s_{i,j}}{E^m} \tag{3.20}$$

Where E^m is the measured energy deposited in the interaction. The transient signals are also proportional to the deposited energy in the hit segment. The corresponding

distributions in Fig. 3.29 show that the distribution for the point with poor matching of signals has strong tailing and is generally more spread out. The distribution that includes the events with the better matching shows nearly Gaussian behavior and it is much narrower. The same was done for two other grid points that were selected from the distribution of hits. The first one is a single high statistic grid point where the PSA falsely allocates interaction points to this position which mainly happens for low energy interactions. The second one is a typical point in the detector that neither shows strong deviations regarding the statistics or correlations to neighboring grid points, i.e. clustering effects. The results are shown in Fig. 3.30. The distribution including the events in single high statistic grid point shows a very similar behavior as the one with the high average figure of merit value. This is consistent with the results shown in Fig. 3.19 where an increase of the average figure of merit can be seen for exactly those points. The second plot shows a behavior that lies in between the nearly Gaussian distribution and the strong tailing that was shown before, corresponding to the grid points with the low or the high figure of merit value, respectively.

For a refined analysis the corresponding traces were analyzed for the points in the detector that were selected by their average figure of merit value. The signals of the segments and the core are shown for example events in Fig. 3.31 for the poor figure of merit values and in Fig. 3.32 for the good ones. In the plots that correspond to the broad distribution of the difference of the amplitudes the transient signals cannot be reproduced very well. Only in two segments the transients of the calculated signal match the measured ones. Contrary to that the signals in Fig. 3.32 show very good agreement with the simulation.

If the amplitude of the hit segment and the core is analyzed more thoroughly, it becomes obvious that there is a mismatch of the measured and calculated energies. This mismatch can be observed if considering the amplitude for the time frame after the risetime. In this time frame, that is indicated in Fig. 3.33, the charge collection is complete and the signal will decay exponentially. It can be assumed as constant in good approximation. A zoom on a segment trace is presented in Fig. 3.33 and it shows a discrepancy of measurement and simulation.

This effect can be seen in most of the traces. To quantize the extent of this deviation the mean amplitude of measured and calculated signals, in the time frame where the signal is constant, were analyzed. Therefore, the last 10 samples of the trace were averaged and compared. Two distributions were created, using the mean amplitudes of measured and

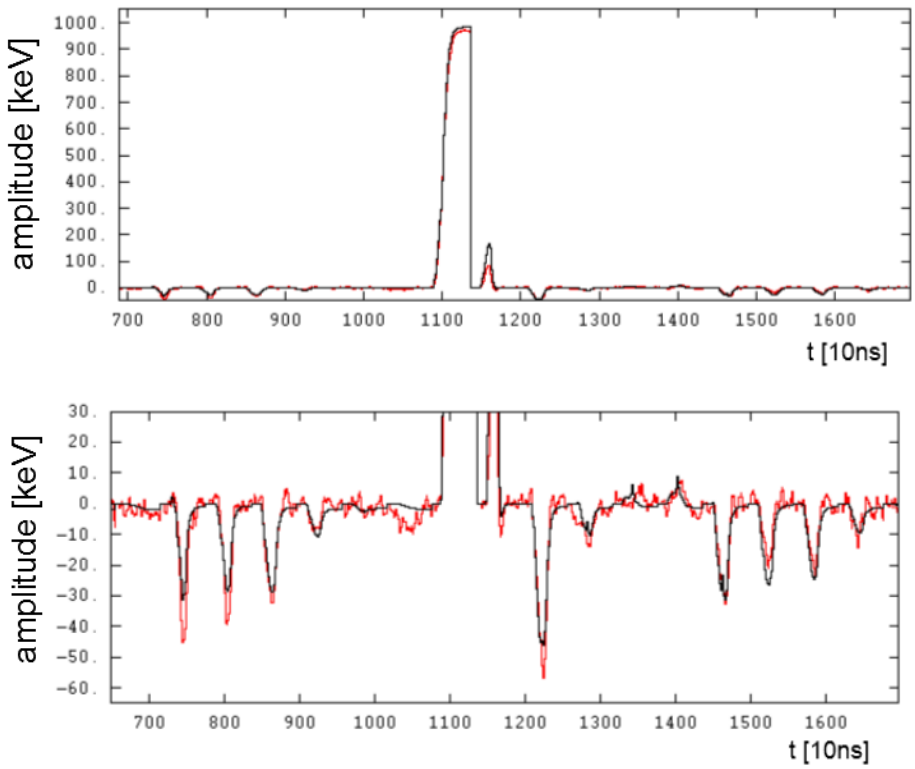

Figure 3.32: Comparison of simulated and measured signals for one event that contributes to the right distribution in Fig. 3.29. The agreement of both signals is very good, only one positive transient in one neighboring segment does not match well.

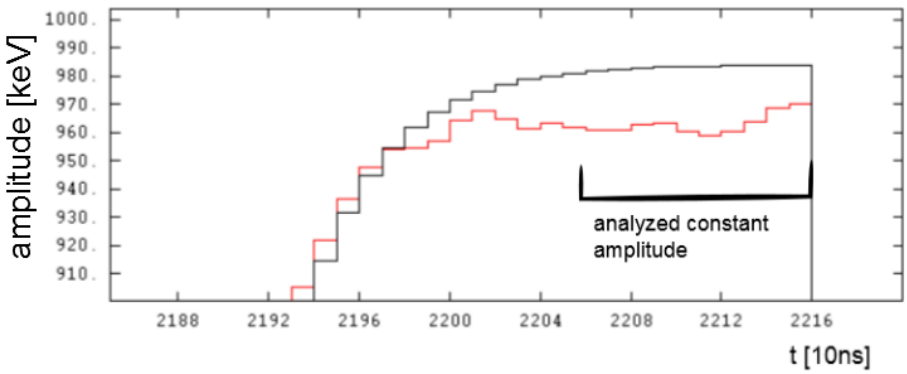

Figure 3.33: A zoom on the trace of the hit segment is shown. In the time frame where the signal becomes constant there is a systematic deviation between measured and simulated amplitudes. The measured amplitude (red) is smaller than the calculation (black). This is observed for the core signal as well. The effect can be seen for most of the events.

calculated data α_m and α_c after the risetime and the energy information E to define the deviation from the measurement $\frac{\alpha_c-\alpha_m}{\alpha_c}$ and from the energy $\frac{\alpha_c-E}{\alpha_c}$. The energy information E is the energy that is assigned to the interaction by the analysis. It is given at the end of the data block that contains the measured and calculated signals. The results are shown in Fig. 3.34. The deviation from the measurement shows clearly that the centroid is shifted towards values > 0. It is more spread out than would be expected taking only the finite energy resolution of the system into account. In contrast to that the energy information E shows only very small differences to α_c and the difference $\alpha_c - E$ is always negative. This shows that the calculated amplitude is derived from the energy information E. It cannot reach its full value in the limited time frame because only the first 560 ns after triggering are considered. The deviations from the energy are very small. To explain the discrepancy between measured and calculated amplitudes α_m and α_c the preprocessing has to be considered. The calibration for the calculated traces depends on the energy calibration for the individual segments and the core. The calibration factor for the traces C_c is derived from the energy calibration factor C_m in the following way:

$$C_c = C_m \frac{\tau_1 \tau_2}{2^{21}} \tag{3.21}$$

With τ_1 being the decay constant of the preamplifier and τ_2 the rise time of the trapezoidal shaper. The 2^{21} factor comes from the digital elctronics that work internally with 2^{37} bits whereas the traces are written only with 2^{16} bit. The time constants are set to $\tau_1 = 46\,\mu$s and $\tau_2 = 5\,\mu$s in the default setup. To minimize the deviations and optimize the calibration of the calculated signals the decay constant of the preamplifier τ_1 has to be adjusted.

The adjustment of the preamplifer decay time was done using the distribution $\frac{\alpha_c-\alpha_m}{\alpha_c}$. The decay constants are adjusted such that the new distribution centers around zero. The centroid of the distribution m with the default setup defines the new decay constant τ_1^{new}:

$$\tau_1^{\text{new}} = \tau_1(1-m) \tag{3.22}$$

This is done for every segment and the core for all detectors. The results are displayed exemplary for one detector in table 3.3. The old value of 46μs was chosen systematically too high. The new distribution of $\frac{\alpha_c-\alpha_m}{\alpha_c}$ is centered around zero per definition and the traces match better. This removes some of the systematic deviations in the difference of the time dependent amplitudes $A^c_{i,j} - A^m_{i,j}$.

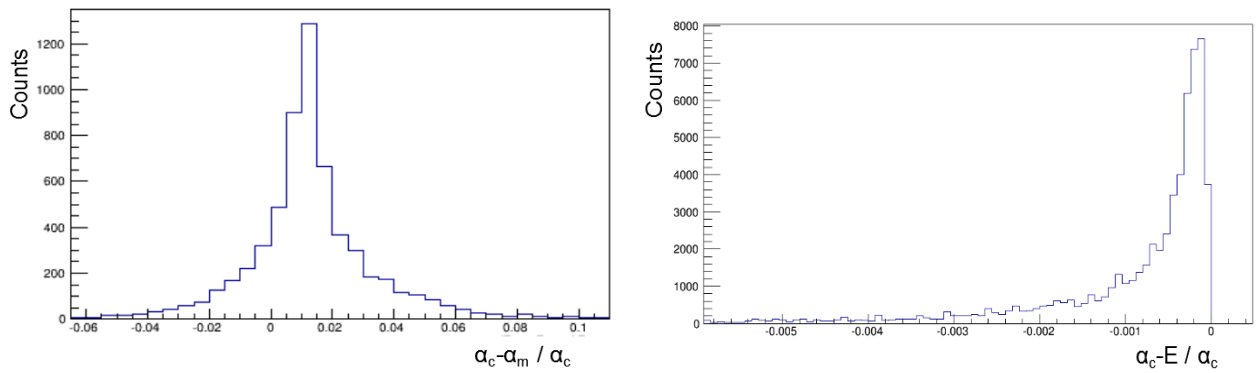

Figure 3.34: In a time frame where the signal of the hit segment becomes constant the amplitudes of measurement and calculation were averaged and compared. The plot on the left shows the normalized difference of those amplitudes and the distribution has a centroid that is significantly above zero with the mean m = 0.013. The right plot shows that the energy information E given at the end of the data block corresponds to the energy used for the calculation.

Segment	Mean m	$\tau_1^{\text{new}}[\mu\text{s}]$	Segment	Mean m	$\tau_1^{\text{new}}[\mu\text{s}]$
1	0.01237	45.43	19	0.01534	45.29
2	0.01076	45.51	20	0.01081	45.50
3	0.01227	45.44	21	0.01185	45.45
4	0.01277	45.41	22	0.01258	45.42
5	0.01656	45.24	23	0.01301	45.40
6	0.00851	45.61	24	0.01259	45.42
7	0.01052	45.52	25	0.01057	45.51
8	0.01153	45.47	26	0.01266	45.42
9	0.01203	45.45	27	0.01169	45.46
10	0.01295	45.40	28	0.01250	45.42
11	0.01360	45.37	29	0.01333	45.39
12	0.01124	45.48	30	0.01253	45.42
13	0.01206	45.45	31	0.01157	45.47
14	0.00893	45.59	32	0.01208	45.44
15	0.01290	45.41	33	0.01074	45.51
16	0.01311	45.40	34	0.01253	45.42
17	0.01396	45.36	35	0.01459	45.33
18	0.01233	45.43	36	0.01060	45.51
Core	0.01342	45.38			

Table 3.3: Adjustment of the preamplifier decay constants which were set to 46μs by default. The values were chosen in a way such that the alignment of the calculated signals with the measured ones is optimal.

3.3.3 Time Alignment

The time alignment is done in two different steps. A first alignment can be performed during the preprocessing of the data. The signal of every segment relative to the core is shifted by a constant time value. The starting time of a signal is defined by calculating the sum of the segment and the core signal. This can be expected as a straight line and the crossing with the baseline can be used as starting time. This method is energy independent and gives a timing resolution which is superior to the 10 ns time steps given by the sampling rate of 100 MHz of the digitizers.

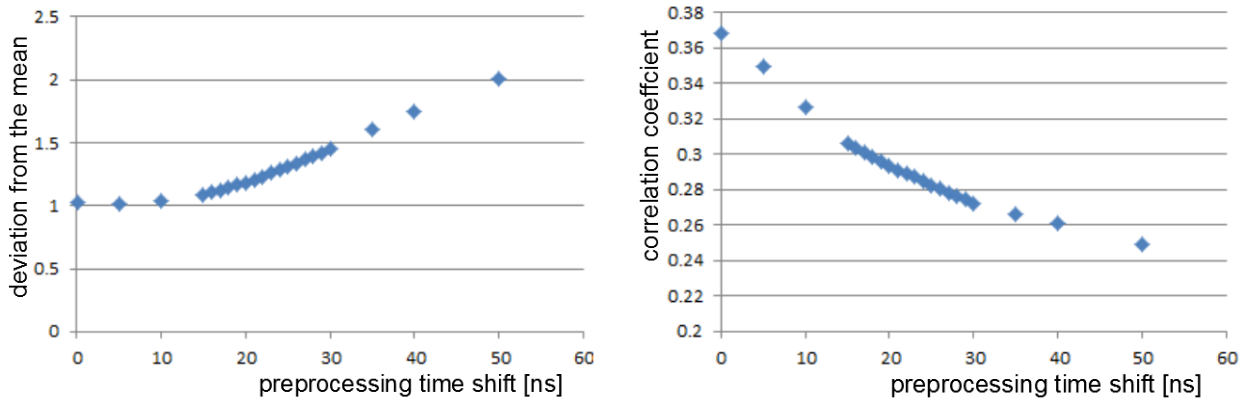

Figure 3.35: The variation of the time alignment during the preprocessing shows no visible minimum for the deviation from the mean (left) and the correlation coefficient (right). The systematic changes due to the different starting times of the PSA dominate the intrinsic change. Instead a different method was used to choose proper time shifts.

The second time alignment is performed during the PSA. The individual signals are shifted to reach the best possible alignment with the calculated signal. The figure of merit is used by a converging algorithm to find the optimal time shift. A more detailed description of the time alignment during the PSA was given in section 2.2.2. The results of the variation of the constant time shift in the preprocessing are given in Fig. 3.35 and show that the correlation coefficient and the deviation from the mean are no adequate observables to choose the correct time shift as they completely contradict each other. Instead another approach was used to choose the constant time shift of the preproceessing. This is done by observing how much the PSA time alignment algorithm has to shift the incoming signal. The corresponding constant time shift in the preprocessing is assumed to be optimal if the average time shift by the PSA is minimal, see Fig. 3.36. This way all constant time shifts can be chosen for every detector. [4]

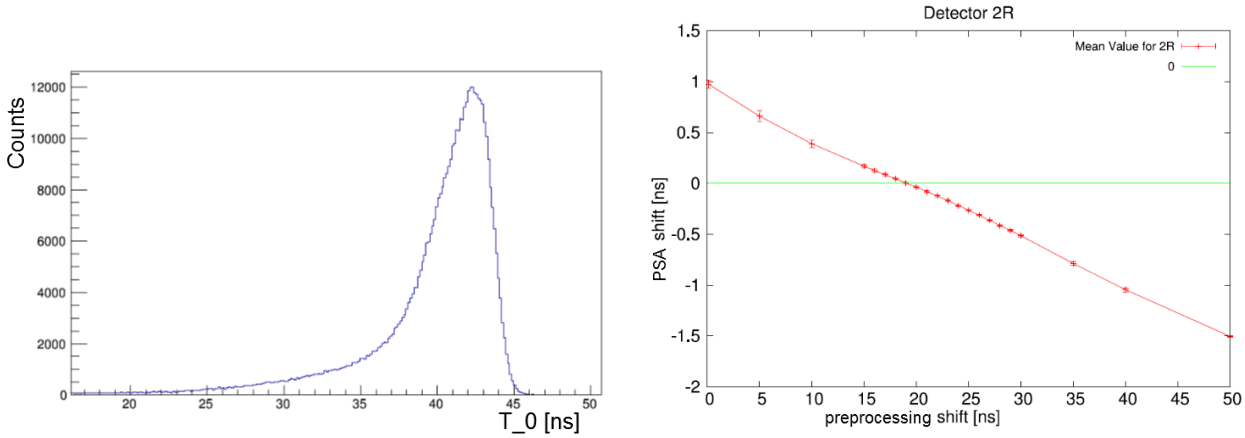

Figure 3.36: The spectrum of the starting times of one segment relative to the core is shown on the left. The width is distinctly smaller than the intrinsic 10 ns resolution. The right plot shows the selection of the time shifts in the preprocessing using the time shifts during the PSA which is the value on the y-axis taken from [4]

3.3.4 Response Function

The PSA relies on the measured pulse shapes of the signals. These signals are automatically altered by a preamplifier stage and the digitization of the data. It was discussed in section 2.1.2 that these two processes alter the measured signal which can be described by a transfer function. This transfer function is assumed to be an exponential decay that has one free parameter τ. Though the typical analytic solution to this problem is the z-transform, which was introduced in section 2.1.2, a different but faster approach was chosen in the analysis. The input signal $A[t]$ at time interval t is altered iteratively:

$$A_{\text{corrected}}[t] = \left(1 - \mathrm{e}^{-\frac{\mathrm{TS}}{\tau}}\right) A[t] + \mathrm{e}^{-\frac{\mathrm{TS}}{\tau}} A_{\text{corrected}}[t-1] \tag{3.23}$$

With the starting condition $A_{\text{corrected}} = 0$. The time parameter t is given in integers with t=0, t=1, ..., t=$\mathrm{T_f}$. The real time is defined by the timestep length TS of 10 ns. This leaves one free parameter τ to describe the whole response function of the electronics. This parameter is assigned individually for the six rings and the core of the detectors. It is possible to assign an individual τ value for each segment and the core in every detector. This would lead up to $15 \cdot 37 = 555$ parameters. Since the preamplifiers are identical large deviations are not expected within a ring. Each ring's signal is given to an individual digitizer. The algorithms for homogeneity and correlation that were developed within this

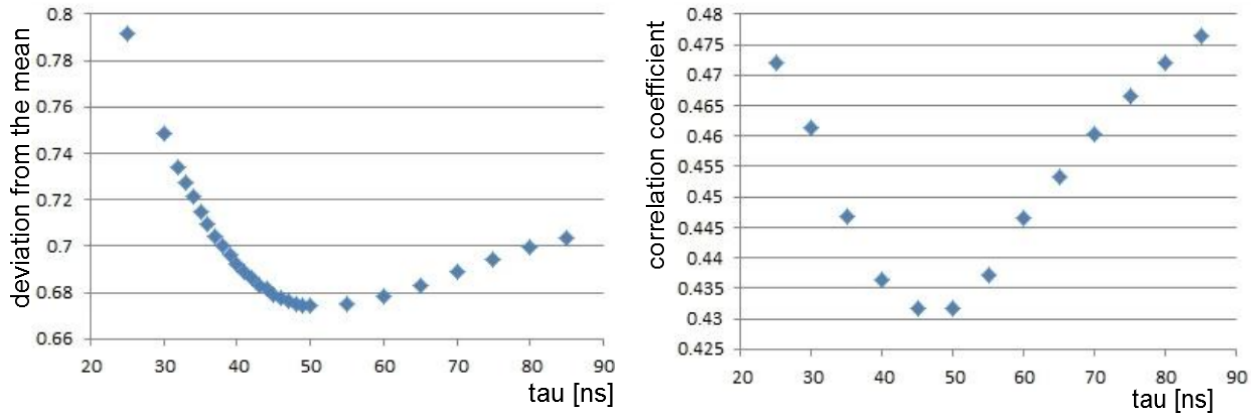

Figure 3.37: The response function was optimized using the deviation from the mean (left) and the correlation coefficient (right). The results are shown for ring two and a nice agreement of both observables can be seen which imply an optimal value around τ=48 ns.

thesis were used to find the optimal τ value for each ring. The results are displayed in Fig. 3.37 and 3.38. There is a nice agreement between the two observables. The results are also summarized in table 3.4.

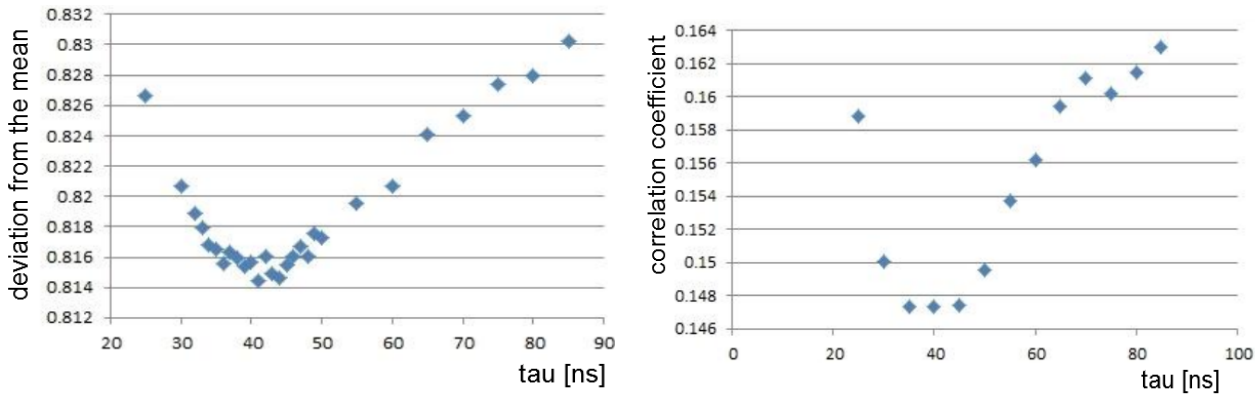

Figure 3.38: The τ optimization, using the deviation from the mean (left) and the correlation coefficient (right), for ring six is shown. The minimum can be found around 40 ns. The slope around the minimum is very small. τ=42 ns was chosen as the final value. This shows that there is a significant deviation for the transfer functions of the different rings.

The found values are used to correct for the electronic response. The previous standard value that was set to 35 ns. The parameters of both optimization methods vary in the range of 1% which implies that the impact of the response function on the PSA is only small.

Ring	τ [ns]
1	55
2	48
3	57
4	58
5	62
6	42

Table 3.4: τ value for every ring, each consisting of six segments, that was found combining the results of the inhomogeneity and correlation method.

3.3.5 Differential Crosstalk

As discussed in section 2.1.2 a correction for both proportional and differential crosstalk has to be performed. The proportional crosstalk is accessible via direct measurements and is derived during the detector setup. The proportional crosstalk is important for the energy resolution which impacts the PSA and the tracking. The differential crosstalk appears during the risetime of the signal and is therefore only relevant when analyzing the pulse shape. It was discussed in section 2.1.2 that proportional and differential crosstalk are related. The differential crosstalk coefficients are estimated using the measured values of the proportional crosstalk. The resistance R in eq. 2.10 is an unknown parameter of the differential crosstalk and it is not accessible by direct measurement. In the used implementation it is a scaling factor with which the derived differential crosstalk is multiplied. The differential crosstalk coefficients $xT_D[i,j]$ are given in the same way as the proportional coefficients $xT_P[i,j]$ in a 36 $\times$ 36 matrix and are calculated in the following way:

$$xT_D[i,j] = xT_P[i,j] - \sum_{i}^{n} xT_P[i,j] \tag{3.24}$$

For $i \neq j$ and N=36 being the number of segments. The sum is the average proportional crosstalk in case segment j is hit. The proportional crosstalk consists of the coupling of the segments to the core and the coupling between the segments. The average is an estimation for core to segment crosstalk. After the core to segment crosstalk is subtracted only the coupling of the segments i and j is left. The coefficient xT_D now has to be scaled by a scaling factor R which was varied and optimized. The results are shown in Fig. 3.39. The optimization suggests an optimal value around R=470 though the minimum is very shallow. The parameter R is given in arbitrary units. On the considered scale the

observables change in the order of roughly 2% for the variance and 5% for the correlation coefficient.

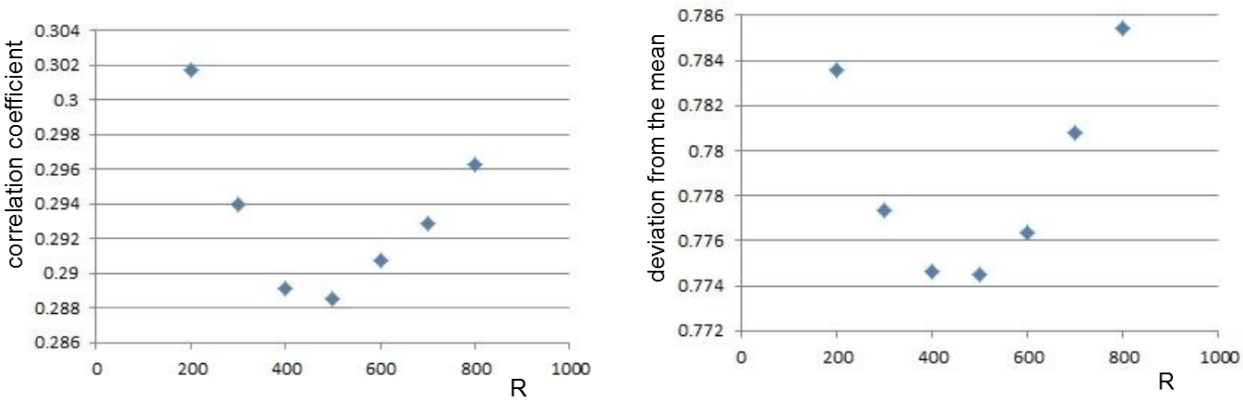

Figure 3.39: The optimization of the scaling factor for the differential crosstalk is shown. The optimization is done using the deviation from the mean (left) and the correlation method (right). Both give consistent results and suggest an optimal value around R=470.

The complete crosstalk correction is then done by altering the time dependent amplitude $A_{i,j}[t]$ of segment i when segment j was hit for $i \neq j$

$$A_{i,j,\text{corrected}}[t] = A_{\text{Core}}[t]\, xT_P[i,j] + A_{i,j}[t] + (A_{i,j}[t] - A_{i,j}[t-1])\, xT_D[i,j]\, R \tag{3.25}$$

Where $A_{i,j}[t] - A_{i,j}[t-1] = \frac{A_{i,j}[t]-A_{i,j}[t-1]}{t-(t-1)}$ corresponds to a derivative of the discrete data points. The first two terms correspond to the proportional crosstalk and the second term includes the differential crosstalk. For $i = j$ the correction is:

$$A_{i,i,\text{corrected}}[t] = A_{i,i}[t]\, xT_P[i,i] \tag{3.26}$$

Because the main diagonal matrix entries $xT_D[i,i]$ are zero.

3.4 Refinement of the Search Algorithms

The most commonly used algorithm for the PSA is the adaptive grid search. The interaction point is first searched on a coarse grid with 6 mm edge length and then on a fine grid with 2 mm edge length in a cube around the interaction point of the first coarse search.

This minimizes the CPU consumption of the PSA while maintaining high position resolution. As CPU time is not of high relevance when replaying the data offline it is possible to use the fine grid search right from the beginning. This is a lot more time consuming as the number of grid points and the corresponding traces that have to be compared increase drastically.

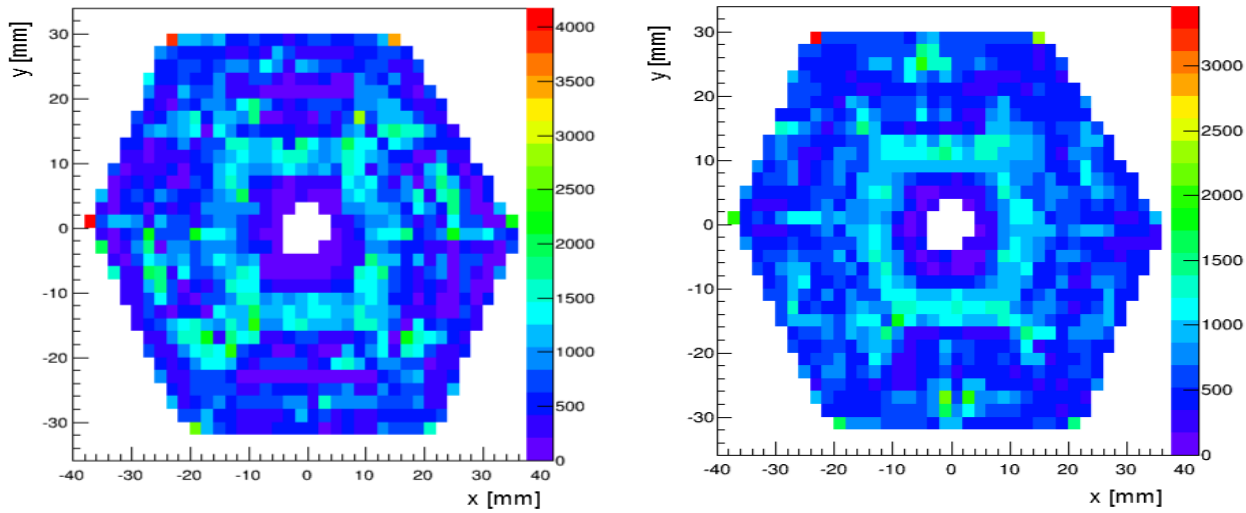

Figure 3.40: The hit distributions for the adaptive grid search using first a coarse and then a fine grid (on the left) is compared with the full search (on the right). A reduced number of wrongly allocated hits is observed. Some single high statistic grid points on the left disappear on the right.

The results are expected to be identical. The physical interaction point is supposed to be within the fine grid that is defined by the found interaction point of the coarse grid. Both search patterns were compared while keeping each parameter constant. The effect on the hit distribution is shown in Fig. 3.40. A reduction of the number of hits in one of the single high statistic grid points can be observed. The normalized deviation from the mean drops from 0.96 (adaptive search) to 0.84 (full search) while the correlation coefficient stays approximately constant. The clustering of hits is reduced as well. The full search should be used if computing power and time consumption is of low priority, like in the offline replay of the data.

The standard version the adaptive grid search assumes that only one interaction happens per segment. Considering the mean free path of a γ-ray in germanium this is to a certain degree a reasonable assumption. The mean free path is about 2 cm even for an 1 Mev γ-ray. The typical distance that a γ-ray has to travel to reach the next segment is about 1-2 cm,

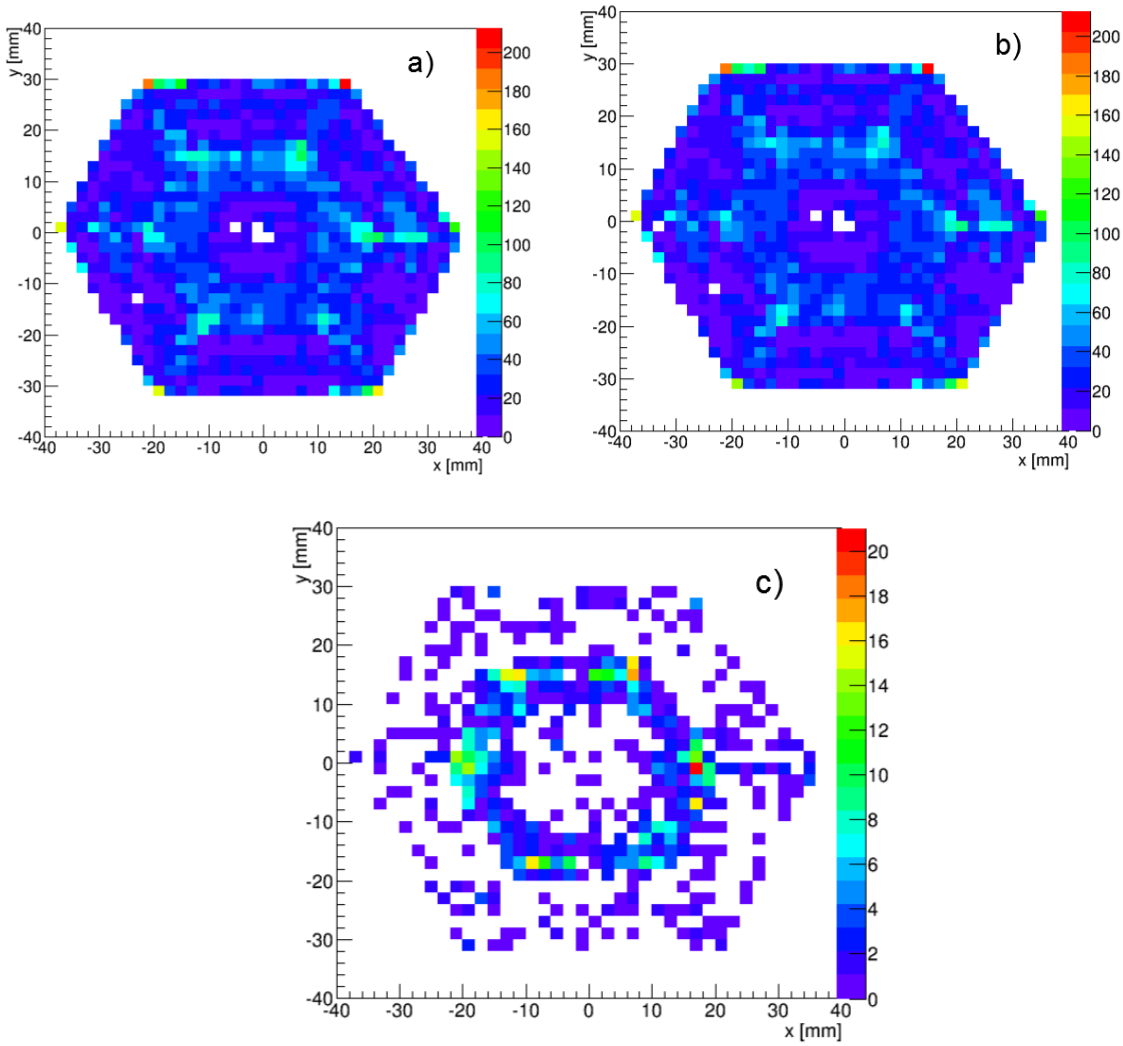

Figure 3.41: The comparison of the hit distributions for an energy of 158,5 keV and a detector depth of z = 12 mm that a) include either all events, b) events that have only one interaction per segment and c) events that only include two interactions per segment. The deviation between the first two is relatively small, only about 5% of the hits are assumed to be multiple interactions per segment. The last plot shows that those two-hit events are not distributed uniformly but are clustered around the central electrode.

depending on the position of the interaction and the direction after scattering. Additional to Compton scattering followed by another interaction of one single γ-ray the coincidence of different γ-rays has also to be considered. Multiple interactions in one segment will be allocated to the barycenter of the interactions, as described in section 2.2.2. It is possible to include these two-hit events by assuming that the signals belonging to these events will

cause a bad matching with the simulation. If the corresponding figure of merit is above a certain threshold value the search is repeated assuming two interactions. The two-hit search result is used instead in case of better figure of merit values .

The data was replayed searching for multiple interactions per segment. To perform the comparison the allocated hit pattern was investigated on an event by event basis determining if multiple hits were assigned to one segment. The results of Fig. 3.41 show that there is only a small difference between the hit distribution that contains multiple hits a) and the one that only includes one-hit events b). About 5% of the interactions were assumed to be two-hit events. The difference between the two plots, i.e. all two-hit events, are shown in the third plot and it can be seen that the allocated interaction positions are not distributed uniformly. In first order a uniform distribution of events with multiple interactions in one segment is expected. The hits are clustered around the central electrode. This implies that the discrimination between one-hit and two-hit events has to be improved. The allocated interaction positions are in most cases not correct. The distinction between one-hit and two-hit events is done solely by comparing the two corresponding figure of merit values. If a single interaction in a segment took place and the PSA cannot find a good fit, the algorithm is asked to treat this as a two-hit event. The obtained results show that in the current implementation it is better to neglect multiple interactions per segment. A source run with ^{152}Eu was investigated. However an in beam experiment with high counting rates, high crystal multiplicities and correlated γ-rays does increase the need to include multiple interactions per segment into the PSA.

3.5 Implementation of the Optimized Configuration

After the optimization of the producer parameter the results are compared with the previous configurations. The optimization was performed for the distance metric, the preamplifier decay time, the response function, the preprocessing time alignment and the differential crosstalk. It is the aim of this thesis to investigate systematic errors of the PSA. For this purpose xy hit distributions were used for comparison. In Fig. 3.42 it is shown that an improvement was achieved, especially the clustering of hits and the visibility of the segment structure is reduced. The number of entries in single grid points with too high statistics is reduced, see Fig. 3.43. In summary the optimization yielded an improved PSA performance. Not all systematic effect could be eliminated. The clustering is still present though

the segment structure is not as clearly visible as before.

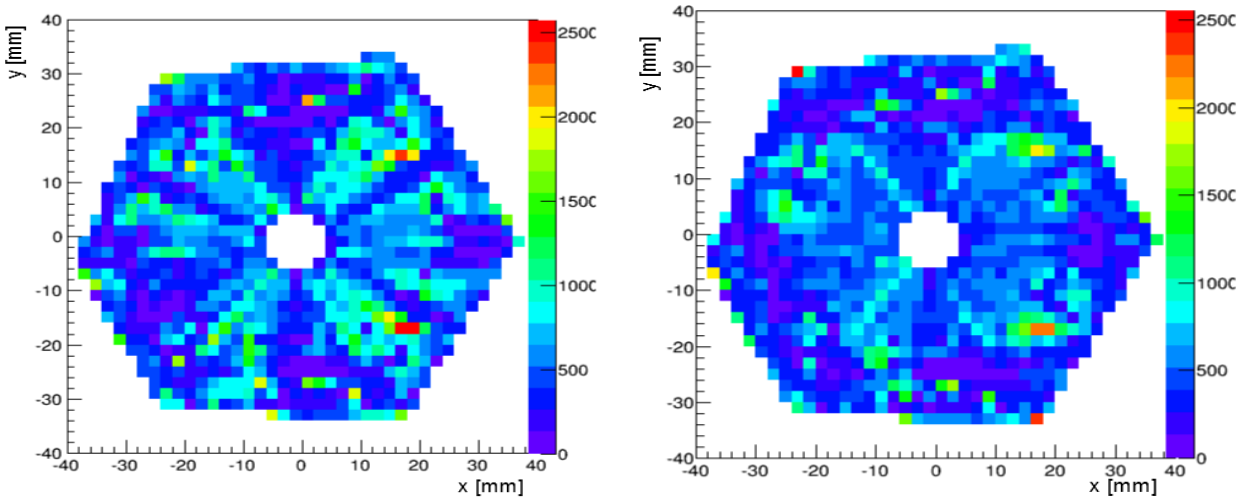

Figure 3.42: Comparison of hit distributions for the previous and the found optimal configurations. The clustering of hits and the visibility of the segment structure is reduced. The single high statistic grid point moves from the segment middle to the edge of the detector but the number of entries in it remains constant.

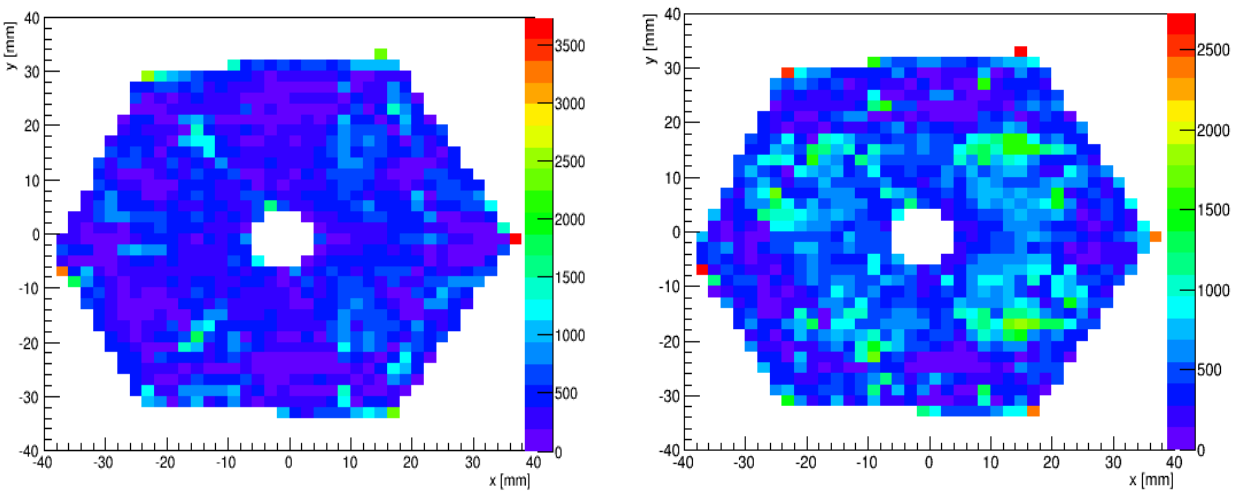

Figure 3.43: The comparison of the different configurations is shown, this time for a detector depth of z = 24 mm. A reduction of the number of hits in the single high statistic grid point on the right edge of the detector can be observed.

4 Summary and Outlook

The PSA, consisting of a signal basis and a search algorithm, has several ingredients that determine the analysis of the incoming data and affect the final allocated interaction position. The PSA shows in its current state systematic deviations from the expected results. Certain types of events, especially low energy interactions, are not always assigned to the correct interaction point. A homogeneous distribution with statistical fluctuation is expected when considering the hit distributions of source runs. The observed behavior is strongly inhomogeneous and therefore the PSA was investigated thoroughly. The energy and position dependence, defined by an angle, a radius and a detector depth, was examined. The quality of the Doppler correction as criteria could only be used to a certain extent to judge the PSA performance. The qualitiy of the Doppler correction depends indirectly and partially on the PSA position resolution.

Therefore, two new methods were developed to describe the PSA performance. These methods are based on the fact that in a source run homogeneous distributions of interaction points are measured. The defined observables quantify how well the PSA result matches these expectations. Every set of grid points that have the same distance to the source and belong to the same detector is analyzed separately. The first method compares the number of hits per grid point with the expected amount and defines a deviation from the mean, very similar to a standard deviation. The second method describes the correlation of neighboring grid points. A C/C++ code was written that implements these analysis steps using the root data of either the NARVAL emulator femul or the Watchers. The written code allows an in depth analysis of the PSA performance using not only the distribution of hits but also information generated by comparison of measured and calculated data. The performed analysis showed that the PSA has problems at the segment borders.

The PSA ingredients were varied and optimized. Special attention was given to five quantities (i) the time alignment, (ii) the detector response, (iii) the distance metric, (iv) the alignment of the traces and (v) the treatment of the differential crosstalk. The new developed methods allowed to optimize these PSA parameters with better and improved

precision than previously done. Most of the considered parameters are not easily accessible to a direct measurement. The conducted optimization of the PSA ingredients yielded an improvement of the PSA performance.

The systematic errors could be reduced though still some unexpected, unphysical behavior in the hit distributions can be observed. There are still some remaining parameters (though they have decreasing impact on the PSA result) which have to be scrutinized more. These are, for example, parameters in the converging PSA time alignment algorithm (e.g. minimal and maximum accepted time shifts or minimum/maximum number of loops) or parameters for the two hit variant of the adaptive grid search. The two-hit search requires limits for minimal allowed energies or distances between the interaction points. A future advanced approach has to reconsider the signal basis and the corresponding parameters, like space charge distribution and charge carrier mobilities of the individual crystals. Though these were already chosen very carefully.

In certain cases the PSA simply reaches its limits defined by noise and instability of the baseline. This is especially true for low energy interactions. However in general the PSA performance is remarkably good and most of the hits are assigned correctly. The tracking is based on the position information given by the PSA and it provides background suppressed spectra with very good Doppler corrections [4, 28].

Bibliography

[1] *femul*. Università di Padova, Italy, 2013 . – private communication 31

[2] Bazzacco, Dino: Advanced Gamma Tracking Array: Review of AGATA and Data Processing. In: *EGAN School Liverpool* (2011) 12

[3] Birkenbach, B. ; Bruyneel, B. ; Pascovici, G. ; Eberth, J. ; Hess, H. ; Lersch, D. ; Reiter, P. ; Wiens, A.: Determination of space charge distributions in highly segmented large volume HPGe detectors from capacitance–voltage measurements. In: *Nuclear Instruments and Methods in Physics Research Section A: Accelerators, Spectrometers, Detectors and Associated Equipment* 640 (2011), Nr. 1, 176 - 184. http://dx.doi.org/http://dx.doi.org/10.1016/j.nima.2011.02.109. – DOI http://dx.doi.org/10.1016/j.nima.2011.02.109. – ISSN 0168–9002 21

[4] Birkenbach, Benedikt: *Gamma ray tracking with the AGATA demonstrator - A novel approach for in-beam spectroscopy*, Institute for Nuclear Physics Cologne, Diss., 2014 22, 34, 36, 61, 70, 71, 80

[5] Blinder, S. M.: 'Klein-Nishina Formula for Photon-Electron Scattering' from the Wolfram Demonstrations Project. (2012). http://demonstrations.wolfram.com/KleinNishinaFormulaForPhotonElectronScattering/, 30

[6] Brun, R. ; Rademakers, F.: *ROOT - A Data Analysis Framework*. http://root.cern.ch. Version: 2010 32

[7] Bruyneel, B. ; Birkenbach, B. ; Reiter, P.: Space charge reconstruction in highly segmented {HPGe} detectors through capacitance-voltage measurements. In: *Nuclear Instruments and Methods in Physics Research Section A: Accelerators, Spectrometers, Detectors and Associated Equipment* 641 (2011), Nr. 1, 92 - 100. http://dx.doi.org/http://dx.doi.org/10.1016/j.nima.2011.02.110. – DOI http://dx.doi.org/10.1016/j.nima.2011.02.110. – ISSN 0168–9002 21

[8] Bruyneel, Bart: On the origin of differential crosstalk in segmented detectors. In: *AGATA Week Uppsala* (2008). http://www.agata.org/links/aw 18

[9] Bruyneel, Bart: Pulse Shape Analysis with the AGATA Demonstrator. In: *Germanium Workshop Berkley* (2010) 18

[10] Bruyneel, Bart: Electronics. In: *EGAN School Liverpool* (2011) 13, 17, 18

[11] Bruyneel, Bart: Weighting Potentials. In: *EGAN School Liverpool* (2011) 14, 24

[12] Bruyneel, Bart ; Reiter, Peter ; Pascovici, Gheorghe: Characterization of large volume {HPGe} detectors. Part I: Electron and hole mobility parameterization. In: *Nuclear Instruments and Methods in Physics Research Section A: Accelerators, Spectrometers, Detectors and Associated Equipment* 569 (2006), Nr. 3, 764 - 773. http://dx.doi.org/http://dx.doi.org/10.1016/j.nima.2006.08.130. – DOI http://dx.doi.org/10.1016/j.nima.2006.08.130. – ISSN 0168–9002 20

[13] Bruyneel, Bart ; Reiter, Peter ; Pascovici, Gheorghe: Characterization of large volume {HPGe} detectors. Part II: Experimental results. In: *Nuclear Instruments and Methods in Physics Research Section A: Accelerators, Spectrometers, Detectors and Associated Equipment* 569 (2006), Nr. 3, 774 - 789. http://dx.doi.org/http://dx.doi.org/10.1016/j.nima.2006.08.129. – DOI http://dx.doi.org/10.1016/j.nima.2006.08.129. – ISSN 0168–9002 20

[14] Bruyneel, Bart ; Reiter, Peter ; Wiens, Andreas ; Eberth, Jürgen ; Hess, Herbert ; Pascovici, Gheorghe ; Warr, Nigel ; Aydin, Sezgin ; Bazzacco, Dino ; Recchia, Francesco: Crosstalk corrections for improved energy resolution with highly segmented HPGe-detectors. In: *Nuclear Instruments and Methods in Physics Research Section A: Accelerators, Spectrometers, Detectors and Associated Equipment* 608 (2009), Nr. 1, 99 - 106. http://dx.doi.org/http://dx.doi.org/10.1016/j.nima.2009.06.037. – DOI http://dx.doi.org/10.1016/j.nima.2009.06.037. – ISSN 0168–9002 17

[15] Bruyneel, Bart ; Reiter, Peter ; Wiens, Andreas ; Eberth, Jürgen ; Hess, Herbert ; Pascovici, Gheorghe ; Warr, Nigel ; Weisshaar, Dirk: Crosstalk properties of 36-fold segmented symmetric hexagonal HPGe detectors. In: *Nuclear Instruments and Methods in Physics Research Section A: Accelerators, Spectrometers, Detectors and Associated Equipment* 599 (2009), Nr. 2–3, 196 - 208.

http://dx.doi.org/http://dx.doi.org/10.1016/j.nima.2008.11.011. – DOI http://dx.doi.org/10.1016/j.nima.2008.11.011. – ISSN 0168–9002 15, 16

[16] Deleplanque, M.A. ; Lee, I.Y. ; Vetter, K. ; Schmid, G.J. ; Stephens, F.S. ; Clark, R.M. ; Diamond, R.M. ; Fallon, P. ; Macchiavelli, A.O.: GRETA: utilizing new concepts in γ-ray detection. In: *Nuclear Instruments and Methods in Physics Research Section A: Accelerators, Spectrometers, Detectors and Associated Equipment* 430 (1999), Nr. 2–3, 292 - 310. http://dx.doi.org/http://dx.doi.org/10.1016/S0168-9002(99)00187-4. – DOI http://dx.doi.org/10.1016/S0168–9002(99)00187–4. – ISSN 0168–9002 10

[17] Duchene, G. ; Farnea, E. ; Gadea, A. ; Korichi, A. ; Nyberg, J. ; Reiter, P. ; Simpson, J.: AGATA—Advanced {GAmma} Tracking Array. In: *Nuclear Instruments and Methods in Physics Research Section A: Accelerators, Spectrometers, Detectors and Associated Equipment* 668 (2012), Nr. 0, 26 - 58. http://dx.doi.org/http://dx.doi.org/10.1016/j.nima.2011.11.081. – DOI http://dx.doi.org/10.1016/j.nima.2011.11.081. – ISSN 0168–9002 10, 11, 12, 18, 31

[18] Grave, X. ; Canedo, R. ; Clavelin, J.-F. ; Du, S. ; Legay, E.: NARVAL a modular distributed data acquisition system with Ada 95 and RTAI. In: *Real Time Conference, 2005. 14th IEEE-NPSS*, 2005, S. 5 pp.– 31

[19] He, Zhong: Review of the Shockley–Ramo theorem and its application in semiconductor gamma-ray detectors. In: *Nuclear Instruments and Methods in Physics Research Section A: Accelerators, Spectrometers, Detectors and Associated Equipment* 463 (2001), Nr. 1–2, 250 - 267. http://dx.doi.org/http://dx.doi.org/10.1016/S0168-9002(01)00223-6. – DOI http://dx.doi.org/10.1016/S0168–9002(01)00223–6. – ISSN 0168–9002 16

[20] Knoll, Glenn F.: *Radiation Detection and Measurement*. Forth Edition. New York, USA : Wiley, 2010

[21] Lopez-Martens, A. ; Hauschild, K. ; Korichi, A. ; Roccaz, J. ; Thibaud, J-P.: γ-ray tracking algorithms: a comparison. In: *Nuclear Instruments and Methods in Physics Research Section A: Accelerators, Spectrometers, Detectors and Associated Equipment* 533 (2004), Nr. 3, 454 - 466. http://dx.doi.org/http://dx.doi.org/10.1016/j.nima.2004.06.154. – DOI http://dx.doi.org/10.1016/j.nima.2004.06.154. – ISSN 0168–9002 29

[22] Recchia, F. ; Bazzacco, D. ; Farnea, E. ; Gadea, A. ; Venturelli, R. ; Beck, T. ; Bednarczyk, P. ; Buerger, A. ; Dewald, A. ; Dimmock, M. ; Duchêne, G. ; Eberth, J. ; Faul, T. ; Gerl, J. ; Gernhaeuser, R. ; Hauschild, K. ; Holler, A. ; Jones, P. ; Korten, W. ; Kröll, Th. ; Krücken, R. ; Kurz, N. ; Ljungvall, J. ; Lunardi, S. ; Maierbeck, P. ; Mengoni, D. ; Nyberg, J. ; Nelson, L. ; Pascovici, G. ; Reiter, P. ; Schaffner, H. ; Schlarb, M. ; Steinhardt, T. ; Thelen, O. ; Ur, C.A. ; Dobon, J.J. V. ; Weisshaar, D.: Position resolution of the prototype {AGATA} triple-cluster detector from an in-beam experiment. In: *Nuclear Instruments and Methods in Physics Research Section A: Accelerators, Spectrometers, Detectors and Associated Equipment* 604 (2009), Nr. 3, 555 - 562. `http://dx.doi.org/http://dx.doi.org/10.1016/j.nima.2009.02.042`. – DOI http://dx.doi.org/10.1016/j.nima.2009.02.042. – ISSN 0168–9002 19

[23] Recchia, F. ; Bazzacco, D. ; Farnea, E. ; Gadea, A. ; Venturelli, R. ; Beck, T. ; Bednarczyk, P. ; Buerger, A. ; Dewald, A. ; Dimmock, M. ; Duchêne, G. ; Eberth, J. ; Faul, T. ; Gerl, J. ; Gernhaeuser, R. ; Hauschild, K. ; Holler, A. ; Jones, P. ; Korten, W. ; Kröll, Th. ; Krücken, R. ; Kurz, N. ; Ljungvall, J. ; Lunardi, S. ; Maierbeck, P. ; Mengoni, D. ; Nyberg, J. ; Nelson, L. ; Pascovici, G. ; Reiter, P. ; Schaffner, H. ; Schlarb, M. ; Steinhardt, T. ; Thelen, O. ; Ur, C.A. ; Dobon, J.J. V. ; Weisshaar, D.: Position resolution of the prototype {AGATA} triple-cluster detector from an in-beam experiment. In: *Nuclear Instruments and Methods in Physics Research Section A: Accelerators, Spectrometers, Detectors and Associated Equipment* 604 (2009), Nr. 3, 555 - 562. `http://dx.doi.org/http://dx.doi.org/10.1016/j.nima.2009.02.042`. – DOI http://dx.doi.org/10.1016/j.nima.2009.02.042. – ISSN 0168–9002 19, 59, 60

[24] Recchia, Francesco: *In-beam test and imaging capabilites of the AGATA prototype detector*, Diss., 2008 11

[25] Recchia, Francesco: *In beam test and imaging capabilities of AGATA prototype detector*, Universita degli studi di Padova, Diss., 2008 27

[26] Venturelli, Roberto: Adaptive Grid Search. In: *AGATA Week Liverpool* (2006) 12, 26

[27] Vogt, Andreas: *Teilchenidentifikation für In-Beam-Gammaspektroskopie neutronenreicher Aktinidenkerne*, Universität zu Köln, Bachelor thesis, 2012 61

[28] Vogt, Andreas: *In-Beam γ-ray Spectroscopy of Neutron-Rich Actinides with Multinucleon-Transfer Reactions*, Universität zu Köln, Master thesis, 2014. – to be published. 34, 61, 80

List of Figures

List of Tables

Acknowledgements

I would like to thank Prof. Dr. Peter Reiter for the opportunity to work in his working group and the provision of the subject as well as his support.

I would also like to thank the whole working group for their help, support and the good working atmosphere. Special thanks goes to Benedikt Birkenbach for his time-consuming contributions and his insight on programming.

I also would like to thank Bart Bruyneel for his good suggestions and helpful discussions.

At last I would like to acknowledge Dino Bazzacco for his efforts and his support regarding the replay of the data.

Eidesstattliche Erklärung

Hiermit bestätige ich, dass ich meine Masterarbeit selbstständig angefertigt und keine anderen als die angegebenen Quellen und Hilfsmittel benutzt sowie Zitate kenntlich gemacht habe.

Köln, den 11. Juli 2014

_____